Jorun Zahl Albertsen

Experimental and theoretical investigations of metal dusting corrosion in plant exposed nickel-based alloys

Thesis for the degree philosophiae doctor

Trondheim, March 2007

Norwegian University of Science and Technology
Faculty of Natural Sciences and Technology
Department of Materials Science and Engineering

NTNU
Innovation and Creativity

NTNU
Norwegian University of Science and Technology

Thesis for the degree philosophiae doctor

Faculty of Natural Sciences and Technology
Department of Materials Science and Engineering

© Jorun Zahl Albertsen

ISBN 978-82-471-1092-8 (printed version)
ISBN 978-82-471-1108-6 (electronic version)
ISSN 1503-8181

Doctoral theses at NTNU, 2007:50
IMT-Report 2007:91

Printed by NTNU-trykk

Preface

This doctoral thesis presents results from the PhD-study carried out at the Department of Materials Science and Engineering at the Norwegian University of Science and Technology, NTNU, between January 2004 and December 2006.

The financial support has been provided by Statoil ASA and The Norwegian Research Council through the ThermoTech KMB project; Thermodynamics Applied to High Temperature Materials Technology.

Before the project started, the author attended the MTI/NiDI Meeting, in Maastricht, Netherlands, November 2003, with the presentation; "*Microscale Investigations of High-temperature Corrosion Reactions in Different Nickel-based Alloys*".

During the course of the work, the author has attended two international conferences where parts of the thesis have been presented:

"Metallurgical Investigations of Metal Dusting Corrosion in Plant Exposed Nickel-Based Alloy 602CA", presented at the EUROCORR 2004 Conference in Nice, France, 12.-16. September 2004.

"Analysis Tools in Metal Dusting Research", presented at Corrosion/2005, Technology Exchange Group meeting, TEG128X, Houston, Texas, USA, 3.-7. April 2005.

The main results of this investigation have been published or are in the process of being published in international journals and conference proceedings;

Albertsen, J. Z., Grong, Ø., Mathiesen, R. H., Schmid, B.: "*Metallurgical Investigation of Metal Dusting Corrosion in Plant Exposed Nickel-Based Alloy 602CA*", Corrosion Engineering, Science and Technology, vol. 40, No. 3, pp.239-243 (2005).

De Bruyn, H. J., Schmid, B., Grong, Ø., Albertsen, J. Z.: "*Adapting Metal Dusting Research to Trends in Syngas Technology*", paper presented at Corrosion/2005, Houston, Texas, USA, 3.-7. April 2005, paper No. 5413, NACE International, Houston, Texas, USA.

Albertsen, J. Z., Grong, Ø., Walmsley, J.C., Mathiesen, R.H., Van Beek, W., Schmid, B.: "*Surface Disintegration of Nickel-Based Alloys During Long Time Exposure to Syngas in an Industrial Plant for Methanol Production*", submitted for publication in Metallurgical and Materials Transactions A (2006).

Albertsen, J. Z., Grong, Ø, Walmsley, J.C, Mathiesen: "*A Model for Metal Dusting Corrosion in Nickel-Based Alloys Involving Internal Precipitation of Carbides, Oxides and Graphite*", submitted for publication in Metallurgical and Materials Transactions A (2006).

Trondheim, December 2006

Jorun Zahl Albertsen

Jorun Zahl Albertsen

Acknowledgements

First of all, I would like to acknowledge the important contribution from Professor Øystein Grong, who has been my principal thesis supervisor. I am extremely grateful for his excellent supervision and his active role in this project. His interest, great support and encouragement during these years are highly appreciated.

I am also grateful to Mr. Hennie De Bruyn (Borealis) and Dr. Bernd Schmid at Statoil Research Centre, Trondheim. Their genuine interest in metal dusting corrosion has inspired me during these years. To both of you, I am extremely grateful for your valuable advices and great support.

Moreover, I am grateful to my co-supervisor Professor John Walmsley at SINTEF Materials and Chemistry for assisting with the TEM experiments and to Dr. Ragnvald Mathiesen at SINTEF Materials and Chemistry for planning and carrying out the synchrotron X-ray diffraction analyses at SNBL in Grenoble in collaboration with Dr. W. Van Beek. To all of you, I am extremely thankful for your contribution, support and valuable advice during these three years.

During the course of the work I have benefited from interaction and collaboration with numerous people within the science community. In particular, I would like to thank Dr. Peter Heard at Bristol University in England, Professor Jarle Hjelen (NTNU) and NAKA Customer Centre in Japan for preparing the FIB samples. Special thanks to my colleagues at the SEM laboratory at NTNU for valuable help during these years. Furthermore, Dr. Kai Tang at SINTEF Materials and Chemistry is acknowledged for assisting with the thermodynamic analyses and Mr. Erlend F. Nordstrand (NTNU) for assisting with the specimen preparation and microscope analyses.

In addition, I am very thankful to my friends and my family for always being around. My deep gratitude in particular goes to my parents, Turid and Helge, not only during the years of this study, but for always listening to me, supporting and encouraging me during stressful times. And finally, I would like to thank Eskil for making these last years particularly cheerful.

Abstract

This doctoral thesis is concerned with experimental and theoretical studies of high temperature corrosion phenomena in plant exposed nickel-based alloys. Different complementary experimental techniques have been used to unravel the microstructural changes and phase formations accompanying the corrosion process, including light microscopy, hardness measurements, field emission scanning electron microscopy (FEG SEM), microprobe / WDS analyses, transmission electron microscopy (TEM) and synchrotron X-ray diffraction (S-XRD). These results together with thermodynamic and kinetic modelling of the rate phenomena involved have provided new insight into the mechanisms of metal dusting corrosion in Ni-based alloys under real plant exposure conditions that have not previously been disclosed using accelerated laboratory tests.

The thesis is divided into five parts.

Part I gives a general introduction to metal dusting corrosion. In particular, aspects of metal dusting corrosion in low alloyed steels, complex engineering alloys and nickel-based alloys have been reviewed and put into proper perspective.

In **Part II** of the thesis a research strategy aiming at a more fundamental understanding of the mechanisms of metal dusting corrosion is presented. Then a full description of the materials, exposure conditions and the experimental techniques being applied throughout the investigations is given as a lead-in to the subsequent microstructure and phase characterisation.

In **Part III** of the thesis, metallurgical characterisation of the nickel-based alloy 602 has been carried out following plant exposure at approximately 540˚C for 2 years. In general, alloy 602 is found to exhibit a high intrinsic resistance to metal dusting corrosion under the prevailing circumstances. Only a thin zone is affected by carbon intrusion, extending about 20μm from the surface and into the bulk of the material. The subsequent FEG SEM and S-XRD analyses of the exposed 602 alloy revealed the presence of various phases at the corroded surface, including nepheline ($NaAlSiO_4$) and presumably also corundum ($Al_{2-x}Cr_xO_3$). None of these oxide phases are commonly observed in connection with metal dusting corrosion.

In **Part IV** of the thesis, the surface disintegration and microstructural stability of the two nickel-based alloys 602 and 693, containing varying levels of chromium and aluminium, have been examined both during oxidising conditions in the laboratory and following 2 and 4 years of exposure to syngas in an industrial plant for methanol production at 540˚C and 35 bar total pressure. The near surface phases were investigated using optical microscopy and hardness measurements, and further characterised by employing synchrotron X-ray diffraction (XRD) in combination with scanning and transmission electron microscopy (SEM/TEM). The disintegration process starts by rejection of α-Cr from the supersaturated austenite matrix. The process proceeds by reactions between the surface oxide layer and the syngas containing the trace elements Si, Na, Ni at the ppb level. The former elements contribute to the development of nepheline ($NaAlSiO_4$) at the outmost surface facing the gas, whereas the deposited Ni particles from the syngas promote coke formation by catalysing the Boudouard reaction ($2CO = C + CO_2$). On the inside a mixed Cr_2O_3-Al_2O_3 oxide layer is observed, both in the steam oxidised and plant exposed alloys. In particular, the inner aluminium oxide is very dense and provides an effective getter against carbon intrusion into the bulk of the alloys by virtue of its ability to restore cracks and flaws through diffusion. Eventually, restrictions in the supply of reactants (e.g. Al) to the oxide/ metal interface complete the incubation period and lead to the formation of corrosion pits at the bottom of the open surface cracks being in direct contact with the syngas atmosphere.

Finally, **Part V** is concerned with fundamental studies of the mechanisms of metal dusting corrosion in the Ni-based alloys 602 and 693 during long time exposure to syngas at 540^{o}C and 35 bar total pressure. Four years plant exposed alloys were examined using synchrotron X-ray diffraction in combination with scanning- and transmission electron microscopy. It is concluded that the metal dusting corrosion attacks start by carbon diffusing into the bulk of the alloys following the break-down of the protective Cr_2O_3 - Al_2O_3 surface oxide layer. During the incubation period this oxide layer provides an effective barrier against carbon intrusion by virtue of its ability to restore cracks and flaws through diffusion. The corrosion pits then grow by a process of internal carburisation and oxidation, where carbides, oxides and graphite form separately within an approximately 30μm thick belt in front of the pits (referred as the white zone). In particular, the oxidation of the internal Cr_3C_2 carbides occurring close to the white zone/pit interface is associated with large volume changes. This volume expansion results in build-up of high mechanical stresses within the white zone and eventually to the complete disintegration of the original alloy matrices into a layered pit

microstructure consisting of Ni + Fe and Cr_2O_3 + Al_2O_3 + graphite, respectively. The observed microstructural changes have been rationalised through detailed modelling of the physical reactions involved, leading to the development of new and comprehensive models for metal dusting corrosion in Ni-based alloys.

Table of contents

Preface iii

Acknowledgements v

Abstract vi

Table of contents ix

PART I

General introduction to metal dusting corrosion 1

1.1 Introduction 3

1.2 Introduction to syngas technology 3

1.2.1 Steps in conversion of natural gas to syngas 4

1.2.2 Plant operating conditions 5

1.2.3 The use of nickel-based alloys 6

1.2.3.1 Phase relations and microstructural stability 6

1.2.3.2 Structure property relationships 9

1.2.4 Reported failure cases in plants for syngas production 10

1.3 Thermodynamics and kinetics relevant to metal dusting corrosion 12

1.3.1 Carbon activity in the gas phase 13

1.3.2 Conditions for carbide formation 15

1.3.3 Conditions for surface oxide formation 19

1.3.4 Diffusion of reactants in the solid state 21

1.3.4.1 Solutions of Fick’s law of diffusion 21

1.3.4.2 Extent of carbon intrusion 23

1.3.4.3 Extent of Al and Cr diffusion 24

1.4 Models for metal dusting corrosion 25

1.4.1 Metal dusting corrosion in low alloyed steels 25

1.4.2 Metal dusting corrosion in complex engineering alloys 28

1.4.3 Metal dusting corrosion in nickel-based alloys 29

1.4.4 Summary of current knowledge 30

1.5 References 32

PART II

Scope and experimental approach 37

2.1 Research strategy 39
2.1.1 Exposure conditions 40
2.1.2 Mechanisms 40
2.1.3 Examination tools 40
2.1.4 Concluding remarks 41
2.2 Experimental 41
2.2.1 Materials 41
2.2.2 Exposure conditions 42
2.2.3 Experimental techniques 44
2.2.3.1 Optical microscopy and hardness measurements 44
2.2.3.2 Scanning electron microscopy 45
2.2.3.3 Microprobe analyses 45
2.2.3.4 Transmission electron microscopy 46
2.2.3.5 Synchrotron X-ray diffraction 48
2.3 References 52

PART III

Metallurgical investigation of metal dusting corrosion in plant exposed nickel-based alloy 602 55

3.1 Introduction 57
3.2 Experimental 57
3.3 Results and discussion 58
3.3.1 Microstructure near the alloy surface 58
3.3.2 Changes in hardness after prolonged high temperature exposure 59
3.3.3 X-ray mapping in FEG SEM 60
3.3.4 Identification of constituent phases close to the corroded surface 61
3.4 Conclusions 63
3.5 References 65

PART IV

Surface disintegration of nickel-based alloys during long time exposure to syngas in an industrial plant for methanol production 67

4.1 Introduction 69
4.2 Experimental 70
4.3 Results 70
4.3.1 Microstructural stability during exposure 70
4.3.2 Phases detected by X-ray diffraction 74
4.3.3 Phases observed in TEM and SEM 77
4.4 Discussion 81
4.4.1 Conditions for α-Cr formation in alloy 693 82
4.4.2 Conditions for α-Cr formation in alloy 602 83
4.4.3 Local phase equilibria at the surface 84
4.4.4 Thermodynamic stability of observed phases 87
4.5 Conclusions 90
4.6 References 93
APPENDIX I S-XRD results and FEG SEM images of the iron-based alloy APMT 97

PART V

A model for metal dusting corrosion in nickel-based alloys involving internal precipitation of carbides, oxides and graphite 101

5.1 Introduction 103
5.2 Experimental 105
5.3 Results 105
5.3.1 Summary of phases detected by synchrotron XRD 106
5.3.2 Microprobe analyses of corrosion pits and their surroundings 107
5.3.3 FEG SEM analyses of the pit/metal interface 110
5.3.4 STEM/TEM analyses of precipitates and corrosion products 113
5.4 Discussion 116
5.4.1 Incubation time for metal dusting corrosion 117

5.4.2 Conditions for oxide formation within the corrosion pits 120
5.4.3 Conditions for carbide formation within the white zone 122
5.4.3.1 Carbide stability 122
5.4.3.2 Extent of carbon intrusion 124
5.4.4 Models for internal carburisation and oxidation 125
5.4.4.1 Carbon diffusion 127
5.4.4.2 Oxygen diffusion 128
5.4.4.3 Quasi-steady state solutions 130
5.4.4.4 Input data used in diffusion models 130
5.4.4.5 Predictions of steady-state corrosion rates 131
5.4.5 Volume changes associated with internal precipitation 133
5.4.5.1 Constitutive equations 133
5.4.5.2 Volume changes within the carburised zone 134
5.4.5.3 Volume changes within the oxidised zone 135
5.4.5.4 Calculated volume changes in alloys 602 and 693 135
5.4.6 Mechanisms of metal dusting corrosion in Ni-based alloys 137
5.5 Conclusions 139
5.6 References 141
APPENDIX II Symbols, formulae and units used in the diffusion models for metal dusting corrosion 146

PART I

General introduction to metal dusting corrosion

1.1. Introduction

Metal dusting corrosion (MD) of metals and alloys is a result of carbon attack at high temperatures (400-800˚C). In general, metal dusting involves diffusion of carbon into the material, formation of carbides, leading, in turn, to decomposition of the alloy into dust consisting of metal particles, coke and other reaction products. An example of pit formation on a drain line of a nickel-based alloy located in a steam superheater caused by metal dusting corrosion is shown in Fig. 1.1.

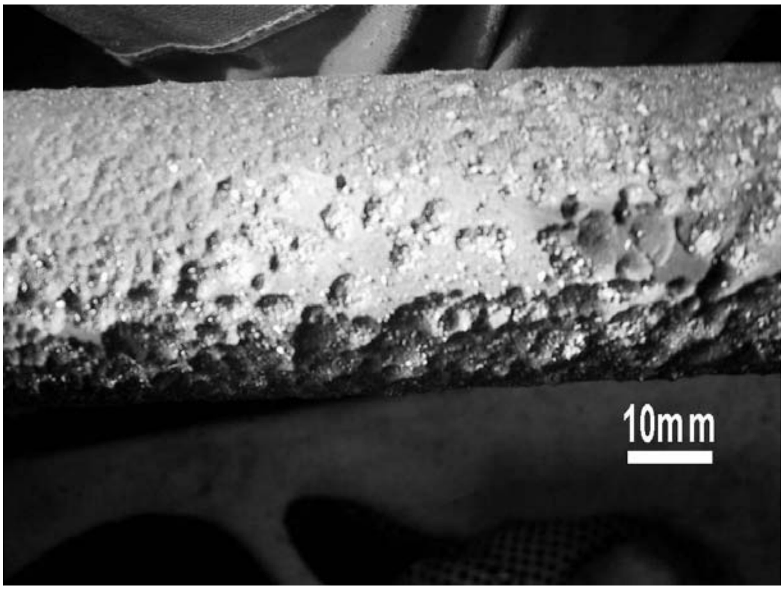

Figure 1.1 Example of pit formation on a drain line of a nickel-based alloy located in a steam superheater caused by metal dusting corrosion.

The phenomenon is complex and the corrosion resistance depends on many factors such as the type of material, the stability of the oxide scale with respect to gas composition, temperature, pressure and time, i.e. both environmental and metallurgical factors. MD is not a new problem, it has been known for more than 100 years[1] and a lot of research in this field has been performed throughout the years. Several researchers have investigated this special form of corrosion, but due to the number of variables involved, a complete understanding of the phenomenon is still lacking.

1.2. Introduction to syngas technology

It is appropriate to start with an introduction to syngas conversion technology in order to put the metal dusting corrosion problem into a proper perspective.

1.2.1. Steps in conversion of natural gas to syngas

Natural gas is a mixture of gaseous hydrocarbons with varying quantities of non-hydrocarbons. It typically consists of 70-90% methane in addition to other higher hydrocarbons (ethane, propane and butane) and small amounts of CO_2, N_2, H_2S and He, which are normally considered impurities.[2] The use of natural gas can be divided into the following main categories; i.e. re-injection into oil reservoirs for increased oil recovery, transport to gas markets [i.e. pipeline, compressed natural gas (CNG) or liquefied natural gas (LNG)], local production of heat and power and chemical conversion to other energy carriers or bulk chemical products (hydrogen, ammonia, methanol, Fischer-Tropsch fuels, etc). However, only applications involving gas conversion are of interest here.

Most gas conversion technologies require the production of synthesis gas (syngas) as an intermediate step. The most relevant technologies for production of syngas are conventional steam reforming (CSR) which is the same as tubular reforming, auto-thermal reforming (ATR), gas-heated steam reforming (GHR), partial oxidation (POX) and different combinations of these.[3] An example of a process route based on two step reforming (i.e. CSR + oxygen blown secondary reforming) covering the production of methanol from natural gas via syngas is shown in Fig. 1.2.

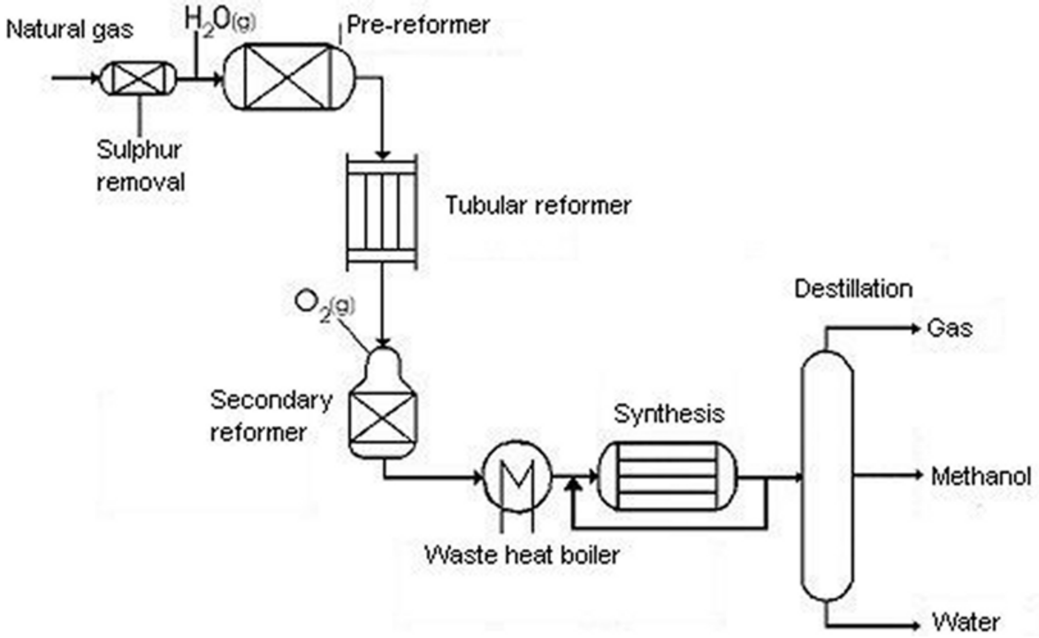

Figure 1.2 Sketch of the different steps in conversion of natural gas to syngas and methanol, based on two step reforming (i.e. CSR + secondary reforming).

The natural gas is transported into the plant where sulphur is removed because of its ability to poison the catalyst. In the pre-reformer, higher hydrocarbons are converted by steam reforming into C_1 components, mainly methane (CH_4) and carbon oxides, mainly CO_2. The gas holds a temperature around 600˚C before entering the tubular reformer (CSR) where steam reforming of methane takes place. In the oxygen blown secondary reformer, hydrogen is combusted with oxygen in the gas phase, followed by reforming on a catalyst bed. At these high temperatures, the equilibrium, according to reaction (1.1), is shifted to the right towards higher CO (g) and H_2 (g) contents:

$$CH_4 + H_2O \leftrightarrow CO(g) \; + 3H_2(g) \tag{1.1}$$

Since it is the CO and H_2 contents in the gas that are requested, the syngas is first quenched in a waste heat boiler to temperatures around 600˚C and further down to 40˚C to remove the remaining H_2O. In a methanol plant, cold syngas is transported to a syngas reactor where the gases react in exact ratio forming raw-methanol. The raw-methanol is further distilled to remove contaminations.

1.2.2. Plant operating conditions

Developments in the oil and gas industry are closely linked to the application of natural gas conversion technology. Currently, new plant concepts and designs are adopted to reduce both capital and operating costs. In particular, it is important to reduce the steam content in the process gas, while increasing the overall reforming capacity in order to make natural gas reforming more economical and ecological feasible. When excess steam is removed from the process, there will be more space for natural gas, meaning that the steam-to-carbon ratio is reduced. Decreasing the steam-to-carbon ratio has two main technical risks associated with it. Firstly, the potential for coke formation in the preheating and reforming sections of a syngas unit will increase. Secondly, the risk for metal dusting corrosion in heat recovery equipment will be higher.

When the process capacity increases, the process parameters will change and become more demanding from a materials point of view. Materials selection is therefore critical and must be optimised in order to avoid problems during subsequent plant operation. Firstly, the materials need to have a high creep resistance and yield strength at elevated temperatures, depending on where in the plant they are used. In addition, the corrosion resistance of the different materials has to be considered.

As already mentioned metal dusting corrosion is a result of carbon attack in the temperature range from 400 to 800˚C. Current practice is therefore to design syngas heat recovery equipment to avoid this temperature range, but since this is not the best solution considering the energy efficiency, there are still components that are required to operate at these temperatures. For such components, attempts are made to select the best available materials. However, because corrosion attacks cannot readily be avoided, the designs are often such that replacement is relatively easy.

1.2.3. The use of nickel-based alloys

In the past, significant research has been carried out to develop nickel-based alloys with improved high temperature corrosion resistance. In the following, a brief review of commonly used alloys in plants for syngas production will be given. Metal dusting corrosion in connection with nickel-based alloys will be presented later.

The nickel-based alloys being exposed to temperatures in the metal dusting corrosion range are mainly located close to the waste heat boiler shown in Fig. 1.2. These contain nickel as the main element and high amounts of chromium. In addition, a wide range of other elements are added to obtain the desired microstructure and properties at elevated temperatures. Table 1.1 shows the typical compositional range for nickel-based alloys.[4]

Table 1.1 Typical compositional range for nickel-based alloys, in wt%.[4]

Element	Cr	Ni	Mo,W	Al	Ti	Co	Nb	Ta	Re
Content (wt%)	5-25	Bal.	0-12	0-6	0-6	0-20	0-5	0-12	0-6

1.2.3.1. Phase relations and microstructural stability

Figure 1.3 shows the binary nickel-chromium phase diagram. It is evident that at chromium contents below 30wt%, γ-Ni is the only stable phase at temperatures above 590˚C. At higher chromium contents, the two phase region is entered, leading to precipitation of α-Cr. Therefore, based on the composition data presented in Table 1.1, the matrix (γ-phase) in nickel-based alloys should be austenitic with a face-centered cubic (fcc) crystal structure and atomic arrangement as illustrated in Fig. 1.4 (a). Similarly, the phase diagram predicts that α-

Cr does not form when the Cr-content is below 30 wt% at 590˚C, which is higher than the typical max Cr-content in these alloys as seen from Table 1.1. The α-Cr phase has the body centered cubic (bcc) crystal structure and the atomic arrangement shown in Fig. 1.4 (b).

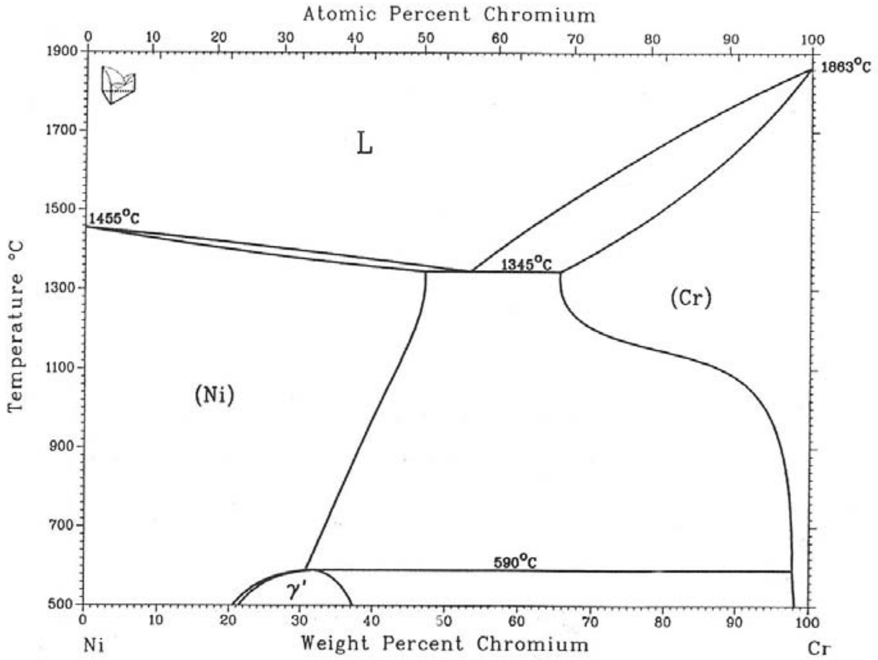

Figure 1.3 The binary Ni-Cr phase diagram.[5]

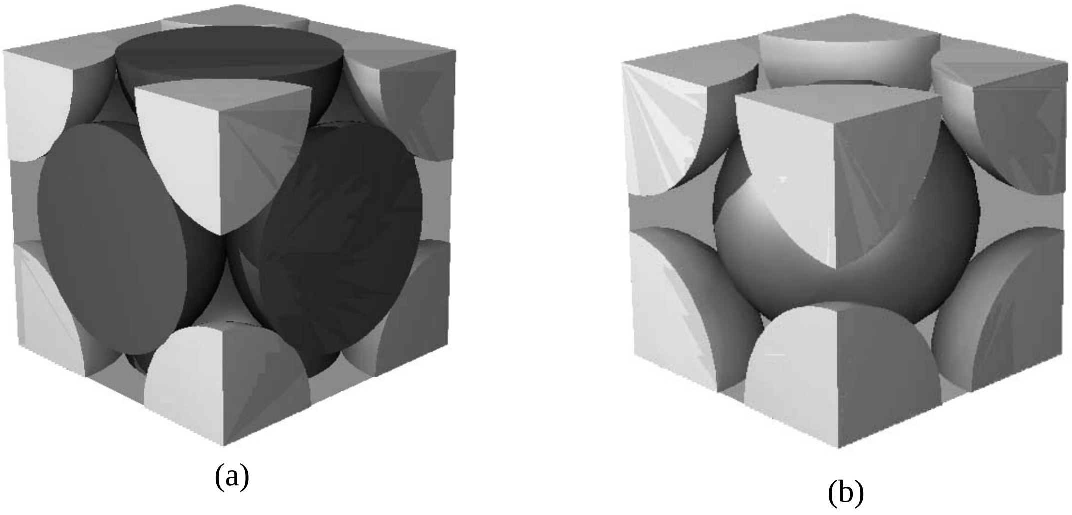
(a)

(b)

Figure 1.4 Schematic drawings of the atomic arrangement in different cubic phases; a) the γ-Ni (fcc) phase, b) the α-Cr (bcc) phase.

It should be noted that the above conclusion is based on a consideration of the binary Ni-Cr phase diagram. More refined calculations, using Thermo-Calc, have shown that the content of other alloying elements such as Al, Ti, W and Fe may strongly influence the precipitation kinetics by increasing the equilibrium temperature at which α-Cr forms.[6] This effect is shown in Fig. 1.5. It follows that both W and Fe will enhance this temperature because they partition to the γ-Ni phase and substitute for Ni in the same way as Cr does. This, in turn, decreases the solubility of Cr in γ-Ni and favours α-Cr precipitation at higher temperatures.

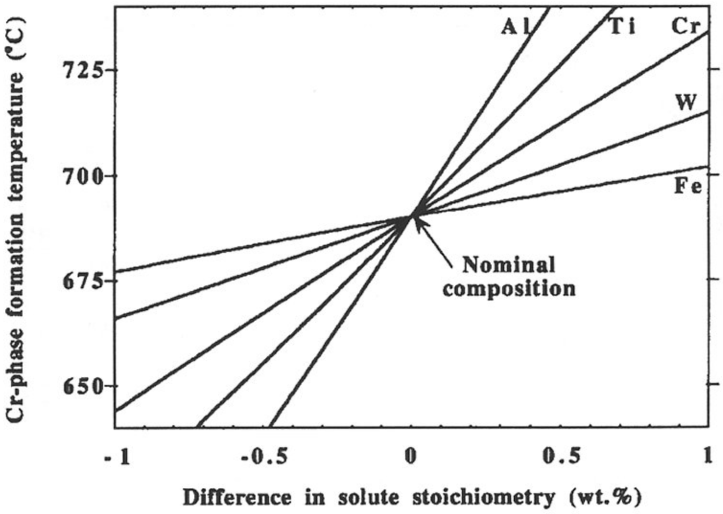

Figure 1.5 Predicted change in the equilibrium formation temperature of α-Cr in a given nickel-based alloy when the Al, Ti, Cr, W or Fe content is varied around the nominal composition. The nominal alloy composition is: Ni-20Cr-3.5W-2.3Al-2.1Ti-5Fe-0.4Si-0.07C-0.005B (in wt %). After Tancret and Bhadeshia.[6]

Also Al and Ti are seen to raise the equilibrium formation temperature of α-Cr in nickel-based alloys, also shown in Fig. 1.5. However, their effect is different, as both elements partition to the intermetallic γ′-Ni phase (appearing in Fig. 1.3) at temperatures below 590˚C), where they form secondary intermetallics of the Ni_3(Al, Ti) type. This precipitation drains Ni from the primary γ-Ni matrix and decreases the total amount of the γ-Ni phase. As a result, the Cr content in it increases, leading again to enhanced α-Cr precipitation.

Finally, it should be mentioned that α-Cr precipitation has not actually been observed in nickel-based alloys,[6] although it's existence is predicted thermodynamically. This may be because the precipitation involves the growth of a bcc phase within a fcc lattice. Hence, the associated kinetics might be so slow that the reaction is not triggered under normal service temperatures and plant operating conditions.

1.2.3.2. Structure-property relationships

The most important aspect of the alloying element additions is to improve the high-temperature properties through control of the microstructure. However, some elements can contribute to the formation of undesirable phases like σ, μ and Laves. Others again, like Al and Ti, react with nickel and precipitate as secondary intermetallics forming the hardening γ'-phase. This phase increases both strength and the creep resistance of the material. Moreover, the γ'' phase can form in certain nickel-based alloys containing niobium and iron, which is a third type of intermetallics. The Ni_3Nb precipitates are found to be coherent with the γ-Ni matrix. The γ'' phase provides a very high strength at low to intermediate temperatures, but is unstable above 1200K (927˚C). Also a wide variety of different carbides can form, depending on the alloy composition and heat treatment conditions. The important types are MC, M_6C, $M_{23}C_6$ and M_7C_3, where M denotes Cr, Mo, W, Nb or Ti. In nickel-based alloys chromium carbides are most commonly observed. In addition, borides can form when boron segregates to grain boundaries. Generally, boride phases, in small amounts, are favourable because they improve the creep-rupture strength.[4]

Table 1.2 Nominal compositions of the four alloys; 600, 601, 602 and 693.[14, 15]

Alloy	600 (UNS N06600)		601 (UNS N06601)		602 (UNS N06025)		693 (UNS N06693)	
Element	min	max	min	max	min	max	min	max
Ni	72*	-	58	63	bal.	-	bal.	-
Cr	14	17	21	25	24	26	27	31
Fe	6	10	bal.	-	8.0	11.0	2.5	6
Al	-	-	1.0	1.7	1.8	2.4	2.5	4.0
C	-	0.15	-	0.1	0.15	0.25	-	0.15
Mn	-	1.0	-	1.0	-	0.1	-	1.0
Si	-	0.5	-	0.5	-	0.5	-	0.5
Cu	-	0.5	-	1.0	-	0.1	-	0.5
Nb	-	-	-	-	-	-	0.5	2.5
Ti	-	-	-	-	0.1	0.2	-	1.0
Y	-	-	-	-	0.05	0.12	-	-
Zr	-	-	-	-	0.01	0.1	-	-

* Value includes both Ni and Co.

In recent years there has been increased emphasis on the content of certain oxide forming elements, especially chromium and aluminium, to prevent metal dusting degradation in nickel-based alloys.[7-9] The traditional materials used in primary and secondary reformers are alloy 600 and alloy 601.[10] These alloys contain high amounts of nickel and chromium, but the modified versions; alloy 602[11, 12] and alloy 693[13] are even higher in chromium and contain aluminium as well. The main objective of these element additions is to create a dense oxide layer that effectively protects the material from degradation during service at high temperatures. Table 1.2 shows the nominal chemical compositions of these four alloys. The delicate balance between the strong carbide and oxide formers in the alloys is obvious from the tabulated data. In particular, it is noted that alloy 602, in addition to aluminium, also contains yttrium and zirconium. Yttrium is known to be an extremely strong oxide forming element.

1.2.4. Reported failure cases in plants for syngas production

Several failure cases due to metal dusting degradation have been reported throughout the years. Already in 1959, Eberle and Wylie[16] reported an attack on two iron-based materials containing 18Cr-8Ni and 25Cr–20Ni, respectively. The materials were in contact with hot syngas in a waste heat boiler and just after 3 weeks of operation it failed. Testing was then carried out using nickel-based alloys and they proved to perform better under the prevailing conditions. Eberle and Wylie therefore concluded that nickel-based alloys should be used in preference of iron-based alloys in critical parts exposed to syngas.

Later, in a methane reforming plant in South Africa a failure case was reported in 1996 by Holland and de Bruyn.[17] Here, methane rich natural gas was reformed to syngas by combined reforming technology; CSR and ATR. Metal wastage of a section of a burner line caused partial collapse of the liner, leading to blockage of some of the burner gas vanes. This led to failure, as a result of metal dusting corrosion attacks on a component of alloy 600 after 18 months of exposure. Figure 1.6 shows an image of the attacked alloy welded onto the unattacked alloy 800. In the specific environment investigated, alloy 800, which is iron-based (containing 32wt%Ni, 21wt%Cr, 44wt%Fe and 0.5wt%Al) showed better resistance against metal dusting corrosion compared to alloy 600. This observation is quite surprising and appears to be in conflict with that reported by Eberle and Wylie.[16] A possible explanation is that alloy 800 is more balanced with respect to chromium and aluminium compared to alloy 600, thereby making it more resistant to metal dusting corrosion attacks.

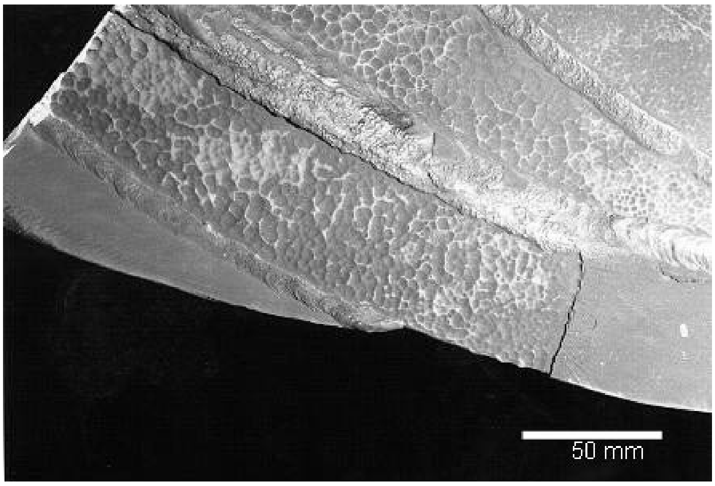

Figure 1.6 Metal dusting pitting attack on alloy 600 adjacent to the undamaged alloy 800. From Holland and deBruyn.[17]

Another failure case, as a result of metal dusting corrosion attacks on a heat exchanger for syngas, has been reported by Grabke.[18] The material used in the heat exchanger was the iron-based alloy 800 and it failed after 32 months of exposure at temperatures in the range between 350 and 575˚C. A cross section micrograph of the attacked alloy is shown in Fig. 1.7. The picture is therefore quite confusing, the iron-based alloy 800 is seen to be susceptible to metal dusting corrosion, as opposed to that reported by Holland and de Bruyn.[17]

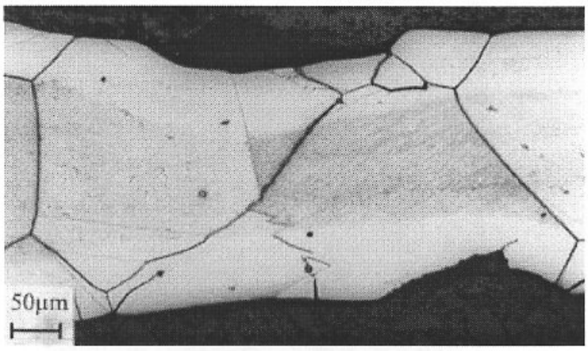

Figure 1.7 Metal dusting corrosion attack on alloy 800. From Grabke.[18]

These few examples presented above illustrate the complexity of the materials problems involved in metal dusting corrosion. For example, a specific alloy can behave well in certain environments, but fail in others. There are many explanations to this behaviour. Obviously, the resistance to metal dusting corrosion depends on the interplay between a number of variables, which cannot readily be accounted for in a mathematical simulation of the process. Of particular importance in this respect is the role of minor elements, i.e. strong oxide and carbide formers, either present in the gas phase or contained in the parent material. These aspects will be further discussed in the following sections.

1.3. Thermodynamics and kinetics relevant to metal dusting corrosion

According to Grabke,[19] metal dusting corrosion may occur when gases with carbon activity greater than one react with the alloy. Generally speaking, the extent of this gas/metal interaction depends both on the thermodynamics[20, 21] and the kinetics of the systems, which, unfortunately, in most cases are difficult to predict.

Normally, diffusion of reactants towards the gas/metal interface leads to local equilibrium, as indicated in Fig. 1.8, while global equilibrium between the bulk phases is less likely to establish. Although this largely complicates the picture, several important points can be deduced from a simplified analysis of the carbon and oxygen activities in the bulk gas and metal phases. Therefore, it is appropriate to proceed with some key definitions and reactions that are essential to the understanding of metal dusting corrosion in metals and alloys under operating conditions applicable to syngas production.

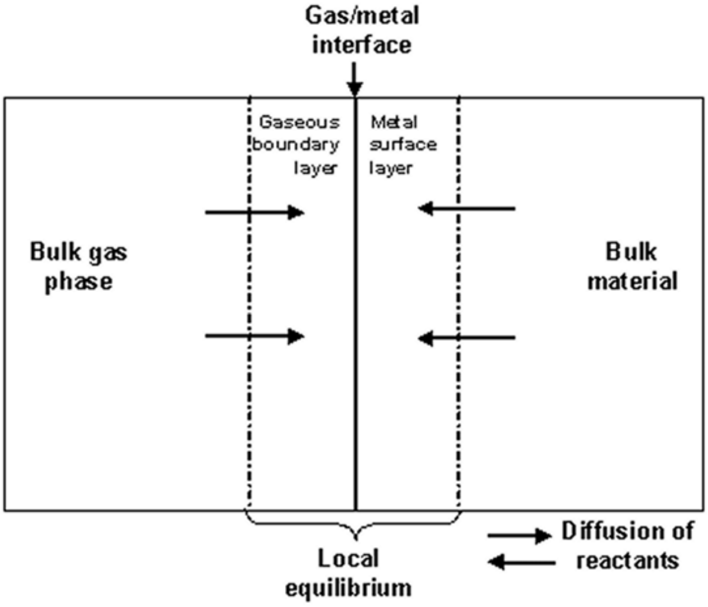

Figure 1.8 Schematic diagram illustrating the concept of local equilibrium where diffusion of reactants towards the gas/metal interface becomes the rate controlling step.

1.3.1. Carbon activity in the gas phase

Usually, gas mixtures causing metal dusting corrosion contain carbon monoxide (CO), hydrogen (H_2), steam (H_2O), carbon dioxide (CO_2) and methane (CH_4). A full thermodynamic analysis of the carbon activity in such complex industrial gases is difficult. However, a simplified analysis is straight forward by considering the main reactions that cause graphite formation, i.e. the Boudouard reaction (1.2) and the CO decomposition reaction (1.3):

$$2CO\left(g\right) = CO_2(g) + C_{(gr.)} \tag{1.2}$$

and

$$CO\left(g\right) + H_2\left(g\right) = H_2O\left(g\right) + C_{(gr.)} \tag{1.3}$$

It follows from equation (1.2) that:

$$a_{C(gr.)} = K_{1.2}\frac{p_{CO}{}^2}{p_{CO_2}} \tag{1.4}$$

and from equation (1.3) that:

$$a_{C(gr.)} = K_{1.3}\frac{p_{H_2}p_{CO}}{p_{H_2O}} \tag{1.5}$$

where $K_{1.2}$ and $K_{1.3}$ are the corresponding equilibrium constants for the reactions.

In real industrial systems the volume fractions X_i of the gaseous components and the total pressure p_{tot} are usually known. Therefore, instead of using the mole fraction, it is more convenient to express the partial pressures of the different gaseous components in terms of X_i and p_{tot}, taking for example $p_{CO} = X_{CO} \times p_{tot}$. Equations (1.4) and (1.5) can then be rewritten as:

$$a_{C(gr.)} = K_{1.2}\frac{X_{CO}{}^2}{X_{CO_2}}p_{tot} \tag{1.6}$$

$$a_{C(gr.)} = K_{1.3}\frac{X_{H_2}X_{CO}}{X_{H_2O}}p_{tot} \tag{1.7}$$

Data for the equilibrium constants $K_{1.2}$ and $K_{1.3}$ can be obtained from well-established reference sources.[22]

By way of example, the syngas composition in Table 1.3 will be used in calculations of the carbon activity. Two different values for the total pressure are assumed, i.e. p_{tot} equal to 1 and 35 bar, respectively, the latter value being representative of an industrial environment.

Table 1.3 Assumed syngas composition (in vol%).

Component	CO	H_2	CO_2	H_2O	CH_4
Content (vol%)	14.9	47.3	5.7	31.2	0.9

Figure 1.9 (a) and (b) show plots of the carbon activity versus temperature under these conditions, based on equations (1.6) and (1.7), respectively. It is evident that the carbon activity in the gas phase is both a function of temperature and the total pressure. Generally, the Boudouard reaction yields higher $a_{c(gr.)}$ values than the CO decomposition reaction. However, since the latter reaction is kinetically favourable compared to equation (1.2), the CO decomposition reaction is normally considered to be determining for the carbon activity in the gas phase at temperatures typical for metal dusting.[19]

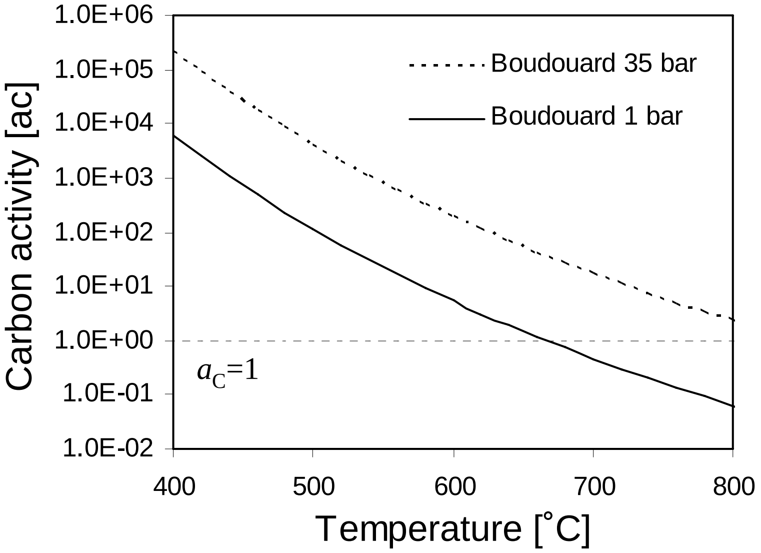

(a)

Figure 1.9 Plots of the carbon activity versus temperature; a) based on the Boudouard reaction, b) based on the carbon decomposition reaction. Input data from Table 1.3 and Kubaschewski and Alcock.[22]

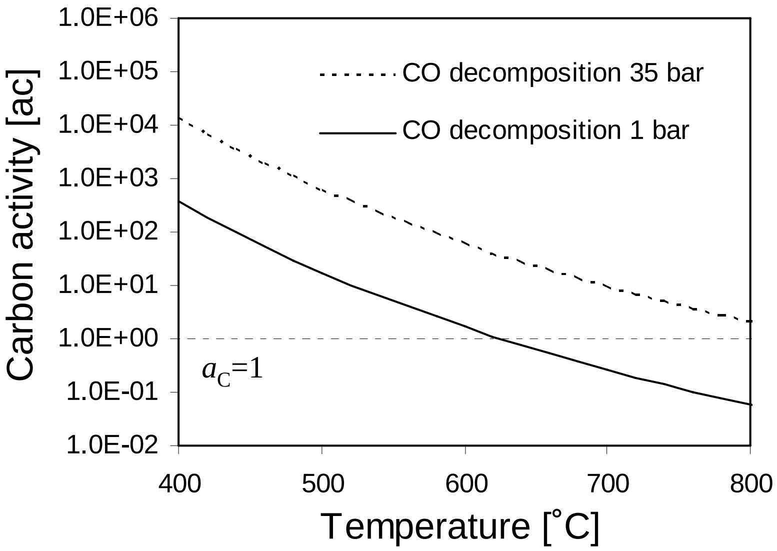

(b)

Figure 1.9 Continued.

Note that the plots in Fig. 1.9 assume that no graphite formation occurs, i.e. the calculated $a_{c(gr.)}$ values define the aggressiveness of the gaseous environment or more precisely the carburising potential in the absence of graphite. As soon as the Boudouard or CO decomposition reaction is triggered and pure graphite forms at the exposed metal surface, the carbon activity drops to unity by definition. Further carburisation of the material must then proceed at a carbon activity close to unity, which makes metal dusting corrosion in pure iron rather complicated to explain from a thermodynamic point of view. This will be discussed in Section 1.4.1.

1.3.2. Conditions for carbide formation

Several factors contribute to the formation of carbides. In carburising atmospheres at high pressures, as experienced in industrial syngas production, the material will be attacked by carbon. As soon as the oxide layer is broken, carbon will start to penetrate the material and form carbides. Which type of carbide that forms will depend on the carbon activity and the content of carbide formers in the base material.

In metal dusting corrosion the thermodynamic stability of both iron carbide and chromium carbides is of specific interest. The most commonly observed chromium carbides are Cr_3C_2,

Cr_7C_3 and $Cr_{23}C_6$. If the composition of the latter carbide is simplified to Cr_4C, the relevant decomposition reactions can be written as;

$$Fe_3C \rightarrow 3Fe + C \tag{1.8}$$

$$Cr_3C_2 \rightarrow 3Cr + 2C \tag{1.9}$$

$$Cr_7C_3 \rightarrow 7Cr + 3C \tag{1.10}$$

$$Cr_4C \rightarrow 4Cr + C \tag{1.11}$$

By introducing the equilibrium constants for the reactions, taking the activities of the carbide and metal phases equal to unity, the corresponding expressions for the carbon activity at the onset of dissolution become:

$$a_c = K_{1.8} \tag{1.12}$$

$$a_c = (K_{1.9})^{\frac{1}{2}} \tag{1.13}$$

$$a_c = (K_{1.10})^{\frac{1}{3}} \tag{1.14}$$

$$a_c = (K_{1.11}) \tag{1.15}$$

Figure 1.10 shows plots of the calculated carbon activities for carbide formation for a limited range in temperature, using data from Kubaschewski and Alcock.[22] It is evident that the carbon activity associated with Fe_3C formation has a value greater than one within the entire temperature range relevant to metal dusting corrosion. However, since the equilibrium constant for the decomposition reaction is a weak function of temperature, the carbon activity is seen to slightly decrease with increasing temperatures. Nonetheless, these results show that Fe_3C is not stable in the presence of graphite, but requires that the steel is exposed to a carburising gas with $a_c > 1$ in order to form.

In contrast, the carbon activity associated with chromium carbide formation is significantly lower than one. This means that the carbides are stable in the presence of graphite. In general, the most stable carbide Cr_4C yields the lowest a_c - value at a given temperature, while the less stable ones yield higher values. Also the a_c - temperature dependence is completely opposite to that observed for Fe_3C, reflecting the fact that the equilibrium constants for the pertinent decomposition reactions are monotonically increasing with T.

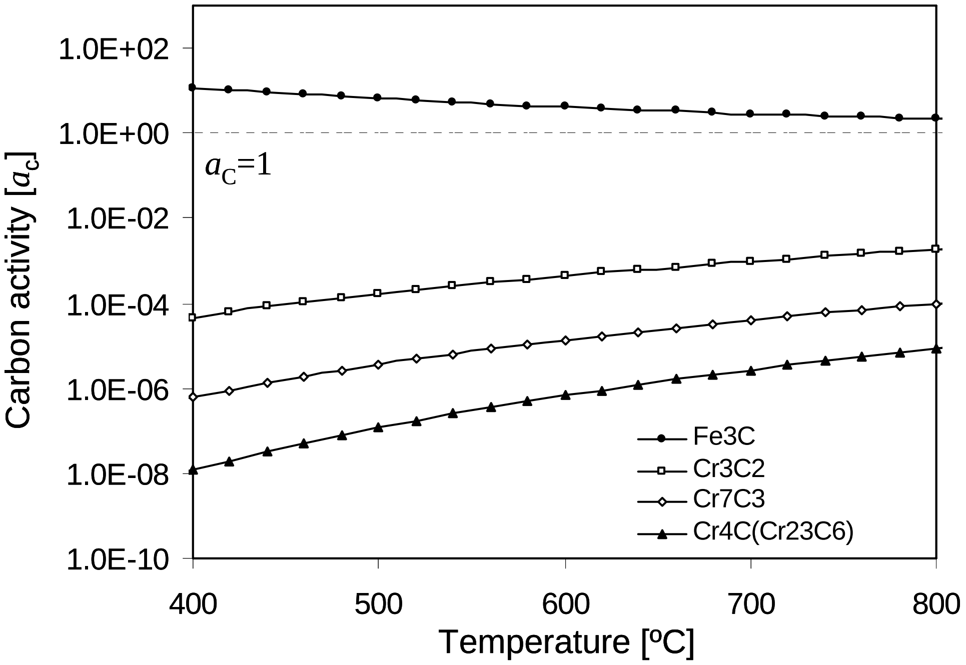

Figure 1.10 Predicted thermodynamic stability of different carbides as function of temperature. The calculations are based on equations (1.12) to (1.15) using input data from Kubaschewski and Alcock.[22]

The practical implications of these differences in the carbide stability are summarised in Fig. 1.11. Fig. 1.11 (a) shows a sketch of the carbon activity gradient, starting from the surface of the steel covered with pure graphite and into the bulk, passing through a region adjacent to the steel surface being rich in Fe_3C. It follows that the Fe_3C phase will not be stable in the presence of graphite, but readily dissolves by diffusion because the carbon activity associated with Fe_3C formation is greater than one. As a result, smoothening of the carbon activity curve will occur with time, leading to the steady-state profile shown in Fig. 1.11 (a). If chromium is present in the steel or alloy, the situation is different. As illustrated in Fig. 1.11 (b), all three chromium carbides will be thermodynamically stable in the presence of graphite and precipitate within distinct regions in the sequence Cr_3C_2, Cr_7C_3 and Cr_4C with increasing distance from the metal surface. Far into the bulk, the Cr_4C phase (synonymous with $Cr_{23}C_6$) is the stable precipitate.

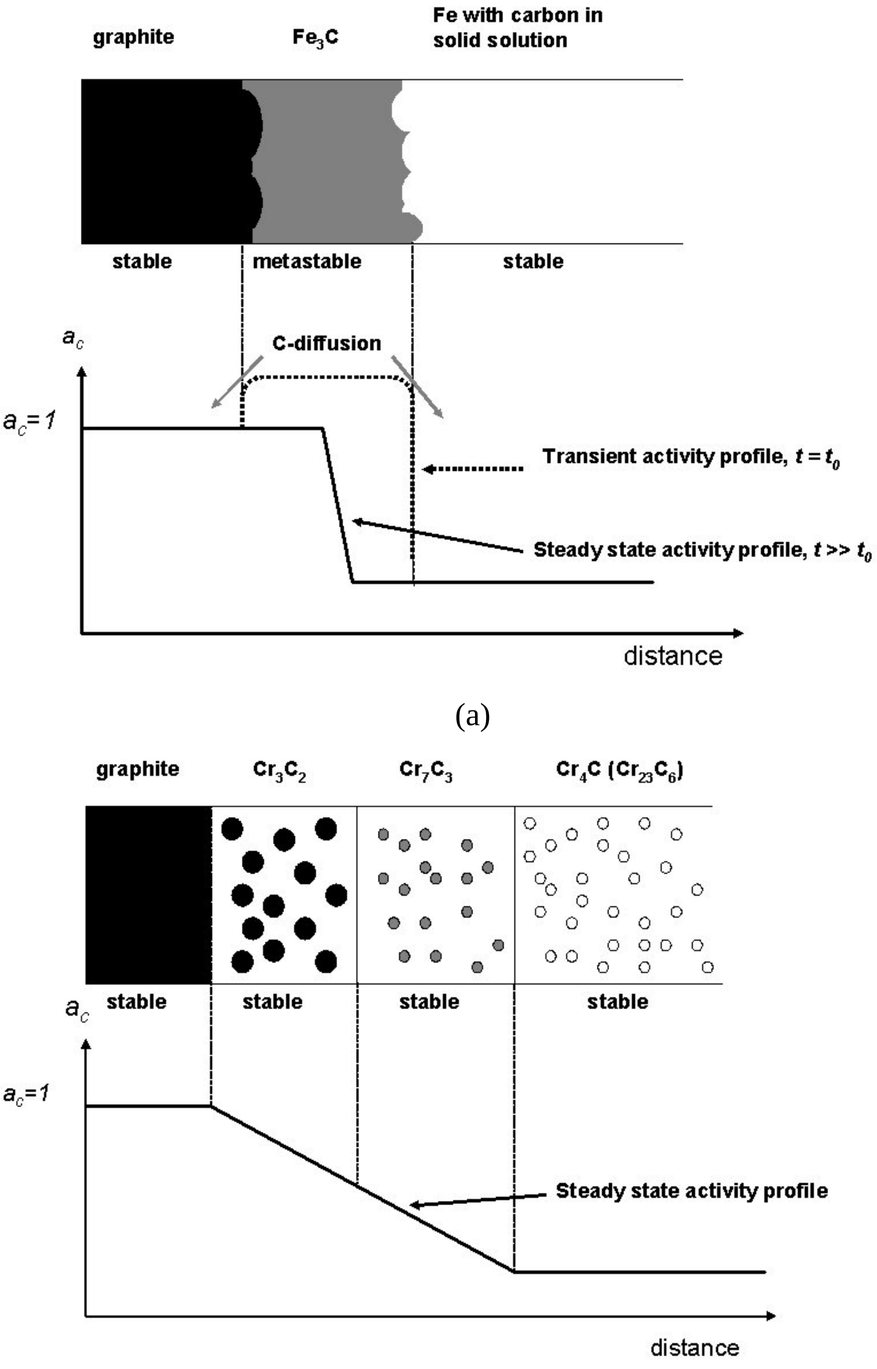
graphite
Fe_3C
Fe with carbon in solid solution
stable
metastable
stable
a_c
C-diffusion
$a_c=1$
Transient activity profile, $t = t_0$
Steady state activity profile, $t >> t_0$
distance
graphite
Cr_3C_2
Cr_7C_3
Cr_4C ($Cr_{23}C_6$)
a_c
stable
stable
stable
stable
$a_c=1$
Steady state activity profile
distance

(a)

(b)

Figure 1.11 Schematic diagrams relating the stability of different carbides to the steady state carbon activity profiles developed following graphite decomposition at the surface of the exposed steel/alloy; (a) Fe_3C in plain carbon steel, (b) Chromium carbides in Cr-containing steels or nickel-based alloys.

1.3.3. Conditions for surface oxide formation

The oxygen partial pressure in the gas phase will determine the type and nature of the oxide layer which forms on the surface of the material during plant exposure. Again, a full thermodynamic analysis of the problem is beyond the scope of the present treatment, but an order of magnitude assessment can be done on the basis of equations (1.16) and (1.17);

$$H_2O = \frac{1}{2}O_2 + H_2 \tag{1.16}$$

$$CO_2 = \frac{1}{2}O_2 + CO \tag{1.17}$$

from which

$$p_{O_2} = \left(K_{1.16} \frac{X_{H_2O}}{X_{H_2}} \right)^2 \tag{1.18}$$

and

$$p_{O_2} = \left(K_{1.17} \frac{X_{CO_2}}{X_{CO}} \right)^2 \tag{1.19}$$

Plots of the calculated partial pressures of oxygen as a function of temperature within the range from 400 to 800˚C are shown in Fig. 1.12, using input data from Table 1.3 and Kubaschewski and Alcock.[22]

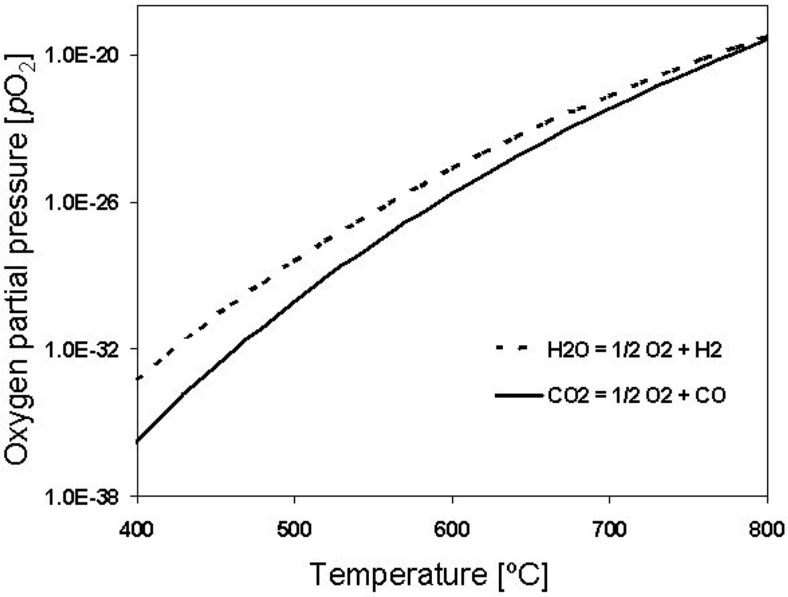

Figure 1.12 Plots of calculated oxygen partial pressures vs temperature. Input data from Table 1.3 and Kubaschewski and Alcock.[22]

Figure 1.12 shows that the oxygen partial pressure, for a fixed gas composition, is a strong function of temperature, varying from 10^{-36} to 10^{-20} atmospheres over the temperature range normally applicable to metal dusting corrosion. Therefore, depending on the content of oxide forming elements in the parent material, a wide variety of surface oxides can form. An illustration of this point is shown in Figure 1.13 which contains plots of the critical partial pressure of oxygen necessary to form Fe_3O_4, Cr_2O_3 and Al_2O_3, according to the pertinent decomposition reactions:

$$Fe_3O_4 = 3Fe + 2O_2 \tag{1.20}$$

$$Cr_2O_3 = 2Cr + \frac{3}{2}O_2 \tag{1.21}$$

$$Al_2O_3 = 2Al + \frac{3}{2}O_2 \tag{1.22}$$

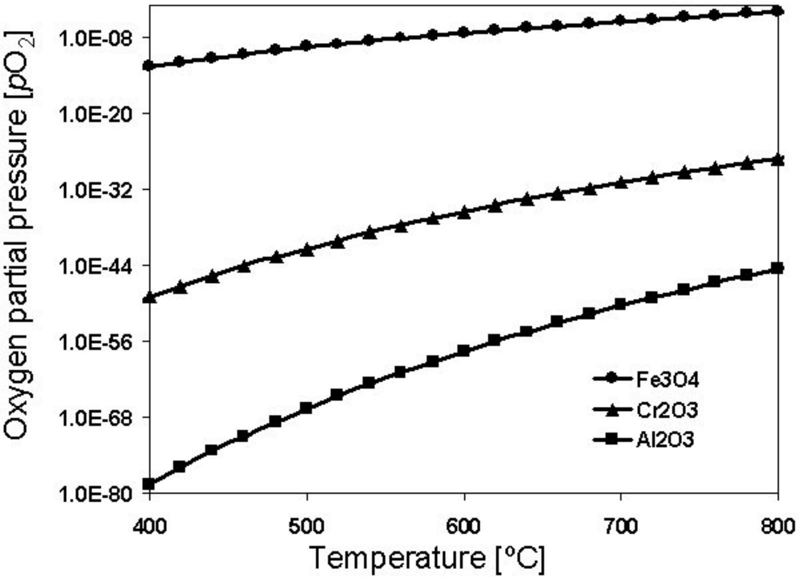

Figure 1.13 Plots of the critical oxygen partial pressures for oxide formation vs temperature for three different oxides; Fe_3O_4, Cr_2O_3 and Al_2O_3. Input data from Kubaschewski and Alcock.[22]

The curves in Figure 1.13 have been constructed by introducing the equilibrium constants for the reactions, taking the activity of the oxide and metal phases equal to unity. Equating with respect to p_{O_2} then gives:

$$p_{O_2} = (K_{1.20})^{\frac{1}{2}} \tag{1.23}$$

$$p_{O_2} = (K_{1.21})^{\frac{2}{3}} \tag{1.24}$$

$$p_{O_2} = (K_{1.22})^{\frac{2}{3}} \tag{1.25}$$

It is evident that Al_2O_3 and Cr_2O_3 will be thermodynamically stable in situations where p_{O_2} varies in the range from 10^{-36} to 10^{-20} atmospheres, corresponding to the exposure conditions described previously in Fig. 1.12. Note that Al_2O_3 will form in preference to Cr_2O_3 if both elements are present in sufficient amounts in the parent material. In contrast, Fe_3O_4 is not a stable phase under the prevailing circumstances, as this would require a much higher p_{O_2} in the gas phase. Considering the important role that the surface oxide layer plays in protecting the material from metal dusting corrosion,[23] the conditions for oxide formation are essential for understanding the metal dusting phenomenon in nickel-based alloys.

1.3.4. Diffusion of reactants in the solid state

So far, the phase formation has been discussed purely on thermodynamical grounds. In practice, rate phenomena will eventually determine the type of reaction product that forms in each case. Still, local equilibrium may prevail, as illustrated previously in Figure 1.8, to an extent which depends on the diffusivities of the reacting elements in the gas or metal phase.

1.3.4.1. Solutions of Fick's law of diffusion

Generally speaking, diffusion is a very complicated matter to deal with since it involves both lattice diffusion as well as element transport along high diffusivity paths such as grain boundaries and dislocation cores.[24] In the following the analysis will be resticted to lattice diffusion of either interstitial alloying elements like carbon or substitutional alloying elements like chromium and aluminium, where the element mobility can be described by the overall diffusion coefficient, defined as:

$$D = D_0 \exp\left(-\frac{Q_d}{RT}\right) \tag{1.26}$$

where D_0 is the pre-exponential factor (with the dimension m^2/s) and Q_d is the apparent activation energy for diffusion (with the dimension J/mol). The other symbols have their usual meaning.

Furthermore, it is assumed that the element transport is driven by the concentration gradient rather than the activity gradient in the material, which means that Fick's 2'nd law of diffusion applies:[25]

$$\frac{\partial C}{\partial t} = \nabla(D\nabla C) \tag{1.27}$$

For the uniaxial case considered in Fig. 1.14, where both the surface concentration C_i and the initial concentration C_0 in the bulk material are fixed, equation (1.27) has the following solution, provided that the model system (here plate) can be regarded as a semi-infinite medium:[25]

$$\frac{C(x,t)-C_0}{C_i-C_0} = 1-erf\left(\frac{x}{\sqrt{4Dt}}\right) \tag{1.28}$$

where x is the position in the plate (in m) and *erf (u)* is the Gaussian error function.

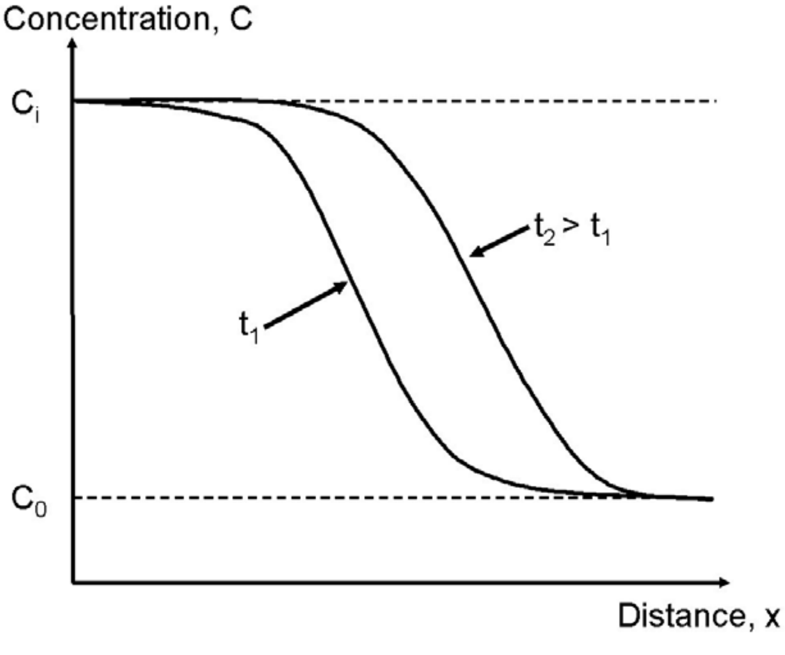

Figure 1.14 Schematic representation of the evolution of the concentration profile with time, as predicted from equation (1.28).

It follows that equation (1.28) applies to the situation where an element of high concentration at the plate surface (e.g. carbon) diffuses into the bulk of the material during long-term exposure at elevated temperatures. Alternatively, if the element transport occurs in the opposite direction, i.e. from the bulk to the plate surface, the appropriate solution becomes:[25]

$$\frac{C(x,t)-C_i}{C_0-C_i}=erf\left(\frac{x}{\sqrt{4Dt}}\right) \tag{1.29}$$

Based on these simple diffusion models it is possible to predict the resulting change in concentration profiles with time for specific alloying elements, provided that the values of D are known. This will provide valuable insight into how far the elements can diffuse under different exposure conditions and whether the thermodynamically stable phases eventually may form or not.

In the following the input data in Table 1.4 will be used to illustrate interstitial and substitutional diffusion in nickel-based alloys. In the former case, a high carbon activity at the gas/metal interface will normally lead to diffusion of carbon into the bulk of the material where it may react with chromium to form different types of carbides (see sketch in Figure 1.11). Conversely, the strong oxide forming elements aluminium and chromium are more likely to diffuse from the bulk and outwards towards the surface because there is a need for a steady supply of the reactants to restore the surface oxide layer.

Table 1.4 Diffusion coefficients for C, Al and Cr in Ni-based alloy.[26]

Austenite (Ni-20Cr-2Al)	C	Al	Cr
D_0 [m^2/s]	1.56 x 10^{-4}	1.35 x 10^{-12}	1.84 x 10^{-4}
Q_d [kJ/mole]	160.680	142.130	278.644

1.3.4.2. Extent of carbon intrusion

The data for D_0 and Q_d in Table 1.4 suggest that the diffusivity of carbon in the austenite lattice is fairly high at the typical operating temperatures for syngas production. For example, at 540˚C, D_C = 7.4 10^{-15} m^2/s, which following substitution into equation (1.28) gives the concentration profiles shown in Fig. 1.15 after 2 and 4 years of exposure, respectively. It is evident from the plots that carbon can readily penetrate 2 to 3 mm into the bulk of the material and cause carbide formation. Although this incident does not necessarily lead to corrosion attacks, the carbon intrusion is highly undesirable from a metallurgical point of view because it will cause material degradation and eventually mechanical failure.

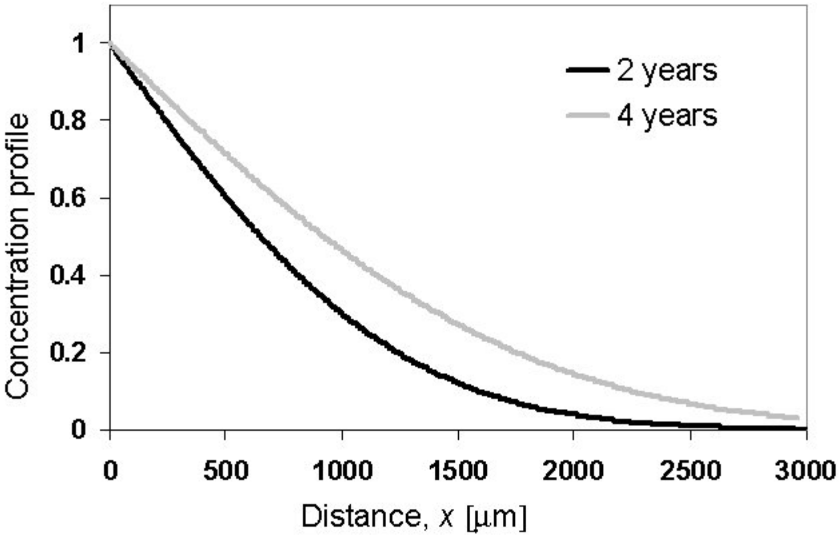

Figure 1.15 Predicted carbon concentration profiles in a Ni-20Cr-2Al alloy after 2 and 4 years of exposure at 540˚C. The calculations are based on equation (1.28) and input data from Table 1.4.

1.3.4.3. Extent of Al and Cr diffusion

One way of preventing carbon from penetrating the material is to maintain a dense (protective) layer of oxide at the surface. As already mentioned, this requires a steady supply of Al and Cr from the bulk to the surface where the elements can react with oxygen present in the gas phase. Unfortunately, the diffusivity of aluminium and chromium in nickel-based alloys is much lower than that of carbon, as indicated by the diffusion data in Table 1.4. This point is more clearly illustrated in Fig. 1.16, which shows plots of the resulting surface concentration profiles of Al and Cr at 540˚C after 2 and 4 years of exposure, respectively. It can be seen that the diffusion distance, in both cases, is in the range from 0.5 to 1 µm, i.e. three orders of magnitude smaller compared to the penetration depth of carbon. Therefore, the possibility of restoring the surface oxide layer by continuous supply of chromium and aluminium from the bulk to the surface is strongly limited in nickel-based alloys and relies on the existence of high diffusivity paths in the material. In practice, this means that the initial grain size or dislocation density in the parent material will eventually determine whether restoration of the surface oxide layer may occur during exposure in a real plant situation.[19, 27, 28]

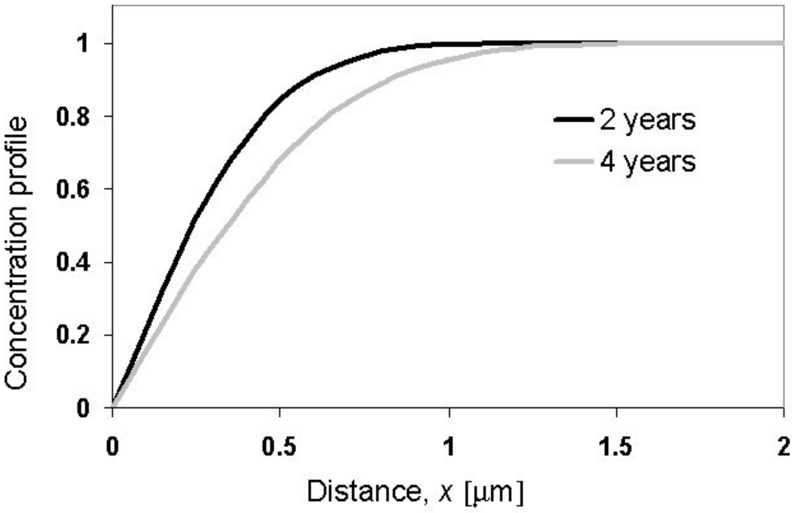

(a)

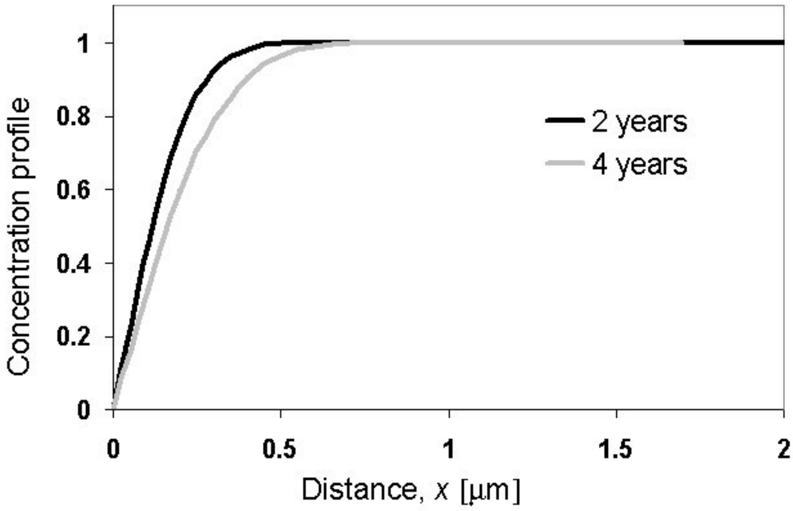

(b)

Figure 1.16 Predicted surface concentration profiles in a Ni-20Cr-2Al alloy of Al and Cr after 2 and 4 years of exposure at 540˚C; a) aluminium, and b) chromium. The calculations are based on equation (1.29) and input data from Table 1.4.

1.4. Models for metal dusting corrosion

In the following, the current models for metal dusting corrosion in low alloyed steels, complex engineering alloys and nickel-based alloys will be briefly reviewed and discussed in the light of the thermodynamics and kinetics of the systems.

1.4.1. Metal dusting corrosion in low alloyed steels

The model for metal dusting (MD) in pure iron and low alloy steels was first presented by Hochman[29, 30] and later refined by Grabke.[31-33] In iron-based alloys the proposed mechanism involves carbon deposition, formation of metastable cementite and further decomposition of this phase into graphite and iron, see Fig. 1.17.

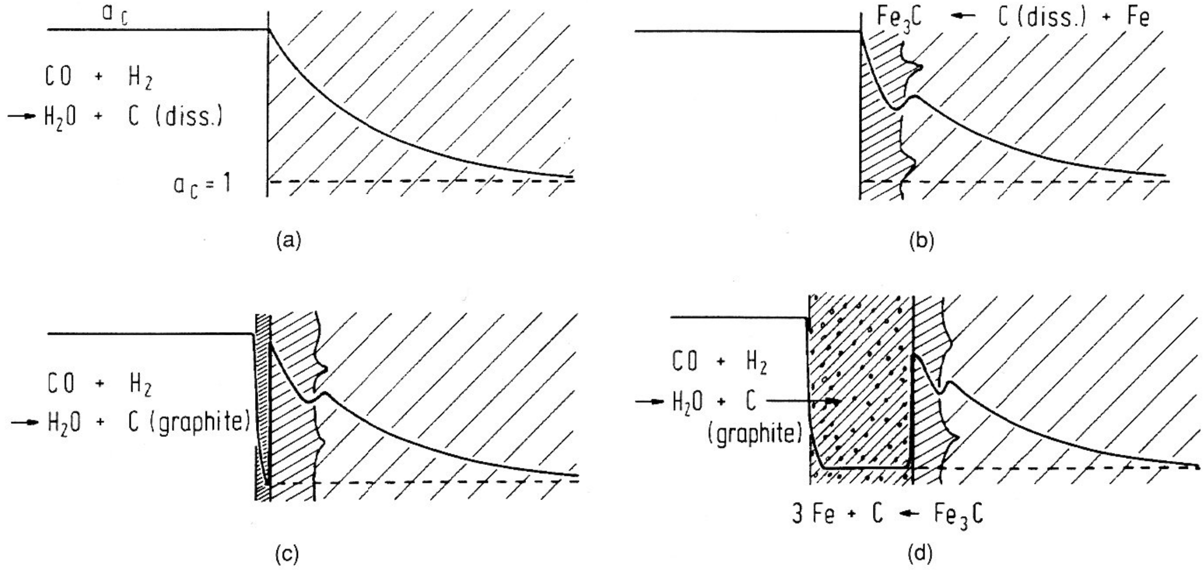

Figure 1.17 Proposed model for metal dusting corrosion in pure iron and low alloyed steels, after Grabke.[32]

The Grabke model assumes that the process occurs in the following steps 1-5;

Step 1) Supersaturation of the metal with dissolved carbon.

Step 2) Precipitation of Fe_3C at the surface and at grain boundaries.

Step 3) Deposition of graphite from the gas atmosphere onto Fe_3C, which is located at the surface.

Step 4) Incipient Fe_3C decomposition, leading to the formation of graphite and metal particles.

Step 5) Further graphite deposition, catalysed by the metal particles.

In step 3, the graphite lattice planes are oriented perpendicular with respect to the cementite surface,[34] which indicates an epitaxial type of growth mode.

The Grabke model is extensively referred to in the scientific literature, and is commonly used to explain the phenomenon of MD in iron-based alloys. Schneider[35] has later pointed out that a step in the MD degradation process presumably involves the growth of iron particles between the cementite- and graphite layers, leading to the formation of a transient layer of iron particles which vanishes again after a certain period. However, the driving force for the iron atoms to move outward through or between the growing graphite flakes and agglomerate into nano-sized particles is unclear.

Other researchers have questioned the model shown in Fig. 1.17, and proposed alternative mechanisms. Recently, Szakálos[36] has pointed out that the MD mechanism in low alloyed steels (shown in Fig. 1.17) requires carbon diffusion in the opposite direction of the carbon activity gradient, which is impossible from a thermodynamic point of view. Instead he proposed a modified MD mechanism, see Fig. 1.18. The first steps are similar to those listed above; i.e. carbon attacks the material, cementite forms on the ferritic surface and graphite forms on the cementite layer. However, because the carbon activity in Fe_3C is higher than the carbon activity in the graphite (see sketch in Fig. 1.11), the former phase will be unstable and start to dissolve. Eventually, it disappears, meaning that the corrosion reaction proceeds by disintegration of the ferrite followed by carbon nanotube formation, as shown in Fig. 1.18.

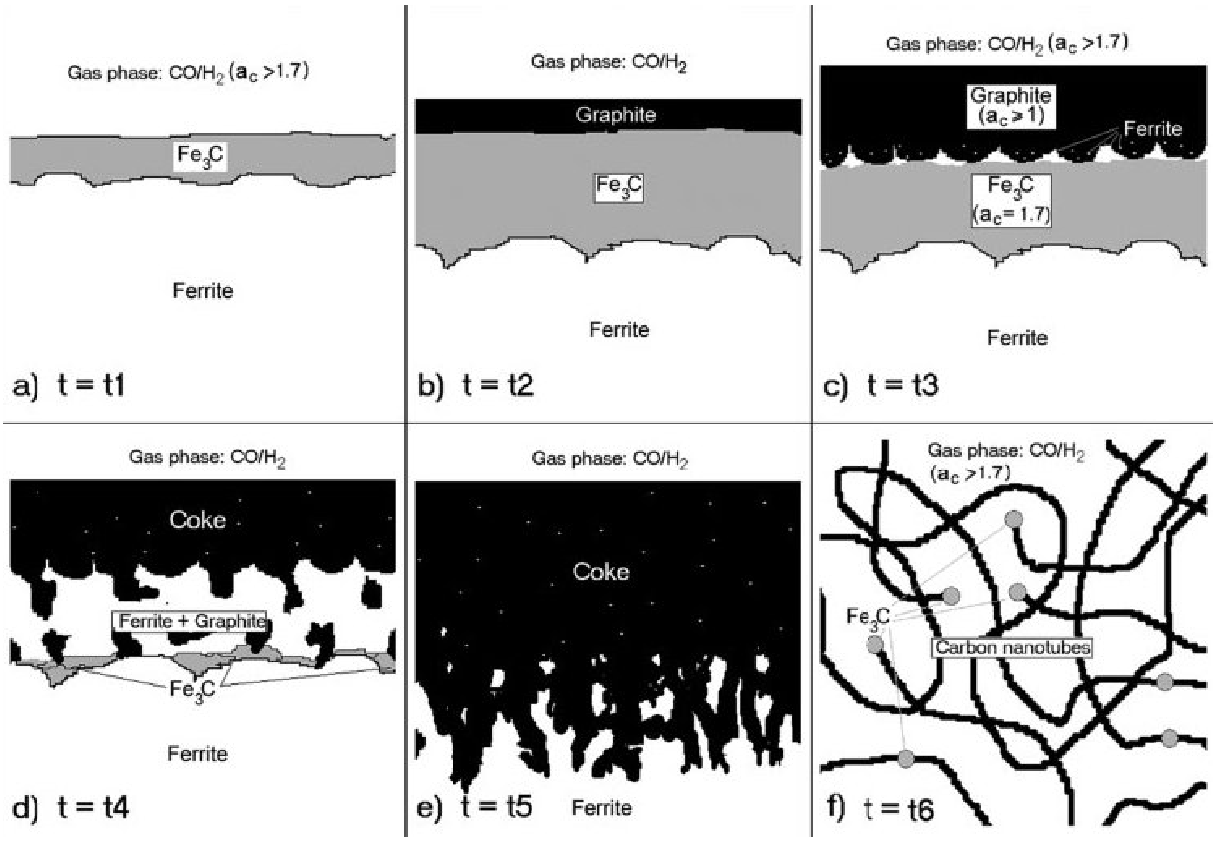
Gas phase: CO/H2 (ac >1.7)
Fe3C
Ferrite
a) t = t1
Gas phase: CO/H2
Graphite
Fe3C
Ferrite
b) t = t2
Gas phase: CO/H2 (ac >1.7)
Graphite (ac>1)
Ferrite
Fe3C (ac= 1.7)
Ferrite
c) t = t3
Gas phase: CO/H2
Coke
Ferrite + Graphite
Fe3C
Ferrite
d) t = t4
Gas phase: CO/H2
Coke
e) t = t5
Ferrite
Gas phase: CO/H2 (ac >1.7)
Fe3C
Carbon nanotubes
f) t = t6

Figure 1.18 Revised model for metal dusting corrosion in pure iron and low alloyed steels, after Szakálos.[36]

1.4.2. Metal dusting corrosion in complex engineering alloys

Complex engineering alloys are in many cases used in environments causing metal dusting corrosion, since they are less susceptible to MD than low alloyed steels.[37] These alloys (which include stainless steels of the 304 type) often have a high content of chromium to form a stable oxide layer. However, the oxide layer is not dense enough to prevent corrosion attacks. The formation of the Cr-rich oxide is dependent on the existence of easy diffusion paths, which is a result of grain size and surface treatment.[38, 39] Figure 1.19 shows a sketch of the mechanism of metal dusting corrosion in complex engineering alloys, as proposed by Grabke.[32]

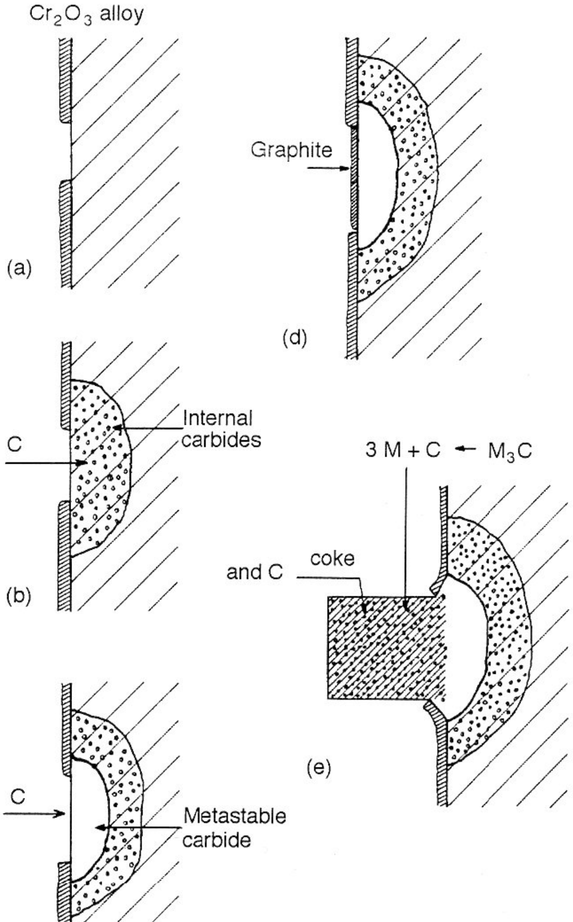

Figure 1.19 Proposed model for metal dusting corrosion in complex engineering alloys, after Grabke.[32]

Referring to Fig. 1.19, the corrosion mechanism can be described by the following steps, a) to e);

Step a) Formation of a local defect in the oxide layer allowing carbon diffusion into the alloy matrix.

Step b) Diffusion of dissolved carbon towards the bulk and subsequent precipitation of stable carbides, e.g $M_{23}C_6$ and M_7C_3 (M=Cr, Fe and Ni).

Step c) Extensive carburisation due to a high carbon activity in the gas phase, leading to nucleation and formation of an unspecified metastable carbide phase, similar to cementite.

Step d) Graphite deposition on the surface. This occurs either by decomposition of the unstable carbide phase to carbon and metal particles or by direct growth of graphite into the bulk of the alloy.

Step e) Further carbon deposition on the metal particles, leading to growth of the carbonaceous protrusions out from the pits.

It follows that the model for metal dusting corrosion in complex engineering alloys is essentially the same as the one proposed for low alloyed steels. However, the major difference is that chromium carbide formation plays a more dominant role in the former case. This makes the model more reliable from a thermodynamic point of view, because chromium carbides (as opposed to cementite) can form at carbon activities lower than one within the material, as shown previously in Fig. 1.10. Hence, the various carbides can grow in a steady state manner in the presence of graphite at the surface, as indicated in Fig. 1.11, which is required for developing corrosion attacks according to the Grabke model.

1.4.3. Metal dusting corrosion in nickel-based alloys

The mechanism of metal dusting corrosion in pure nickel was first described in the literature by Grabke.[40] While MD in iron-based alloys proceeds via formation and disintegration of metastable carbide, it is believed that nickel and nickel-based alloys directly disintegrate, see Fig. 1.20.[41] In nickel-based alloys metal dusting corrosion is assumed to start with decomposition of graphite, while chromium enrichment occurs near the surface, forming Cr_2O_3. Further disintegration of the Cr-free metal may then occur, where termination of reactive graphite lattice planes contributes to the atomistic disintegration of the metal.

Furthermore, in order to explain why the coke layer often contains Ni/Fe and Cr_2O_3 particles, Pippel and co workers[34] have suggested that the metal atoms presumably diffuse through the graphitic layer and agglomerate into particles in the outer reaction zone (coke layer). The graphite lattice planes are oriented perpendicularly to the carbide/metal surface and act as active sites in the disintegration process.[42] The disintegration process proceeds by direct inward or internal growth of the graphite, leading to the formation of larger metal particles (dust) in the coke layer.[43]

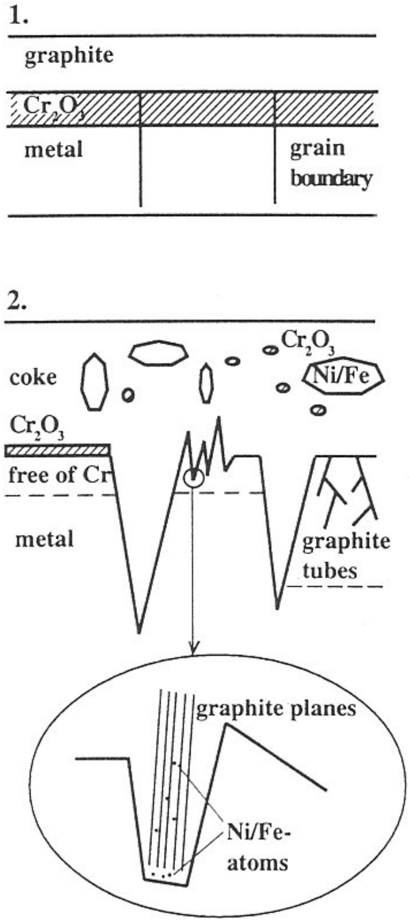
1.
graphite
Cr2O3
metal
grain boundary
2.
Cr2O3
coke
Ni/Fe
Cr2O3
free of Cr
metal
graphite tubes
graphite planes
Ni/Fe-atoms

Figure 1.20 Proposed model for metal dusting corrosion in nickel-based alloys, after Schneider *et* al.[41]

1.4.4. Summary of current knowledge

In spite of the fact that extensive research has been carried out within the field of metal dusting corrosion over the past decades, the mechanism of MD is still controversial and not fully understood, even for the system of pure iron.

Recently, Szakálos[23] has tried to draw the conflicting views and observations into one consistent picture by dividing the metal dusting phenomenon into three main mechanisms, i.e. Type 1, 2 and 3, respectively. Type 1 refers to the transient decomposition of metastable cementite, while Type 2 is the steady state corrosion mechanism which involves the disintegration of the carbon supersaturated ferrite by internal graphitisation, as shown previously in Fig. 1.18. Moreover, Type 3 is a third corrosion mechanism which occurs by selective oxidation of alloyed carbides. This is more in line with the model presented in Fig. 1.20. The Type 3 mechanism suggests that the oxygen present in the gas phase will not only affect the materials ability to establish a protective oxide layer at the surface, but also contribute to matrix destruction once metal dusting has been initiated.[44-46] Apparently, all three mechanisms can operate at the same time, but the alloy composition and exposure conditions will eventually determine which type of corrosion mechanism that will dominate in each case.[23]

1.5. References

1. J. Pattinson: *Journal of Iron Institute*, 1876, vol. 1, pp. 85-100.
2. M. Bohnet, Ed., *Ullmann's Encyclopedia of Industrial Chemistry*, vol. 22 (ed. 6, 2003), pp. 708.
3. R. Hansen, J. Sogge, M. H. Wesenberg, O. Olsvik, "*Selecting optimum syngas and process design for large scale conversion of natural gas into Fischer Tropsch products (GTL) and Methanol*", paper presented at The 6th Natural Gas Conversion Symposium, Girdwood, Alaska, USA, 17.-21. June 2001.
4. M. J. Donachie, S. J. Donachie: *Superalloys - A Technical Guide*, 2'nd ed., ASM International, Materials Park, Ohio, 2002.
5. T. B. Massalski: *Binary alloy phase diagrams*, 1'st ed., American Society for Metals, Metals Park, Ohio, 1986.
6. F. Tancret, H. K. D. H. Bhadeshia: *Materials Science and Technology*, 2003, No.3, vol. 19, pp. 291-295.
7. H. J. Grabke, H. P. Martinz, E. M. Müller-Lorenz: *Materials and Corrosion*, 2003, No.11, vol. 54, pp. 860-863.
8. B. A. Baker, V. W. Hartmann, L. E. Shoemaker, S. A. McCoy, S. Rajendran: *Transactions of the Indian Institute of Metals*, 2003, No.3, vol. 56, pp. 327-333.
9. J. Wilson, D. C. Agarwal, "*Case histories on successful applications of alloy 602CA, UNS N06025 in high temperature environments*", paper presented at Corrosion/2005, Houston, Texas, USA, 3.-7.April 2005, NACE International, Houston, Texas, USA.
10. B. A. Baker, G. D. Smith, S. A. McCoy: *Ammonia plant safety (and related facilities)*, 2002, vol.42, pp. 257-267.
11. D. C. Agarwal, U. Brill, "*Performance of alloy 602CA in high temperature environments up to 1200ºC (2200ºF)*", paper presented at Corrosion/2000, Orlando, Florida, USA, 26.-31.March 2000, NACE International, Houston, Texas, USA.
12. D. C. Agarwal, L. Stewart, M. McAllister, "*Alloy 602CA (UNSNO6025) solves pig tail corrosion problems in refineries*", paper presented at Corrosion/2003, San Diego, California, USA, 16-20 March 2003, NACE International, Houston, Texas, USA.
13. B. A. Baker, G. D. Smith, V. W. Hartmann, L. E. Shoemaker, S. A. McCoy, "*Nickel-base material solutions to metal dusting problems*", paper presented at Corrosion/2002, Denver, Colorado, USA, 7.-11.April 2002, NACE International, Houston, Texas, USA.

14. www.specialmetals.com/products: 2004.
15. www.thyssenkrupp.com: 2004.
16. F. Eberle, R. D. Wylie: *Corrosion*, 1959, No.12, vol. 15, pp. 622t-626t.
17. M. L. Holland, H. J. De Bruyn: *International Journal of Pressure Vessels and Piping*, 1996, No.1-3, vol. 66, pp. 125-133.
18. H. J. Grabke, M. Spiegel: *Materials and Corrosion*, 2003, No.10, vol. 54, pp. 799-804.
19. H. J. Grabke: *Materials and Corrosion*, 2003, No.10, vol. 54, pp. 736-746.
20. R. Yin: *Oxidation of metals*, 2003, No.1/2, vol. 60, pp. 103-116.
21. R. Yin: *Oxidation of metals*, 2004, No.3/4, vol. 61, pp. 323-337.
22. O. Kubaschewski, C. B. Alcock: *Metallurgical thermochemistry*, 5'th ed., Pergamon Press, Oxford, 1979.
23. P. Szakálos: "*Mechanisms of Metal Dusting*", PhD Thesis, KTH - Royal Institute of Technology, Department of Materials Science and Engineering, Stockholm, 2004.
24. P. Shewman: *Diffusion in solids*, 2'nd ed., The Minerals, Metals & Materials Society (TMS), Pennsylvania, USA, 1989.
25. J. Cranck: *The Mathematics of Diffusion*, 2'nd ed., Clarenden Press, Oxford, UK, 1975.
26. A. Engström: "*Long-range Diffusion and Microstructural Evolution in Multiphase Alloys - A Combined Thermodynamic and Kinetic Approach*", PhD Thesis, Royal Institute of Technology, Department of Materials Science and Engineering, Stockholm, 1996.
27. H. J. Grabke, E. M. Müller-Lorenz, B. Eltester, M. Lucas: *Materials at high temperatures*, 2000, No.2, vol. 17, pp. 339-345.
28. H. J. Grabke, E. M. Müller-Lorenz, "*Occurrence and prevention of metal dusting on stainless steels*", paper presented at Corrosion/2001, Houston, Texas, USA, 11.-16.March 2001, NACE International, Houston, Texas, USA.
29. R. F. Hochman, J. H. Burson: *American Petroleum Institute Division of Refining Proceedings*, 1966, vol.46, pp. 331-344.
30. R. F. Hochman, "*Metal Deterioration in Carbon Monoxide and Hydrocarbon at Elevated Temperatures*", paper presented at 3'rd International Congress on Metallic Corrosion, Moscow, Russia, 1966, University of Moscow Press.
31. H. J. Grabke, R. Krajak, J. C. Nava Paz: *Corrosion Science*, 1993, No.5-8, vol. 35, pp. 1141-1150.

32. H. J. Grabke: *Corrosion*, 1995, No.9, vol. 51, pp. 711-720.

33. J. C. Nava Paz, H. J. Grabke: *Oxidation of metals*, 1993, No.5-6, vol. 39, pp. 437-456.

34. E. Pippel, J. Woltersdorf, R. Schneider: *Materials and Corrosion*, 1998, No.5, vol. 49, pp. 309-316.

35. A. Schneider: *Corrosion Science*, 2002, No.10, vol. 44, pp. 2353-2365.

36. P. Szakálos: *Materials and Corrosion*, 2003, No.10, vol. 54, pp. 756-762.

37. J. Klöwer, H. J. Grabke, E. M. Müller-Lorenz, D. C. Agarwal, "*Metal dusting and carburization resistance of nickel-base alloys*", paper presented at Corrosion/97, New Orleans, LA, USA, 9.-14.March 1997, NACE International, Houston, Texas, USA.

38. C. Y. Lin, C. H. Chang, W. T. Tsai: *Oxidation of metals*, 2004, No.3/4, vol. 62, pp. 153-174.

39. H. J. Grabke, E. M. Müller-Lorenz, S. Strauss, E. Pippel, J. Woltersdorf: *Oxidation of metals*, 1998, No.3/4, vol. 50, pp. 241-254.

40. H. J. Grabke, R. Krajak, E. M. Müller-Lorenz, S. Strauss: *Materials and Corrosion*, 1996, 47, pp. 495-504.

41. R. Schneider, E. Pippel, J. Woltersdorf, S. Strauss, H. J. Grabke: *Steel research*, 1997, No.7, vol. 68, pp. 326-332.

42. C. M. Chun, T. A. Ramanarayanan, J. D. Mumford: *Materials and Corrosion*, 1999, vol. 50, pp. 634-639.

43. E. Pippel, J. Woltersdorf, H. J. Grabke: *Materials and Corrosion*, 2003, No.10, vol. 54, pp. 747-751.

44. B. Schmid, Ø. Grong, R. Ødegård: *Materials and Corrosion*, 1999, No.11, vol. 50, pp. 647-653.

45. H. J. De Bruyn, E. H. Edwin, S. Brendryen, "*Apparent influence of steam on metal dusting*", paper presented at Corrosion/2001, Houston, Texas, USA, 11.-16.March 2001, NACE International, Houston, Texas, USA.

46. M. Hänsel, C. A. Boddington, D. J. Young: *Corrosion Science*, 2003, vol.45, pp. 967-981.

PART II

Scope and experimental approach

2.1. Research strategy

To further increase the understanding of the metal dusting corrosion phenomenon, it is necessary to develop a research strategy that fully acknowledges the complexity of the problem. Such a strategy should also aim at developing procedures for qualifying materials for specific intended applications in a syngas unit. Specifically, it should cover the following aspects:[1]

1) Exposing relevant materials to realistic process environments for sufficiently long time to produce materials specimens that can be used for further study.
2) Establishing and developing a fundamental understanding of metal dusting, based on thermodynamics, kinetics and catalysis.
3) Employing optimum examination tools to study alloy microstructures and metal dusting damage.

These three aspects of the research strategy are illustrated in Figure 2.1.

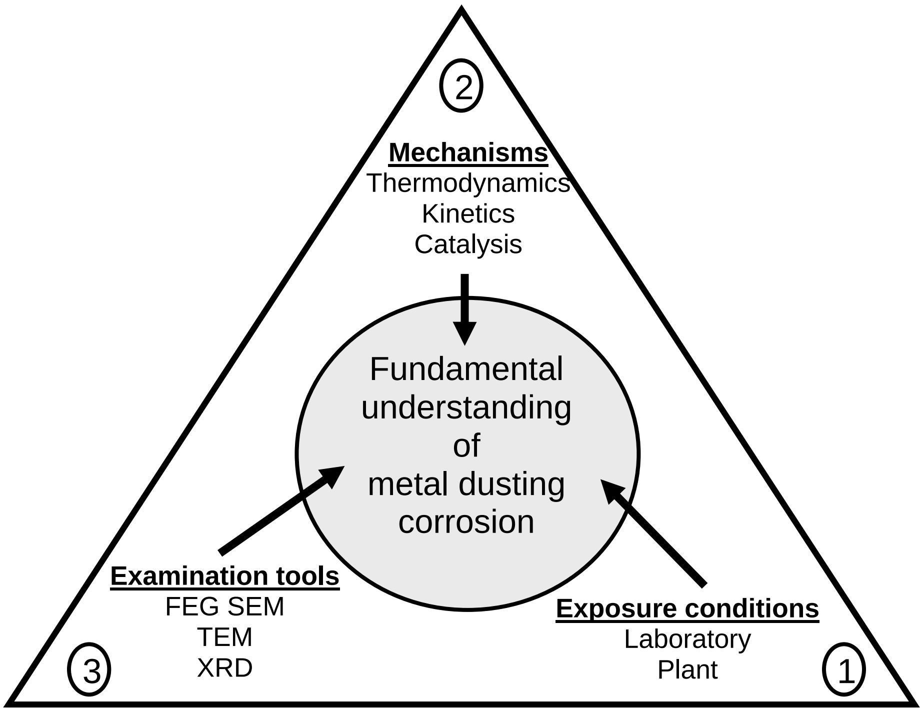
2
Mechanisms
Thermodynamics
Kinetics
Catalysis
Fundamental understanding of metal dusting corrosion
Examination tools
FEG SEM
TEM
XRD
3
Exposure conditions
Laboratory
Plant
1

Figure 2.1 Proposed metal dusting research strategy. The diagram is based on the ideas of De Bruyn *et* al.[1]

2.1.1. Exposure conditions

The exposure of different alloys should occur under realistic process conditions, taking into account all reasons for failure. Exposures should also be long enough to produce reliable data. It is very important not to assume that some parameters, like contaminants for example, are not important. There is still, today, an inadequate understanding of metal dusting thermodynamics, where all participating reactions are included as well as the kinetics of these. Making assumptions on how the gas aggressiveness can be increased to produce results in shorter times are likely to change several other important parameters, and should not be attempted without a thorough understanding of all the relevant reactions that might occur during the damage process.

2.1.2. Mechanisms

A fundamental understanding of metal dusting should preferably be developed through understanding of the gas/metal reactions involved, the thermodynamic driving forces for these reactions as well as the kinetics of the most relevant reactions. In addition, the catalytic influence that an alloy surface has on the metal dusting reactions must be incorporated in the analysis. Physical metallurgy should be employed to understand changes that occur in the alloy during exposure. Metal dusting literature, especially those dealing with mechanisms, should not be merely accepted without thoroughly questioning all reasoning behind the statements.

2.1.3. Examination tools

Metallographic examinations are vital tools in the study of metal dusting. Light microscopy should be complemented with more advanced electron microscopy. Metal dusting is a damage process that occurs on a nano-scale. The tools to study this should be able to resolve images on the same scale. Conventional scanning electron microscopy (SEM) has limitations that could be vastly improved with the use of a field emission gun scanning electron microscope (FEG SEM).[2] Ultimately, the study of finely dispersed carbides may require the use of a transmission electron microscope (TEM).[3] Element and phase identification are equally important in the study of metal dusting. The use of energy dispersive X-ray analysis (EDS), often fitted to scanning electron microscopes, is commonly used in metal dusting studies for the identification of different elements. However, these tools are rarely calibrated to provide full quantitative analysis and lack the ability to determine phase compositions accurately, besides, exact identification of light elements (i.e. carbon) can be difficult due to contamination. Both Raman spectroscopy[4] and X-ray diffraction[2, 4, 5] have been successfully used to identify phases and to study modifications due to carbon penetration. The availability to use these techniques during metal dusting studies significantly improves the quality of the results and the fundamental understanding of metal dusting corrosion.

2.1.4. Concluding remarks

In the present thesis, attempts will be made to implement this research strategy. Obviously, this is a formidable task that cannot be undertaken by a single person, but must be done in collaboration with competent researchers covering the relevant fields. Although the challenges are great, it is hoped that the strategy will help developing our understanding of the metal dusting phenomenon a step further and at the same time provide the required stimulus for new research work. This, in turn, can lead to improved scientific understanding of one of the classical problems of materials technology in the context of high temperature corrosion.

2.2. Experimental

The present investigation is part of a larger research programme on metal dusting corrosion in various nickel-, iron- and cobalt-based alloys during long time exposure (2 and 4 years) to syngas in an industrial plant for methanol production. Included in the investigation are two Ni-based alloys and one Fe-based alloy, the latter serving as a reference material to clarify the origin of the observed Ni-deposit on the surface of the exposed alloys.[6]

2.2.1. Materials

Samples of the two nickel-based alloys and the iron-based alloy were obtained from different commercial material manufacturers. Their chemical compositions are given in Table 2.1. The nickel-based alloy 693 and the iron-based alloy APMT were at the time of investigation classified as test materials still under development, whereas alloy 602 is a well-proven Ni-based alloy specially designed for high-temperature applications.

Table 2.1 Chemical composition of the three alloys 602 and 693 and APMT, in wt%.

Alloy	Ni	Fe	Cr	Al	Si	Ti	Mn	Co	Zr	Nb	W	Y	C
602	62.5	9.5	25.1	2.2	0.1	0.1	0.1	-	0.1	-	-	0.1	0.2
693	58.6	6.0	29.7	3.3	0.1	0.1	-	1.7	-	0.6	-	-	-
APMT	0.2	73.0	21.0	5.8	0.3	-	0.2	-	-	-	0.2	-	-

In both nickel-based alloys, nickel is the main constituent element. The matrixes are fully austenitic and contain the hardening γ' - $Ni_3(Al,Ti)$ precipitate phase.[7] In addition, alloy 602 contains a secondary $M_{23}C_6$ carbide phase distributed as micrometer-sized globular particles at grain boundaries and in the bulk. Its presence is reflected in the carbon analysis. Moreover, both materials are alloyed with Cr (major) and Al (minor), which generally improve their resistance to surface degradation due to carburisation and oxidation. Other elements such as Nb, Co, Zr, and Y are also added to obtain the desired microstructure and properties at elevated temperatures.[8, 9] Alloy 693 and APMT were tested in the as-received condition, while the cold rolled and solution annealed alloy 602 was used in the surface pickled condition. Pickling is a chemical treatment which removes scale and contaminants from the surface to assist formation of a continuous chromium oxide layer.

In contrast to the 602 and 693 alloys, which are produced using the conventional melting and casting techniques, the iron-based ferritic material, APMT, is a powder metallurgy based material. In this case rapid solidification is employed to achieve a dispersion strengthened matrix.[10] The material contains a fine dispersion of stable inclusions which provide obstacles to grain growth and dislocation movement. In addition, balanced alloying with chromium and aluminium results in a material that exhibits a high intrinsic resistance against oxidation.[10] Because the APMT material contains no nickel, it is an excellent test material for comparison with the two nickel-based alloys 602 and 693 under conditions where metal dusting corrosion occurs.

2.2.2. Exposure conditions

Samples were welded onto a valve in an industrial plant for methanol production, close to the waste heat boiler outlet, in an environment which is known to promote metal dusting corrosion during service. Samples of the alloys were kept inside the waste heat boiler for 2 and 4 years before they were removed during a pre-scheduled plant shut down. During operational exposure, the total pressure was 35 bar (3.5MPa) and the gas temperature was approximately 540˚C. The approximate bulk gas composition in vol % is shown in Table 2.2.

Note that the process gas, like most industrial syngas mixtures, contains traces of Na, Si and Ni at the stage where it enters the waste heat boiler.

Table 2.2 Inlet process gas composition, in vol%.

Gas component	CO	H_2	H_2O	CO_2	CH_4	Trace elements
Content (vol%)	15	47	31	6	1	Ni, Na, Si

In addition to the industrial exposure, steam oxidation laboratory experiments were conducted in a 2 liter high pressure autoclave (UNS N10276) at 540˚C and 30 bar (3.0MPa) to study instantaneous oxide formation in alloy 602. The target gas mixture of 50 vol% H_2O and 50 vol% N_2 was obtained by preheating the carrier gas to 250°C before water injection, employing a conventional gas blending system. This wet gas mixture was further preheated to 450°C before it was led into the hot pressurised autoclave. Prior to exposure, the samples were ground using grade 150 SiC emery paper and rinsed in methanol. The samples were then kept in the steam environment inside the autoclave for 75 hours, using a quartz glass sample holder supported on platinum wires.

Table 2.3 gives an overview of the alloys and the different exposure conditions being used throughout the thesis. Specifically, Part III deals with alloy 602, both unexposed and 2 years plant exposed samples. In Part IV the main focus is on the two years plant exposed alloys 602 and 693, where the iron-based APMT alloy is used as a reference material to clarify the origin of the observed Ni-deposit on the surface of the alloys following plant exposure.[6] Finally, Part V is concerned with the 4 years plant exposed alloys 602 and 693 and the mechanisms of metal dusting corrosion in these materials.

Table 2.3 Overview of the alloys and the different exposure conditions being used throughout the thesis.

Alloy	Exposure condition	Part of thesis		
		III	IV	V
602	Unexposed	X	X	
	Steam oxidised		X	
	2 years exposure	X	X	
	4 years exposure			X
693	Unexposed		X	
	2 years exposure		X	
	4 years exposure			X
APMT	2 years exposed		X	
	4 years exposed		X	

2.2.3. Experimental techniques

In accordance with the proposed research strategy, the alloys were examined using different experimental techniques. These include light microscopy, hardness measurements, scanning electron microscopy, microprobe analyses, transmission electron microscopy and synchrotron X-ray diffraction (S-XRD). Table 2.4 gives an overview of the different experimental techniques being employed throughout the thesis.

Table 2.4 Overview of the different experimental techniques being used throughout the thesis.

Experimental technique	Part III	Part IV	Part V
Light optical microscopy	X	X	X
Hardness measurements	X	X	-
FEG SEM	X	X	X
Microprobe/WDS analyses	-	-	X
TEM	-	X	X
S-XRD	X	X	X

2.2.3.1. Optical microscopy and hardness measurements

Standard metallographic techniques were employed to prepare the cross section samples used in the optical microstructure characterisation. Following cleaning in ethanol, microstructures were revealed by electrolytical etching in 5% H_2SO_4 at 3V for approximately 10 seconds and also by Bloech & Wedl colour etching. The Bloech & Wedl etchant consists of 0.1 to 2g of potassium metabisulphite in a 100 ml stock solution (i.e. 5 parts distilled water and 1 part concentrated hydrochloric acid, by volume). Metallographic examination was performed in a conventional Zeiss reflecting light microscope on both unexposed, steam oxidised and plant exposed samples of the alloys.

In addition, Vickers hardness measurements were carried out in cross section geometry to evaluate the metallurgical stability of the alloys following different exposure conditions. The hardness indentations were performed on polished samples using a Wolpert hardness tester and a load of 1kg. A total of 6 independent hardness measurements were performed at each location at varying depths below the surface to obtain the desired hardness profiles, which are constructed on the basis of the average (mean) values.

2.2.3.2. Scanning electron microscopy

The plant exposed samples were investigated at high magnification in the as-polished condition using a Field Emission Gun Scanning Electron Microscope (FEG SEM), type Hitachi S-4300SE, equipped with an Oxford INCA Energy EDS system. Reaction products and particles at the surface were examined by backscattered electrons (BSE) to reveal variations in chemical composition, and secondary electrons (SE) to reveal topographic details on the surface. EDS composition analyses and X-ray mapping in the cross section geometry were carried out in the surface-near regions and close to metal dusting corrosion pits to determine the element distribution within specific phases.

2.2.3.3. Microprobe analyses

An electron probe micro analyser, or microprobe, is basically a scanning electron microscope designed and optimised for X-ray analysis of elements from very small areas. The distribution of the main constituent elements; nickel, chromium, iron and aluminium, along with carbon and oxygen within the surface near regions of the alloys was investigated applying a JEOL JXA-8900 microprobe analyser. The instrument is equipped with 4 wavelength dispersive X-ray spectrometers (WDS) in addition to an energy dispersive X-ray spectrometer (EDS). Compared to conventional EDS analyses, the WDS technique is particularly useful for light element detection in the presence of chromium. This is because the problem with overlap between the $K\alpha$ radiation energy of oxygen (0.526keV) and the $L\alpha$ radiation energy of chromium (0.573keV) in the X-ray spectrum then is avoided.

The WDS measurements were done employing an accelerating voltage of 15kV and a pre-selected step size of 1µm. Several line scans were performed across the surface area of the alloys, starting from the bottom of the pits and continuing approximately 100µm into the bulk of the materials. The dotted lines in Figure 2.2 indicate the position of the linescans.

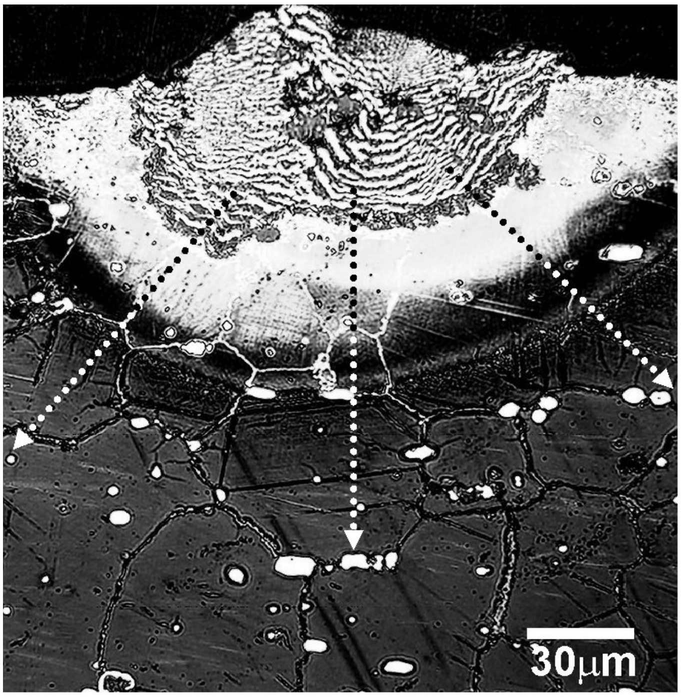

Figure 2.2 The dotted lines indicate the position of line scans performed on alloy 602, starting from the bottom of the pits and continuing approximately 100μm into the bulk alloy.

2.2.3.4. Transmission electron microscopy

Subsequent STEM/TEM analyses were performed in a JEOL 2010F microscope operating at 200kV. Both compositional analyses and X-ray mapping were carried out in the surface near region of the sample employing an Oxford Instruments INCA energy dispersive spectroscopy (EDS) system.

Cross section samples were prepared for examination in a transmission electron microscope (TEM). The thin foils from the steam oxidised sample of alloy 602 were prepared by gluing 3mm thick slices of exposed surfaces face to face, from which 0.2mm thick orthogonal slices were cut. These were further ground to a thickness of ~0.12mm and then dimple ground to a central thickness of ~0.03mm before ion thinning from both sides to achieve the required electron transparency.

TEM samples of the plant exposed alloys were prepared applying a Focused Ion Beam (FIB) instrument, which is a rapid and precise specimen preparation method for TEM.[11] The FIB samples (10μm x 10μm x 0.1μm) were removed from selected positions using a single beam

Hitachi FIB2100 instrument. These were taken from the uncorroded parts of the surface as well as from the bottom of metal dusting corrosion pits, as shown schematically in Figure 2.3.

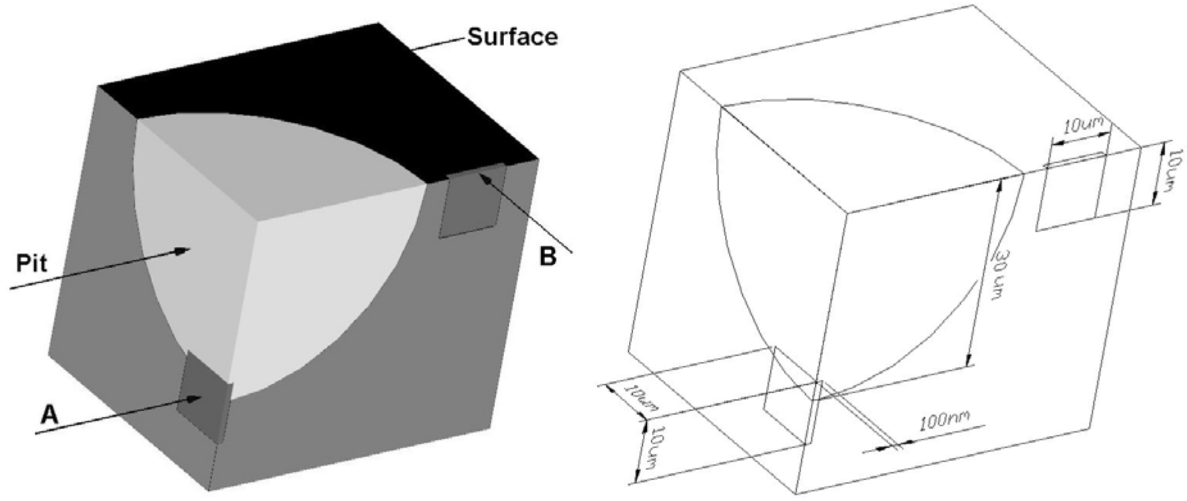

Figure 2.3 Schematic diagrams showing the areas from which the FIB samples were extracted. Section (A) referring to the bottom of the metal dusting corrosion pits, and Section (B) referring to the uncorroded parts of the surface.

Complementary diffraction analyses were then performed to determine lattice parameters and crystal structure of specific phases. These were compared to simulated diffraction patterns obtained by applying the MaC TempasX Software - Version 2.1.1.[12], which is a program for simulating diffraction patterns. Input data, such as applied camera length, acceleration voltage as well as type of structure, space group and lattice constants give diffraction patterns which can be viewed from different zone axes.

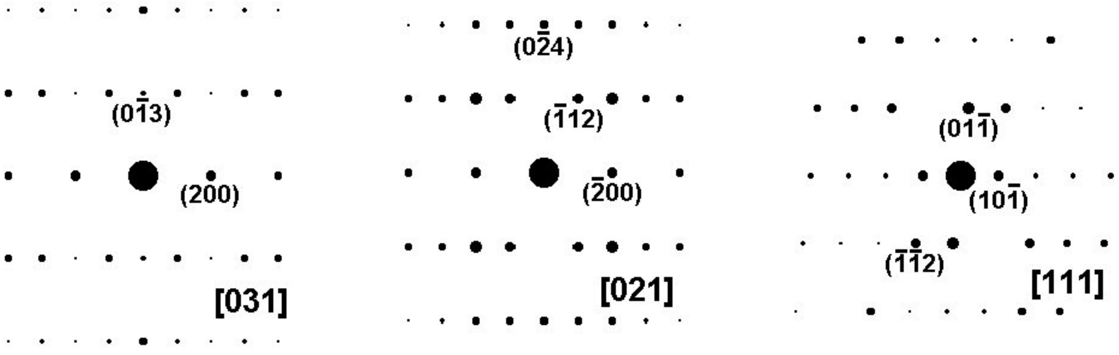

(a) (b) (c)

Figure 2.4 Simulated diffraction patterns of the Cr_3C_2 carbide from different zone axes; (a) The [031] zone axis, (b) The [021] zone axis and (c) The [111] zone axis. The simulations are done using the Mac Tempas X Software – Version 2.1.1.[12]

Examples of simulated diffraction patterns from the orthogonal Cr_3C_2 carbide with Pnma space group, lattice constants; a = 5.5329Å, b = 2.8290Å and c = 11.4719Å, are shown in Figure 2.4. These refer to specific zone axes. Note that double diffraction will occur and cause the forbidden reflections to appear in the real diffraction pattern if the thickness of the thin foil is too large.

2.2.3.5. Synchrotron X-ray diffraction

X-ray diffraction (XRD) is a powerful tool for identification and quantification of crystalline phases in multiphase samples and is extensively used as a tool for materials characterisation. The main difference between X-ray and electron diffraction is that electron-material interactions are typically 3 orders of magnitude stronger than their photon-material counterparts. Therefore, electron transmission is much lower than X-ray transmission. Accordingly, X-ray samples do not require special preparation. On the other hand, since X-ray interaction is much weaker, generally larger crystalline domains are needed to produce detectable diffraction signals. Therefore, X-ray diffraction signals are difficult to detect from microstructure phases with grainsizes below ~30 nm (slightly dependent on wavelength and atomic composition). It is therefore possible that the characterised samples contain nanometer sized corrosion product particles or bulk precipitates unaccounted for in the study. In the geometry chosen for the experiment, the sample surface was more or less completely bathed with the incident beam which combined with the typical penetration depth resulted in probed sample volumes of the order of several mm^3. Accordingly the experiment output provides a global overview of the mean surface near microstructure of the sample, where products constituting less than typically 0.1 to 0.2 % of the activated scattering volume are difficult to detect, even of their local concentrations are considerable.

Synchrotron XRD is mainly distinguished from classical source XRD by two important aspects. Firstly, a typical synchrotron bending magnet (BM) source at the European Synchrotron Radiation facility (ESRF) offers a continuous and useable photon energy spectrum from 4 to 60 keV, which allow the experimentalist to select an optimum energy for the experiment by monochromatisation of the continuous source. With a classical source, standard XRD experiments are usually restricted to occur at energies corresponding to the characteristic emission lines of the anode target material. Secondly, synchrotron BM sources exceed the classical sources by a factor of 10^{10}, or even more in brilliance, i.e. the intensity at the sample position per unit cross section. Accordingly, for synchrotron setups it is affordable in terms of measurement time and efficiency to employ excessive pre- and post sample filtering, such as slitting, monochromatization and angular apertures with low acceptance in the diffracted beams. For these reasons S-XRD superceeds XRD with conventional sources in terms of angular resolution, discrimination of secondary emission (fluorescence) and adjustability in parameters like sample penetration.

The Synchrotron XRD experiments were done employing a high resolution powder diffractometer at the Swiss-Norwegian Beam Line (SNBL); D01B, at the ESRF in Grenoble, France.[13] The diffractometer is equipped with a three-axis goniostat for sample spinning (φ) and geometry alignment (χ, ω), and a six-channel point detector array with Si_{111} analyser crystals allowing for parallel measurements of six high resolution diffractograms. The analyser crystals limits the angular acceptance of the detector which at the energies used for the experiments corresponds to roughly 0.02mrad. The experimental set-up is shown in Figure 2.5.

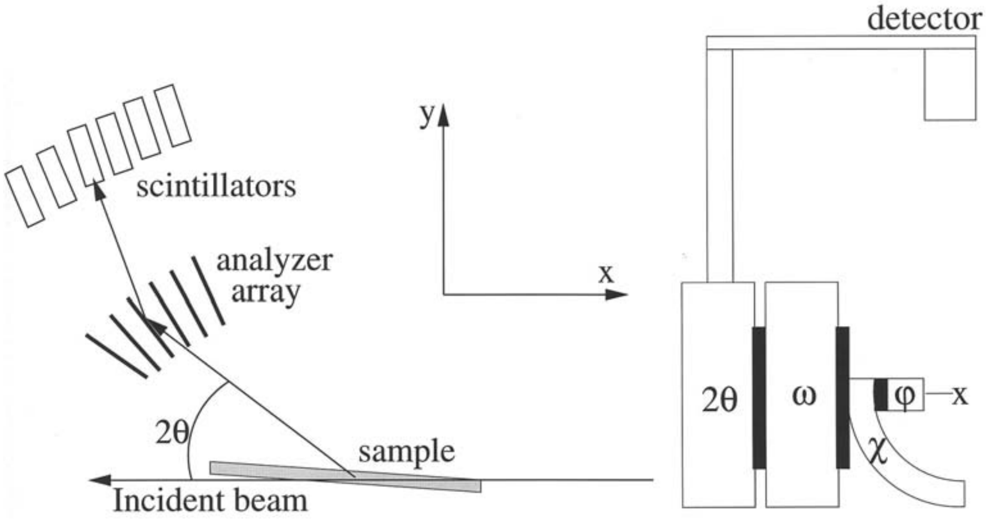

Figure 2.5 The SNBL 1B three-axis goniostat (right), and a sketch showing the flat sample reflection geometry and the 6 channel analyser/scintillator array (left).

The S-XRD experiments were carried out in reflection geometry using incident monochromatic beam energy of E = 17.7keV. Diffractograms were collected at T = 297 K over the pertinent 2θ-ranges, employing fixed angular step sizes, Δ2θ, and a constant counting time of 1s per step, which resulted in an average measuring time of approximately 2.5 hrs per sample. Moreover, sample spinning was chosen to minimise the effects caused by possible sample inhomogeneties and local surface topography. By optimising the sample inclination angle *ω* in each experiment, the X-ray penetration depth could be controlled, resulting in enhanced output signals from the surface near regions and improved counting statistics for a given combination of alloy composition, exposure condition and surface topography. Variations of ω between 2° and 6.5° were used to achieve the desirable penetration employing a model for the X-ray absorption based on homogeneous sample compositions and lattices corresponding to the as-delivered materials. With these models, the ω-adjustments corresponded to 99% output signal cut-off at effective bulk penetration depths of 5 to 11μm, schematically indicated by the dashed horisontal line in the FEG SEM cross section image in Figure 2.6.

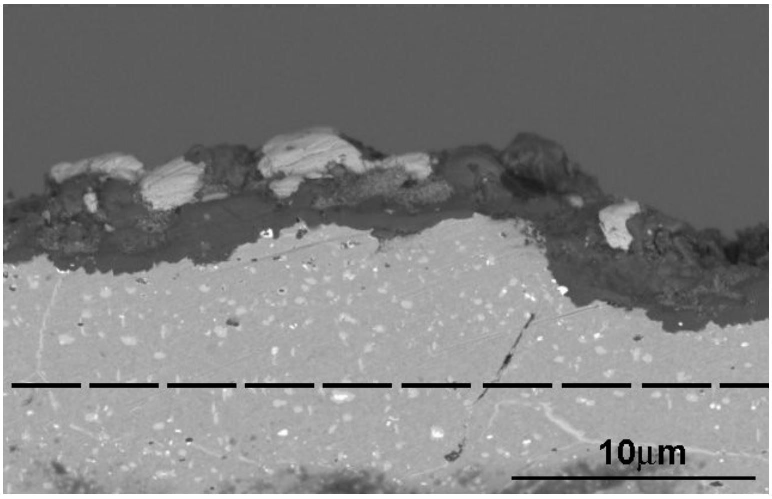

Figure 2.6 FEG SEM cross section image of the 4 years plant exposed alloy APMT. The dashed horisontal line indicates the maximum penetration depth from which the S-XRD signals have been extracted.

The experimental parameters used in the synchrotron X-ray diffraction analyses are summarised in Table 2.5.

The subsequent processing of the experimental X-ray diffraction data was carried out using the General Structure Analysis System (GSAS) software.[14] For each phase least squares refinements involved lattice parameters, relative scale factors in addition to a set of intensity profile parameters fitted by employing a multi-term Simpson's rule integration approach[15] to a pseudo-Voigt model.[16] Based on the assumption that the constituent phases are distributed homogeneously in the probed sample volume, the relative scale factors could be interpreted as estimates for the phase specific volume fractions. However, this assumption is not justified here, and more accurate volume fraction estimates would require the use of sophisticated models correcting for X-ray absorption. Because such corrections are rather complicated to implement, and generally would be associated with potentially large errors, attempts have not been made towards an absolute quantification of the phase fractions in the present investigations. Still, the scale factors represent the relative fractions of the phases detected, and will thus be useful to identify and point out various global differences and similarities encountered for the different samples and exposure conditions.

Table 2.5 Summary of experimental parameters used in the S-XRD analyses.

Alloy	Condition	ω [°]	2θ-range [°]	Δ2θ [°]	# of scans
602	Unexposed	6	4.5-55	0.005	1x6
	Steam oxidised	3	4-45	0.005	1x6
	2 years syngas	6	4-45	0.005	1x6
	4 years syngas	5	3-50	0.003	5x6
693	Unexposed	3	10-45	0.005	1x6
	Steam oxidised	2	5-40	0.005	1x6
	2 years syngas	5	4-40	0.005	2x6
	4 years syngas	6.5	3-40	0.003	3x6
APMT	2 years syngas	2	3.5-65	0.005	1x6
	4 years syngas	5	3-50	0.003	5x6

2.3. References

1. H. J. De Bruyn, B. Schmid, Ø. Grong, J. Z. Albertsen, "*Adapting metal dusting research to trends in syngas technology*", paper presented at Corrosion/2005, Houston, Texas, USA, 3.-7.April 2005, NACE International, Houston, Texas, USA.
2. J. Z. Albertsen: Part III, IV and V of the present thesis.
3. B. Schmid: "*Microscale examination of metal dusting corrosion in steels and in-situ observations of high temperature oxidation of metals*", PhD Thesis, NTNU - Norwegian University of Science and Technology, Department of Materials Technology and Electrochemistry, Trondheim, 2000.
4. Z. Zeng, K. Natesan, V. A. Maroni: *Oxidation of metals*, 2002, No.1-2, vol. 58, pp. 147-170.
5. J. Z. Albertsen, Ø. Grong, R. H. Mathiesen, B. Schmid: *Corrosion Engineering, Science and Technology*, 2005, No.3, vol. 40, pp. 239-243.
6. J. Z. Albertsen: Part IV of the present thesis.
7. M. J. Donachie, S. J. Donachie: *Superalloys - A Technical Guide*, 2'nd ed., ASM International, Materials Park, Ohio, 2002.
8. J. Wilson, D. C. Agarwal, "*Case histories on successful applications of alloy 602CA, UNS N06025 in high temperature environments*", paper presented at Corrosion/2005, Houston, Texas, USA, 3.-7.April 2005, NACE International, Houston, Texas, USA.
9. B. A. Baker, G. D. Smith, V. W. Hartmann, L. E. Shoemaker, S. A. McCoy, "*Nickel-base material solutions to metal dusting problems*", paper presented at Corrosion/2002, Denver, Colorado, USA, 7.-11.April 2002, NACE International, Houston, Texas, USA.
10. B. Jonsson, R. Berglund, J. Magnusson, P. Henning, M. Hattestrand: *Materials Science Forum*, 2004, 461-464, pp. 455-462.
11. L. A. Giannuzzi, F. A. Stevie: *Micron*, 1999, No.3, vol. 30, pp. 197-204.
12. R. Kilaas: MacTempas, A Program for Simulating High Resolution TEM images and Diffraction patterns, Version 2.1.1, Berkeley Total Resolution Ltd., Berkeley, CA, 1992.
13. ESRF: www.esrf.fr/exp_facilities/BM1A/index.htm, 2005.
14. A. C. Larson, R. B. Von Dreele: GSAS, General Structure Analysis System, LANSCE, S-H805, Los Alamos National Laboratory, Los Alamos, 2000.
15. C. J. Howard: *Journal of applied crystallography*, 1982, vol.15, pp. 615-620.

16. P. Thompson, D. E. Cox, J. B. Hastings: *Journal of applied crystallography*, 1987, vol.20, pp. 79-83.

PART III

Metallurgical investigation of metal dusting corrosion in plant exposed alloy 602

3.1. Introduction

Reforming of natural gas to syngas (CO + H_2) is perhaps the most crucial process step in the gas-to-liquid (GTL) conversion processes, e.g. methanol or Fischer-Tropsch synthesis. Despite the fact that nickel-based alloys are often used in critical parts of the plant, metal dusting corrosion still imposes limitations on engineering design.[1, 2] Research is currently being directed towards the development of new and more resistant alloys, and in particular balanced alloying with chromium and aluminium is claimed to improve the resistance to metal dusting corrosion under strongly reducing conditions.[3-5]

Although aspects of metal dusting corrosion have been extensively investigated and reported in the scientific literature, the mechanisms involved are not yet fully understood. Obviously, the exposed materials will be prone to carburisation and carbide formation owing to a characteristically high carbon activity in the gas phase, and carbide formation is normally considered to be a prerequisite for metal dusting corrosion.[6] However, more recently, the importance of surface oxide formation has been highlighted,[7-9] suggesting that metal dusting corrosion of nickel-based alloys occurs as a result of coupled carburisation and oxidation reactions.

In the present investigation, the nickel-based alloy 602 has been examined with respect to phase stability and metal dusting corrosion after 2 years of exposure in the reforming section of a methanol plant. Both field emission gun scanning electron microscope (FEG SEM) and synchrotron X-ray diffraction (S-XRD) analyses have been carried out in order to identify the constituent phases at the corroded surface. The combination of these two techniques has, in turn, lead to the identification of some new phases not commonly observed in connection with metal dusting corrosion.

3.2. Experimental

Part III deals specifically with alloy 602, both unexposed and 2 years plant exposed samples. The experimental techniques being used include:

- Light microscopy
- Hardness measurements
- Scanning electron microscopy (FEG SEM)

- Synchrotron X-ray diffraction (S-XRD) analyses

Further details are given in Part II of the thesis.

3.3. Results and Discussion

3.3.1. Microstructure near the alloy surface

The formation of carbides near the alloy surface was studied in order to judge the resistance of the alloy towards carbon intrusion. Figure 3.1 shows an optical image of the microstructure after plant exposure. The high chromium and carbon contents of the 602 alloy contributed to the formation of large $M_{23}C_6$ carbides in the material, both intragranularly and along grain boundaries. These carbides were also present in a similar manner in the unexposed parent material.

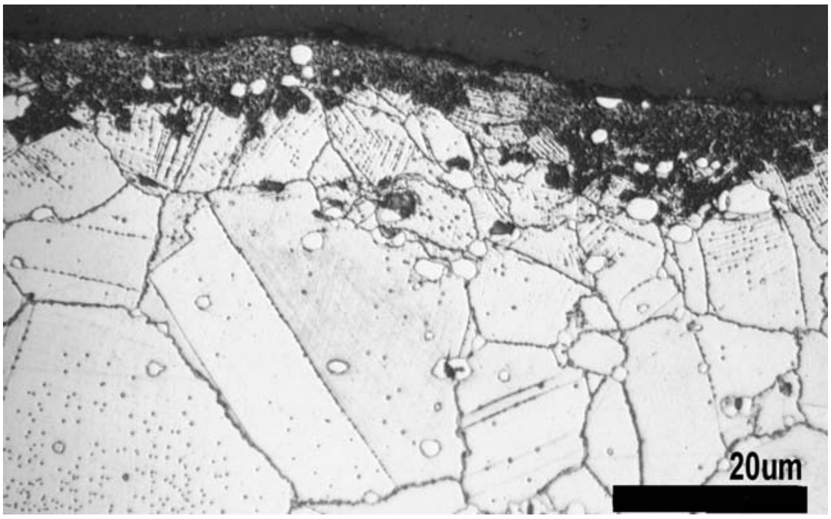

Figure 3.1 Optical image of plant exposed alloy 602 showing internal grain structure, chromium carbide formation and carburised zone beneath corroded surface.

The FEG SEM analyses of the corroded surface, using backscattered electron imaging, showed that the visible Cr-rich precipitation zone is approximately 20µm deep (Fig. 3.2). This zone corresponds to the darkly etched region in Fig. 3.1. Therefore, the surface oxide layer is not sufficiently dense to prevent reactions between the alloy and the surrounding syngas atmosphere. Some metal dusting corrosion pits are also present beneath the surface of the exposed alloy.[10] In other respects alloy 602 exhibits a high intrinsic resistance to metal dusting corrosion under the prevailing circumstances. In fact, after 2 years of exposure, the measured uniform material loss is negligible.

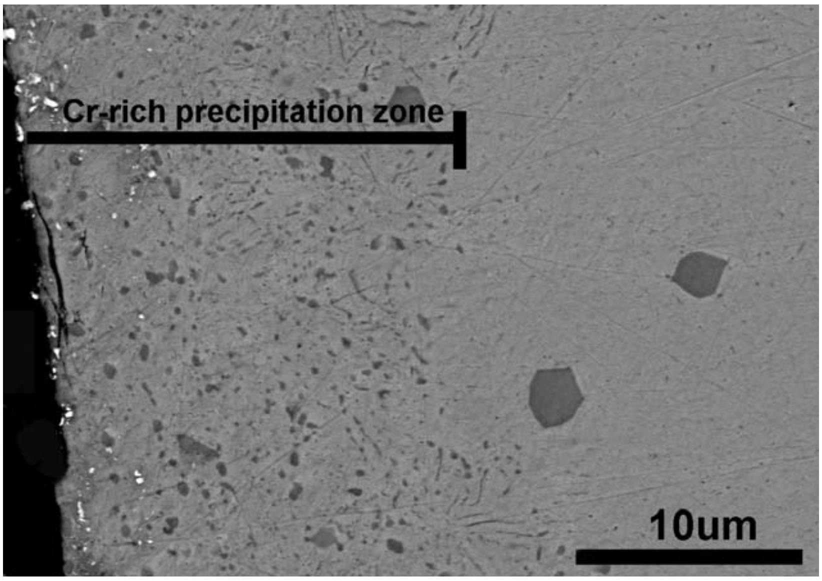

Figure 3.2 Backscattered electron image of cross-section of exposed alloy 602, indicating the width of visible Cr-rich precipitation zone.

3.3.2. Changes in hardness after prolonged high temperature exposure

Hardness measurements in a plane perpendicular to the surface were carried out to reveal changes in the microstructure. Figure 3.3 shows plots of the hardness profile in the cross-section of exposed and unexposed samples.

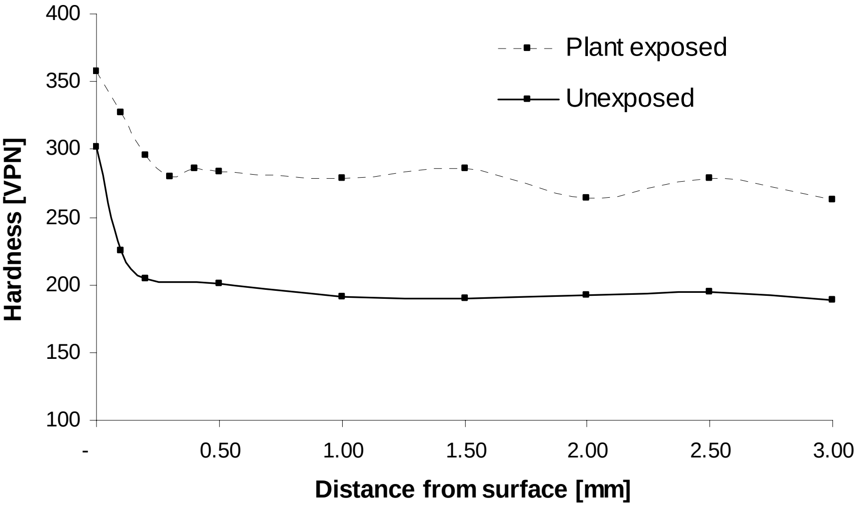

Figure 3.3 Plots of measured hardness profile in the cross-section of the plant exposed and unexposed alloy 602.

It is evident that alloy 602 is prone to secondary precipitation hardening at 540˚C, leading to a general increase in the bulk hardness of about 75 HV after 2 years of exposure. In other respects, the two hardness profiles are very similar. For example, the surface deformation zone is clearly visible in both samples, and extends about 0.25 mm into the bulk of the materials. This implies that neither recovery nor recrystallisation of the predeformed metal surface occurs during exposure. Therefore, the 602 alloy is essentially stable at 540˚C from a microstructural point of view, suggesting that mechanical degradation of the parent material is not a problem in the exposure environment.

3.3.3. X-ray mapping in FEG SEM

The constituent elements close to the corroded surface were identified by means of X-ray mapping in the FEG SEM. Figure 3.4 shows a backscattered electron image of the cross-section of the plant exposed alloy 602, along with X-ray maps of the main constituent elements. The maximum depth being viewed is about 3μm, referring to the surface of the sample. A closer inspection of Fig. 3.4 reveals that a crack is present approximately 1.5μm beneath the corroded surface. This crack is associated with Cr-Al oxide formation, and has probably developed as a result of this. At the corroded surface, Si and Na substitute for Cr as metallic components in the oxide phase. This suggests that an exchange reaction occurs between the elements when the Cr-Al oxide is exposed to process gas containing traces of Na and SiO(g).

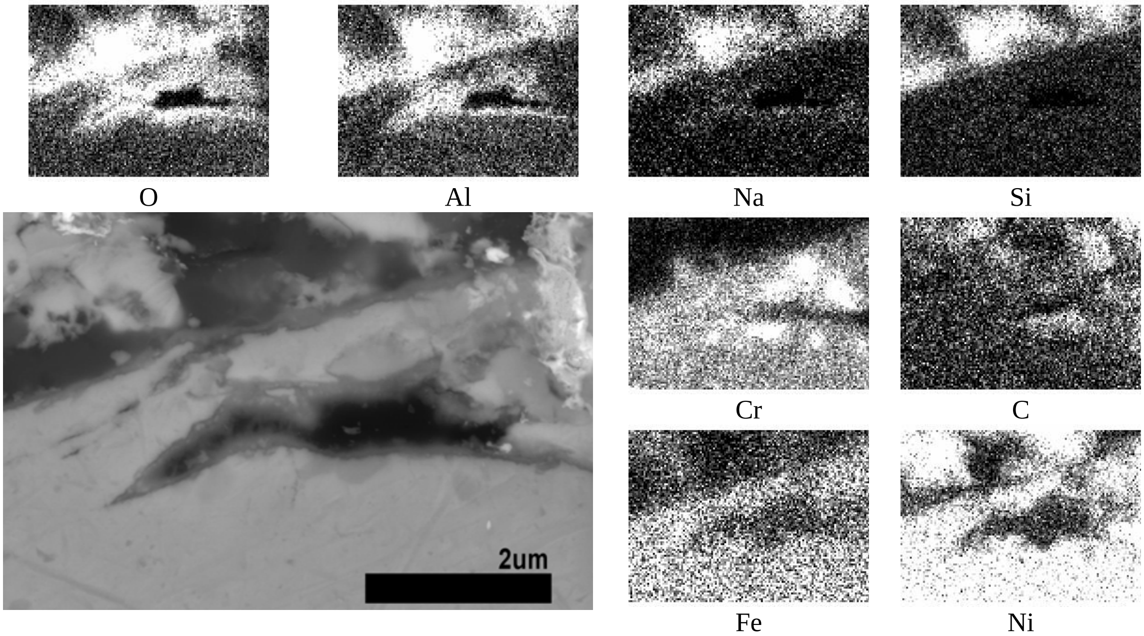

Figure 3.4 Backscattered electron image of cross-section of plant exposed alloy 602 along with X-ray maps of main constituent elements.

3.3.4. Identification of constituent phases close to the corroded surface

Six distinct phases were identified near and at the alloy surface using surface-sensitive synchrotron X-ray diffraction techniques. Figure 3.5 shows the results of the X-ray diffraction data analysis and refinements carried out using the general structure analysis system software (GSAS).[11]

Table 3.1 summarises the different phases that have been detected by means of the S-XRD analyses of both unexposed (U) and plant exposed (E) samples of the 602 alloy. The signals were extracted from a maximum depth of 11.5μm below and outwards from the surface.

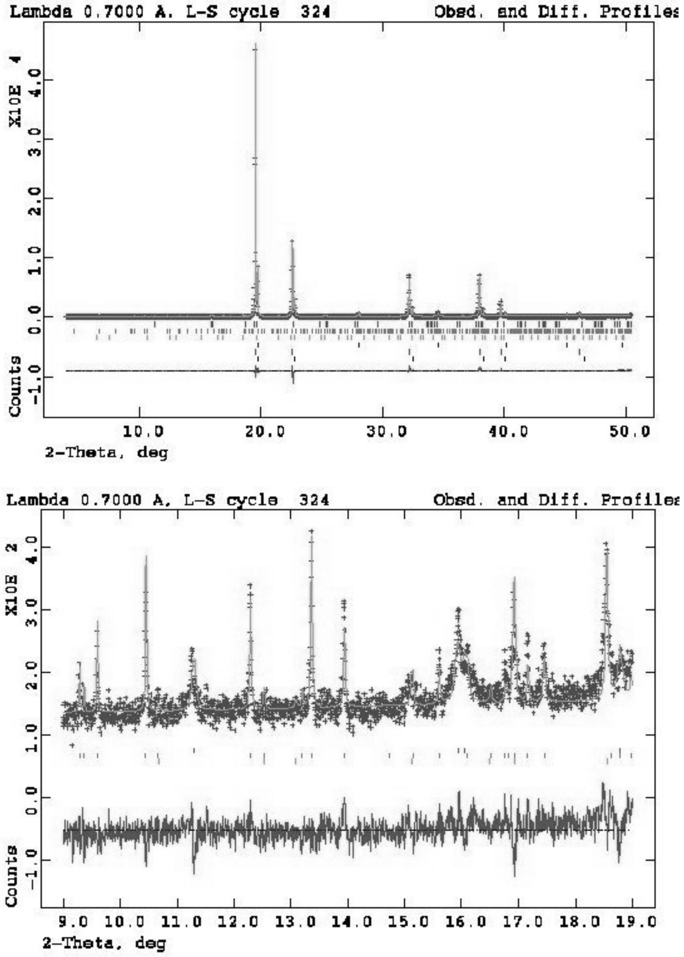

Figure 3.5 GSAS LSQ-fit plots of plant exposed alloy 602.

Table 3.1 Phases detected close to surface of unexposed (U) and plant exposed (E) samples of alloy 602 using S-XRD analyses. X-ray signals extracted from a depth down to 11.5μm below the surface. Numbers in parenthesis indicate standard deviation of experiments.

	Unexposed (U)	Plant exposed (E)
Aus_1, fcc *(Ni,Cr,Fe)*	*a* = 3.5851(1)Å 99.8 vol%	*a* = 3.5684(1)Å 83.0 vol%
Ni-deposit, fcc (γ-Ni)		*a* = 3.5395(1)Å 6.2 vol%
Ferrite, bcc (α-Cr)		*a* = 2.8832(1)Å 9.4 vol%
Carbide, fcc ($M_{23}C_6$)	*a* = 10.660(1)Å 0.2 vol%	*a* = 10.6375(4)Å 0.2 vol%
Nepheline, hexagonal ($NaAlSiO_4$)		*a* = 9.9912(6)Å *c* = 8.3723(8)Å 0.8 vol%
Corundum, trigonal ($Al_{2-x}Cr_xO_3$)		n.r.* 0.4 vol%

* not refined

It is evident from the tabulated data that plant exposure at 540˚C gives rise to the formation of various phases. In the unexposed (U) parent material, the two main phases are austenite, (Aus_1) and $M_{23}C_6$ carbides. Aus_1 refers to the bulk lattice. Following 2 years plant exposure, the Aus_1 phase beneath the corroded surface starts to decompose, leaving behind a Cr-depleted matrix with a smaller austenite lattice parameter (i.e. *a*-value). In addition, essentially pure γ-Ni is observed at the corroded surface. This phase is probably brought to the surface by the syngas and is believed to stem from the catalyst nickel particles used upstream in the process. (to be discussed further in Part IV of the thesis)

Moreover, both nepheline ($NaAlSiO_4$) and also corundum ($Al_{2-x}Cr_xO_3$) are detected at the corroded surface. These findings are in excellent agreement with the X-ray maps shown previously in Fig. 3.4, revealing the presence of the constituent elements Cr-Al-O and Na-Al-Si-O at distinct positions. None of these oxide phases are commonly observed in connection with metal dusting corrosion.

Apparently, α-Cr (i.e ferrite) is also present at the surface, as indicated by the S-XRD data in Table 3.1. The mechanism of the α-Cr formation is not entirely clear, but it may be linked to the formation of the nepheline phase. A possible reaction path is that corundum initially forming a protective oxide, transforms to the thermodynamically more stable nepheline, leaving α-Cr as a reaction product at the surface. The nepheline phase was first observed in the FEG SEM in the form of 2 to 3µm large hexagonal single crystals, located at the surface, as shown in Fig. 3.6. Chemical mapping revealed that the crystals contained a substantial amount of Na (e.g. see Fig. 3.4), and based on this information, the unknown compound was identified as nepheline, according to the Powder Diffraction Files (PDF). This phase is among the most stable oxides that are known, and only small amounts of Na (at the ppb level) are sufficient to form the nepheline phase. Under the prevailing circumstances it is believed that nepheline forms as a result of reactions between corundum, Na and SiO(g), the latter two substances being brought to the surface by the syngas.

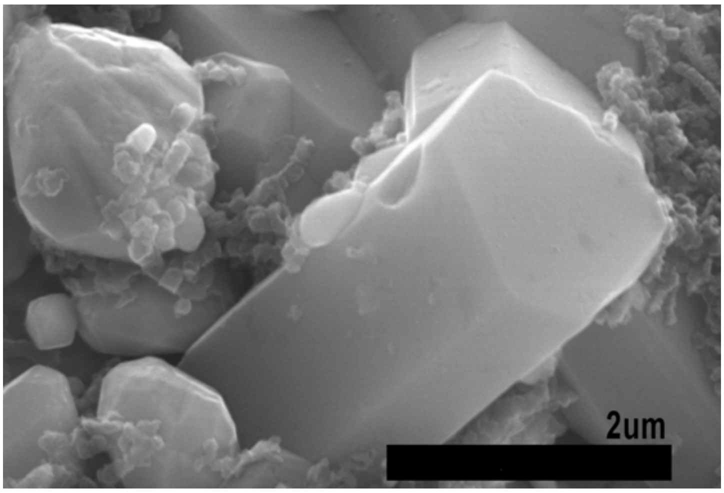

Figure 3.6 Secondary electron image of nepheline crystal observed at corroded surface of plant exposed alloy 602.

3.4. Conclusions

- In general, alloy 602 is found to exhibit a high intrinsic resistance to metal dusting corrosion in process gas mixtures relevant for methanol or Fischer-Tropsch synthesis. After 2 years of plant exposure to a syngas environment, pits are present on the corroded surface. However, the observed material loss is negligible, reflecting the fact that only a thin zone, extending about 20µm into the bulk of the material, is seen to be enriched with respect to Cr-containing precipitates.

- At the operating temperature of about 540˚C, the 602 alloy is prone to secondary precipitation hardening, leading to a general increase in the bulk hardness of about 75 HV after 2 years of exposure. In other respects, the high temperature stability of the alloy is good, suggesting that mechanical degradation of the parent material should not be a problem during service.

- In Ni-based superalloys, balanced alloying with aluminium and chromium improves the intrinsic resistance to metal dusting corrosion. During plant exposure, these elements contribute to the formation of a stable surface oxide layer, presumably corundum, $Al_{2-x}Cr_xO_3$, which prevents carbon from penetrating deep into the bulk of the material. From this natural surface oxide, the nepheline phase, $NaAlSiO_4$, starts to grow, probably due to reactions between corundum, Na and SiO(g). The latter two substances are transported to the surface by the syngas which contains traces of these elements at the ppb level.

3.5. References

1. D. J. Tillack, J. E. Guthrie, "*Wrought and cast heat-resistant stainless steels and nickel alloys for the refining and petrochemical industries*", in NiDI Technical Series, Report No.10071, Nickel Development Institute, Birmingham, England, 1998.
2. B. A. Baker, G. D. Smith, S. A. McCoy: *Ammonia plant safety (and related facilities)*, 2002, vol.42, pp. 257-267.
3. S. Strauss, H. J. Grabke: *Materials and Corrosion*, 1998, No.5, vol. 49, pp. 321-327.
4. P. Szakálos: *Materials and Corrosion*, 2003, No.10, vol. 54, pp. 756-762.
5. D. C. Agarwal, U. Brill, "*Performance of alloy 602CA in high temperature environments up to 1200ºC (2200ºF)*", paper presented at Corrosion/2000, Orlando, Florida, USA, 26.-31.March 2000, NACE International, Houston, Texas, USA.
6. H. J. Grabke: *Materials and Corrosion*, 1998, No.5, vol. 49, pp. 303-308.
7. B. Schmid, Ø. Grong, R. Ødegård: *Materials and Corrosion*, 1999, No.11, vol. 50, pp. 647-653.
8. H. J. De Bruyn, E. H. Edwin, S. Brendryen, "*Apparent influence of steam on metal dusting*", paper presented at Corrosion/2001, Houston, Texas, USA, 11.-16.March 2001, NACE International, Houston, Texas, USA.
9. P. Szakálos, R. Pettersson, S. Hertzman: *Corrosion Science*, 2002, No.10, vol. 44, pp. 2253-2270.
10. P. Szakálos: "*Mechanisms of Metal Dusting*", PhD Thesis, KTH - Royal Institute of Technology, Department of Materials Science and Engineering, Stockholm, 2004.
11. A. C. Larson, R. B. Von Dreele: GSAS, General Structure Analysis System, LANSCE, S-H805, Los Alamos National Laboratory, Los Alamos, 2000.

PART IV

Surface disintegration of nickel-based alloys during long time exposure to syngas in an industrial plant for methanol production.

4.1. Introduction

The major impetus for developments in nickel-based alloys for high-temperature applications has been provided by the need for improved chemical and microstructural stability during service.[1-6] Experience has shown that oxidising, reducing or a combination of both environments can be responsible for surface degradation and corrosion attack during high-temperature exposure.[3] Oxidising environments refer to gas compositions with high oxygen partial pressures, while reducing environments are characterised by low oxygen partial pressures or by a high carbon activity in carbonaceous gas phases.[1] In syngas atmospheres, rich in carbon monoxide and hydrogen, a special form of high-temperature corrosion can occur, frequently referred to as metal dusting (MD) corrosion.[7]

Extensive research, mainly in the laboratory, has been performed to explain the degradation mechanisms of MD in both iron and nickel-based alloys over the years.[8-13] It is generally accepted that MD is related to carburisation occurring at temperatures typically between 400ºC and 800ºC.[1, 14, 15] A high carbon activity in the gas phase usually accelerates the corrosion process, but still concurrent oxidation reactions are believed to play a role in the metal dusting attacks.[16-18] Although advanced nickel-based alloys are frequently used to reduce MD induced material degradation, the failure cases reported by Eberle and Wiley,[19] Holland and De Bruyn,[20] and Grabke[21] highlight the complexity of the materials selection. Obviously, the MD-resistance depends on the interplay between a number of variables that cannot readily be accounted for by simple thermodynamic calculations based on knowledge of bulk compositions. In particular, the role of minor alloying elements is of importance, especially strong oxide and carbide formers such as Al, Cr, Nb, Co, Zr and Y.[22-24] For example, it has been suggested that carbon ingress into the bulk phase during exposure can be reduced by balanced additions of chromium and aluminium to Ni-based alloys.[22, 24-26]

In addition to alloy composition, the MD corrosion resistance is also affected by gas composition, temperature, pressure and time.[27, 28] Most high-temperature materials reveal metallurgical changes following long term use, and sometimes these attacks can be difficult to understand and explain.[29] It is also suggested that the presence of trace elements in the gas phase at the ppm or ppb level may interfere with the reactions taking place at the surface during exposure. Recently, it has been shown that the presence of elements such as Na and Si in the process gas leads to the formation of new oxide phases at the surface of Ni-based alloys that are not observed after exposure to synthetic gases in the laboratory.[30, 31]

Since gas-metal interactions normally occur on an atomic level, the use of complementary high-resolution experimental techniques is important to reveal the reaction products and determine the mechanisms involved.[11, 30] In the present investigation, long time exposure of two nickel-based alloys containing different amounts of aluminium and chromium has been performed in an industrial plant for methanol production. A number of complementary high-resolution experimental techniques have then been applied to characterise the surface reaction products and assess the microstructural stability of the alloys after 2 and 4 years of syngas exposure. By these means, new and important information about the reactions taking place between minor elements present in the metal and gas phases has been obtained. Some unexpected microstructural changes occurring as a consequence of these reactions have also been identified, which, following interpretation, has lead to a more verified understanding of the degradation mechanism involved.

4.2. Experimental

Part IV deals mainly with the 2 years plant exposed alloys 602 and 693, where the iron-based APMT alloy is used as a reference material to clarify the origin of the observed Ni-deposit on the surface of the alloys. The experimental techniques being used include:

- Light microscopy
- Hardness measurements
- Scanning electron microscopy (FEG SEM)
- Transmission electron microscopy (TEM / STEM)
- Synchrotron X-ray diffraction (S-XRD)

Further detailes are given in Part II of the thesis.

4.3. Results

4.3.1. Microstructural stability during exposure

Figure 4.1 shows optical micrographs of alloy 602 in the as-received and plant exposed conditions. As expected, the original microstructure of the parent material consisting of 50 to 100μm large austenite grains and coarse $M_{23}C_6$ carbides is preserved in the bulk of the two plant exposed samples. After 2 years of exposure, only a few metal dusting corrosion pits are observed on the surface. However, the corrosion attack becomes more uniform after 4 years of exposure, leading to the formation of 20 to 50μm deep pits along the surface. Adjacent to the pits the characteristic white zone is observed. This contains a high fraction of Cr_3C_2 carbides, as documented in Part V of the present thesis employing TEM diffraction pattern analyses.[32]

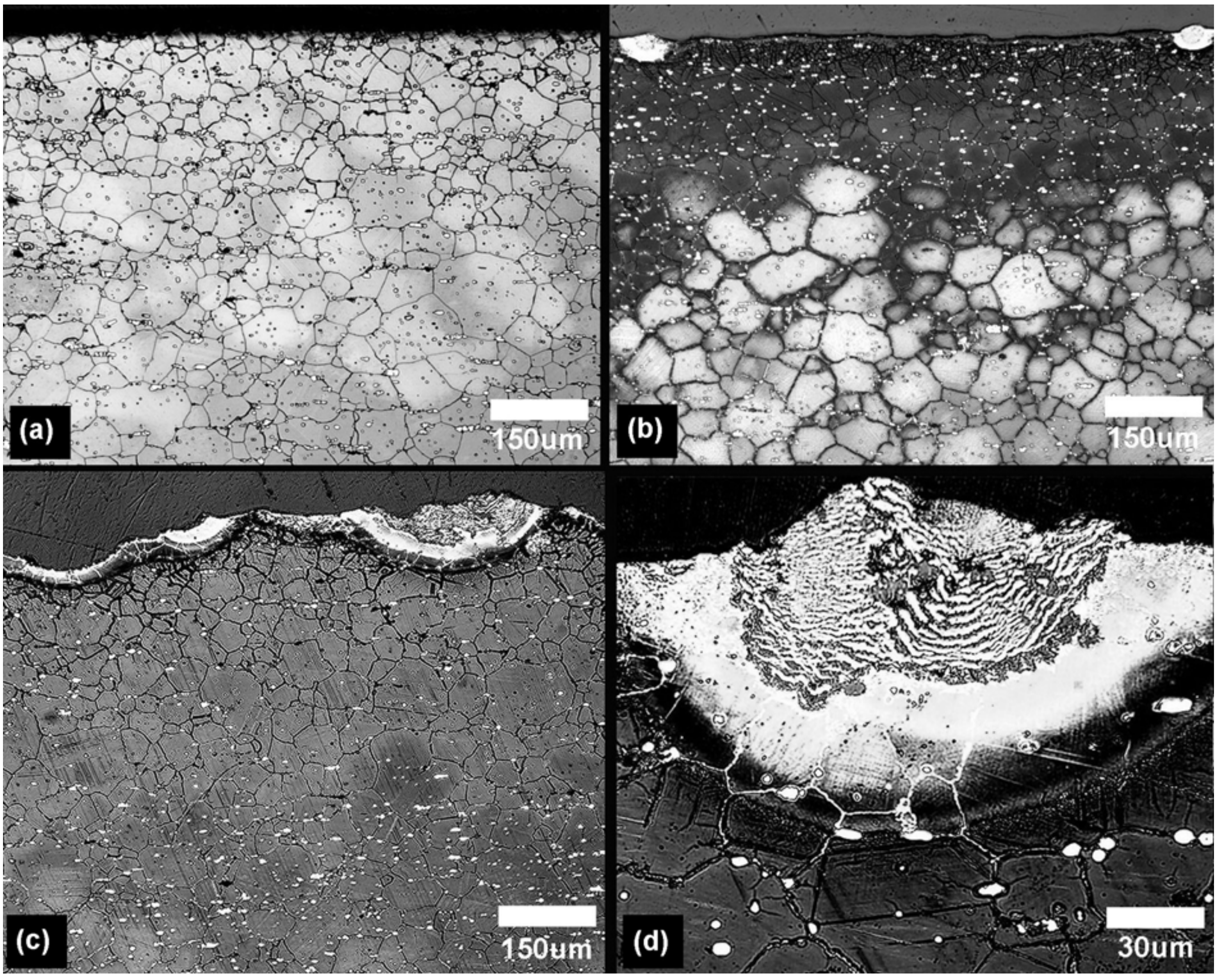

Figure 4.1 Optical images showing the bulk and surface-near microstructures of alloy 602 following different exposure conditions; (a) As-received material, (b) 2 years of plant exposure, (c) 4 years of plant exposure, (d) Close-up of corrosion pit formed after 4 years of plant exposure.

In contrast, the initial austenite grain structure of alloy 693 is seen to be significantly coarser, as shown by optical micrographs in Fig. 4.2 (a). Also, the response of alloy 693 to tempering at 540˚C is highly different compared to that of alloy 602. This follows from a comparison between the micrographs of the two plant exposed samples in Fig. 4.2. In both cases the original grain structure has completely vanished and is replaced by a secondary transformation product. This masking probably reflects a phase transformation occurring at an early stage of the tempering process, since the same transformation product also is present along the original grain boundaries of the steam oxidised specimen. On the other hand, the overall resistance to metal dusting corrosion seems not to be affected by the transformation, as the 4 years plant exposed sample only reveals evidence of a small number of hemispherical pits at the surface.

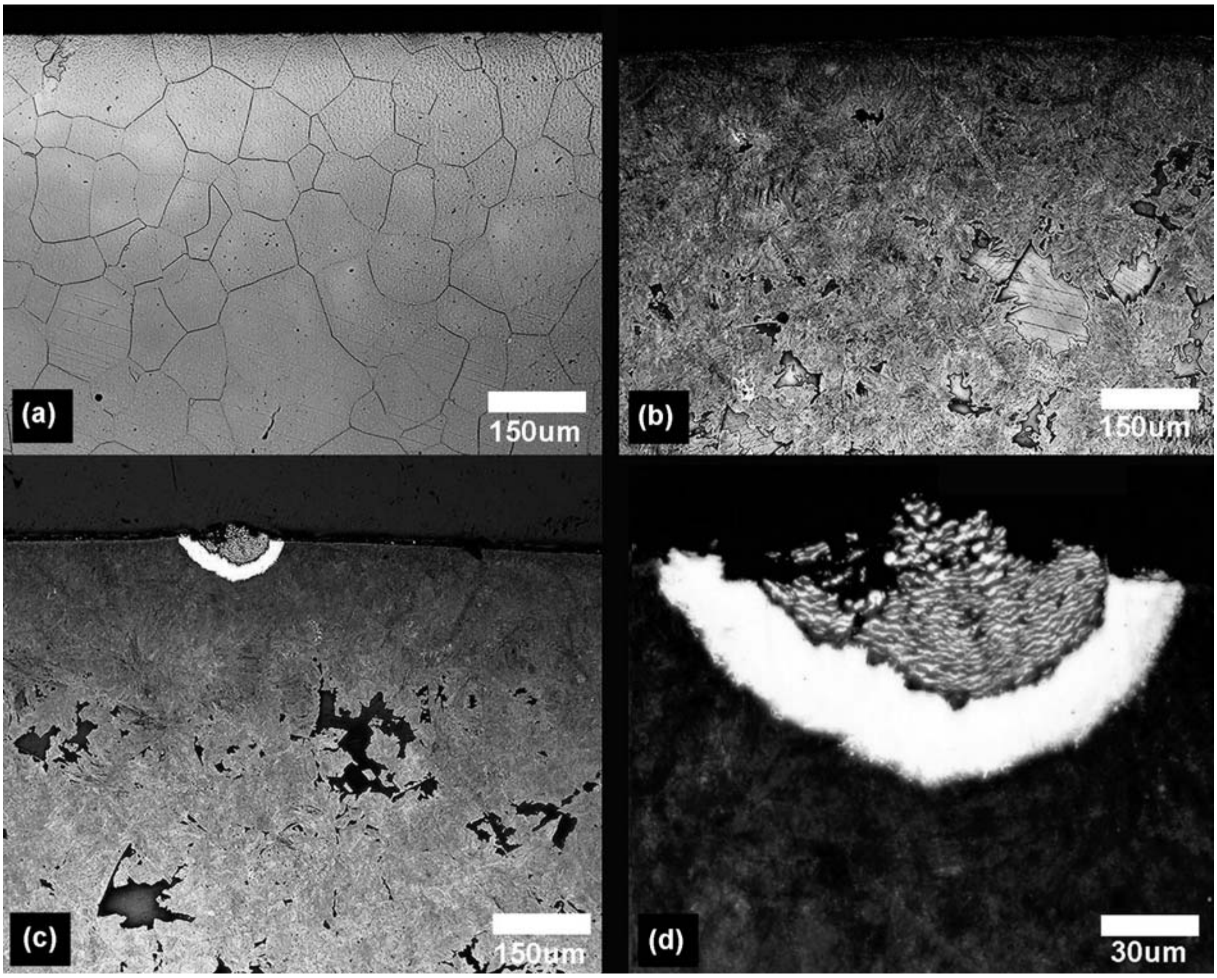

Figure 4.2 Optical images showing the bulk and surface-near microstructures of alloy 693 following different exposure conditions; (a) As-received material, (b) 2 years of plant exposure, (c) 4 years of plant exposure, (d) Close-up of corrosion pit formed after 4 years of plant exposure.

The results from the hardness measurements of alloys 602 and 693 following different exposure conditions are summarised in Fig. 4.3 (a) and (b), respectively.

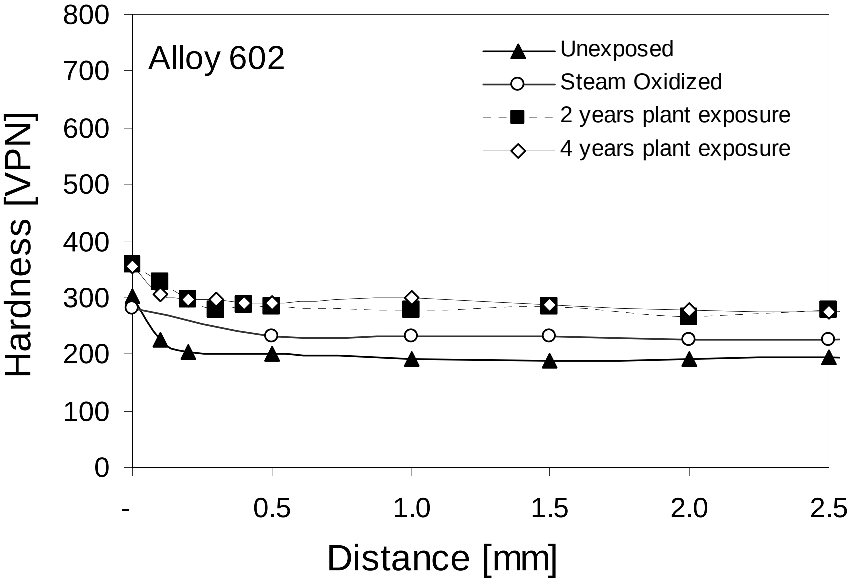

(a)

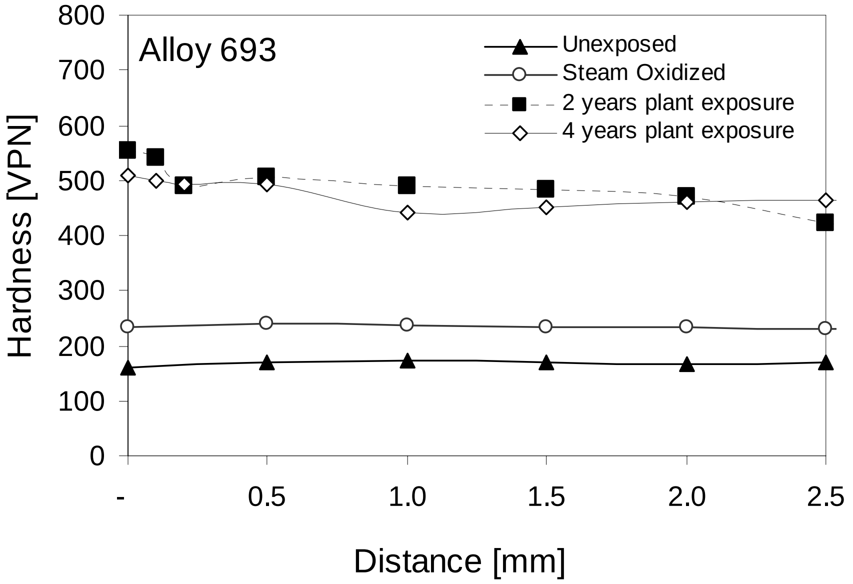

(b)

Figure 4.3 Plots of measured hardness profiles in the cross section of the materials following different exposure conditions; (a) Alloy 602, and (b) Alloy 693.

In the unexposed condition the hardness is about 200HV in alloy 602 and approximately 180HV in alloy 693. Notice that alloy 602, which is a cold deformed material, displays an increased hardness in the surface-near region, independent of choice of exposure conditions. Moreover, it is evident from Fig. 4.3 that the hardness increase following steam oxidation is much larger in alloy 693 than in alloy 602, which just shows a weak tendency to secondary precipitation hardening. The different ways the two alloys respond to tempering becomes even clearer after 2 and 4 years of plant exposure, where the hardness increases to a level between 400 to 500HV in alloy 693, as opposed to about 300HV in alloy 602. It is obvious that this dramatic hardness increase in alloy 693 is associated with the previously noted phase transformation in Fig. 4.2, a point which will be further elaborated and discussed in the forthcoming sections of the thesis.

4.3.2. Phases detected by X-ray diffraction

The results from the Synchrotron X-ray diffraction experiments are summarised in Tables 4.1 (a) and (b). These tables contain refined lattice parameters along with estimates of their relative volume fractions (in percent of the phases detected) to depths of approximately 10µm below the surface of the exposed samples. Corresponding data for the two unexposed alloys are provided for comparison.

Table 4.1(a) Phases detected close to the surface of alloy 602 following different exposure conditions using synchrotron XRD. Each column contains data for estimated relative volume fractions (in percent) and measured lattice parameters, *a*, *b* and *c* (in Angstrom). Numbers in paranthesis yield standard deviation of XRD experiments.

Penetration depth	11.5µm	6.1µm	11.0µm	9.8µm
Phases detected	Exposure conditions			
	Unexposed	Steam Oxidised	2 Years exp.	4 years exp.
Aus_1, fcc *(Ni,Cr,Fe)*	a=3.5851(1) 99.8 vol%	a=3.5775(1) 99.7 vol%	a=3.5684(1) 83.0 vol%	a=3.5684(1) 66.5 vol%
Ni-deposit, fcc (γ-Ni)			a= 3.5395(1) 6.2 vol%	a= 3.5357(1) 27.9 vol%
Ferrite, bcc (α-Cr)			a= 2.8832(1) 9.4 vol%	a= 2.8831(1) 2.8 vol%
Carbide, fcc ($M_{23}C_6$)	a=10.660(1) 0.2 vol%	a=10.6390(5) 0.3 vol%	a=10.6375(4) 0.2 vol%	a=10.6381(5) 0.2 vol%
Nepheline, hexagonal ($NaAlSiO_4$)			a=9.9912(6) c=8.3723(8) 0.8 vol%	a=9.9872(6) c=8.3670(5) 1.3 vol%
Corundum, trigonal ($Al_{2-x}Cr_xO_3$)		not refined	not refined 0.4 vol%	
Alumina, trigonal (α-Al_2O_3)				a=4.764(3) c=12.972(5) 0.5 vol%
Chromite, trigonal (Cr_2O_3)				a=4.965(2) c=13.564(6) 0.8 vol%

Table 4.1(b) Phases detected close to the surface of alloy 693 following different exposure conditions using synchrotron XRD. Each column contains data for estimated relative volume fractions (in percent) and measured lattice parameters, *a*, *b* and *c* (in Angstrom). Numbers in paranthesis yield standard deviation of XRD experiments.

Penetration depth	7.1μm	4.9μm	10.2μm	10.2μm
Phases detected	Exposure conditions			
	Unexposed	Steam Oxidised	2 Years exp.	4 years exp.
Aus_1, fcc *(Ni,Cr,Fe)*	*a*=3.5959(1) 100 vol%	*a*=3.5703(1) 74.7 vol%	*a*=3.5682(1) 69.1 vol%	*a*=3.5682(1)* 16.5 vol%
Ni-deposit, fcc (γ-Ni)			*a*=3.5378(1) 12.3 vol%	*a*=3.5330(1) 53.4. vol%
Aus_2, fcc *(Ni,Cr,Fe)*				*a*=3.538-3.565(1) 24.4 vol%
Ferrite, bcc (α-Cr)		*a*=2.8832(1) 25.3 vol%	*a*=2.8834(1) 16.9 vol%	
Nepheline, hexagonal $(NaAlSiO_4)$			*a*=9.9926(6) *c*=8.3716(10) 1.1 vol%	*a*=9.988(1) *c*=8.366(2) 0.4 vol%
Corundum, trigonal $(Al_{2-x}Cr_xO_3)$		not refined	not refined 0.6 vol%	
Alumina, trigonal $(\alpha\text{-}Al_2O_3)$				*a*=4.760(1) *c*=12.988(5) 0.8 vol%
Chromite, trigonal (Cr_2O_3)				*a*=4.9507(1) *c*=13.554(2) 4.5 vol%

* Lattice parameter and profile functions are kept at values identical to the 2 years exposure

In Tables 4.1 (a) and (b), the Aus_1 phase refers to the original austenite lattice in the alloys. This phase is largely preserved at the surface during exposure, although solute depletion of the matrix leads to a gradual decrease in the measured lattice parameters. Moreover, it is evident that the identity of the $M_{23}C_6$ carbide phase in alloy 602 is not lost within the surface-near regions during exposure, showing that the phase is thermodynamically stable under the prevailing circumstances. Still, the materials are not inert towards the gas atmospheres, as can be seen from the number of new phases that are observed in Tables 4.1 (a) and (b).

Starting with the steam oxidised specimens, the X-ray data reveal that both materials contain a surface oxide consisting of alumina and chromite. In Tables 4.1 (a) and (b) this mixed oxide is tentatively referred to as unstoichiometric corundum ($Al_{2-x}Cr_xO_3$). The corundum phase has a lattice parameter that falls between that of α-Al_2O_3 (a = 4.755Å, c = 12.99Å) and Cr_2O_3 (a = 4.9607Å, c = 13.599Å), all with the same $R3c$ space group symmetry. Unfortunately, a more exact identification of the surface oxide layer is not possible by X-ray diffraction because the spread in the signals from the individual small and perhaps unstoichiometric crystallites result in non-uniform broad peaks that cover the entire Cr_2O_3 – α-Al_2O_3 range. In addition, alloy 693 is seen to contain a high volume fraction of α-Cr following steam oxidation, which probably is associated with the previously noted phase transformation in Fig. 4.2. The same type of mixed alumina-chromite oxide is also observed at the surface of the alloys after 2 years of plant exposure, but in this case it appears together with nepheline ($NaAlSiO_4$), which is a hexagonal oxide phase with lattice parameters a = 9.9926Å and c = 8.3716Å. Since nepheline contains large amounts of the syngas trace elements Na and Si, it must have formed as a result of an exchange reaction with the syngas atmosphere. Moreover, both alloys contain crystallites of essentially pure γ-Ni and α-Cr at the surface after 2 years of plant exposure, i.e. before the onset of the MD corrosion attacks. It has previously been established that the Ni-deposit is an erosion product that stems from the nickel catalyst being used upstream in the process.[31] Therefore, the same Ni-deposit is also observed at the surface of the plant exposed samples of the iron-based alloy as well, which contains no nickel. This is fully documented in Appendix I, showing the S-XRD results along with a series of FEG SEM images of the iron-based alloy. In contrast, the α-Cr being observed at the surface is a result of reactions taking place within the materials during exposure, which in the case of alloy 693 can be traced back to the previously noted phase transformation.

After 4 years of plant exposure, the picture becomes more complicated, as shown by the results in Tables 4.1 (a) and (b). Whereas nepheline is still present at the surface of both alloys, the surface oxide is now developed further into two distinct products; pure alumina (α-Al_2O_3) and pure chromite (Cr_2O_3), the latter being the dominating oxide phase in alloy 693. In the case of alloy 693, it is evident that the α-Cr phase has completely vanished from the surface, probably oxidised to Cr_2O_3, since a distinct increase in the chromite volume fraction is apparent. Note that the new phase, labelled Aus_2, in Table 4.1 (b), was introduced to handle the scattered intensity falling in-between the peaks ascribed to Aus_1 and γ-Ni. This phase represents a transition zone, where Aus_1 approaches pure Ni. The Aus_2 phase forms either as a result of solute depletion or because the Ni-deposit dissolves into the Aus_1 phase. Still, there is enough Ni present from the catalyst to cover the surface of alloy 693 after 4 years of plant exposure, as indicated by the volume fraction data in Table 4.1 (b). Extensive nickel deposition is also observed on the surface of alloy 602, but in this case there is no need to introduce a new Aus_2 phase because the Aus_1 to Ni transition can be adequately handled by the profile parameters fitted to the parent phases. In addition, isolated crystallites of α-Cr are present at depths down to about 10μm beneath the surface, suggesting that it is effectively protected from carburisation and oxidation at a subsurface position.

4.3.3. Phases observed in TEM and SEM

Before describing details of the phase distribution at the surface of the plant exposed samples, it is appropriate to start with a characterisation of the mixed alumina-chromite oxide layer which forms during steam oxidation. As shown by the TEM bright field image of the surface-near region of alloy 602 in Fig. 4.4, the thickness of this oxide layer is approximately 50nm.

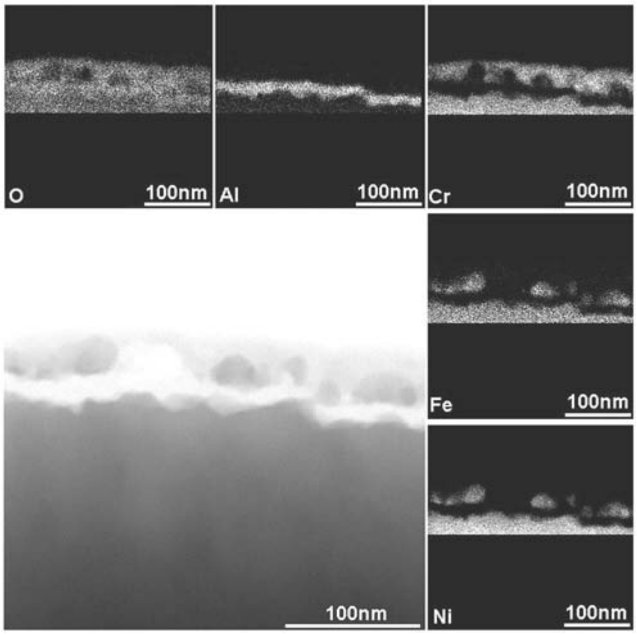

Figure 4.4 TEM bright field image of the cross section of alloy 602 following steam oxidation. The smaller images show the corresponding X-ray maps of main constituent elements from the same surface area.

The layer itself consists of an inner zone being rich in aluminium and oxygen and an outer zone being rich in chromium and oxygen. This follows from a comparison of the corresponding X-ray element images in the figure. In-between these two layers, nanometre sized metal particles containing Ni and Fe are observed. They probably form by selective oxidation of the original Aus_1 lattice, which contains large amounts of Cr in solid solution along with Al in the form of γ ′- Ni_3Al hardening precipitates. The same type of surface oxide is also present in the 2 years plant exposed samples, as shown by the synchrotron X-ray data in Tables 4.1 (a) and (b), although, as pointed out above, the individual peaks of Cr_2O_3 and α-Al_2O_3 cannot readily be revealed by X-ray diffraction. However, after 4 years of plant exposure these phases have grown to an extent which makes this possible, leading to the identification of alumina and chromite in the surface-near regions of both alloys.

Further information about the phase distribution at the surface of the plant exposed samples can be obtained by examining the different plan view and cross section samples in the FEG SEM. As shown by the plan view images in Fig. 4.5, both the previously detected nepheline phase and the pure Ni crystallites are located on the top of the surface.

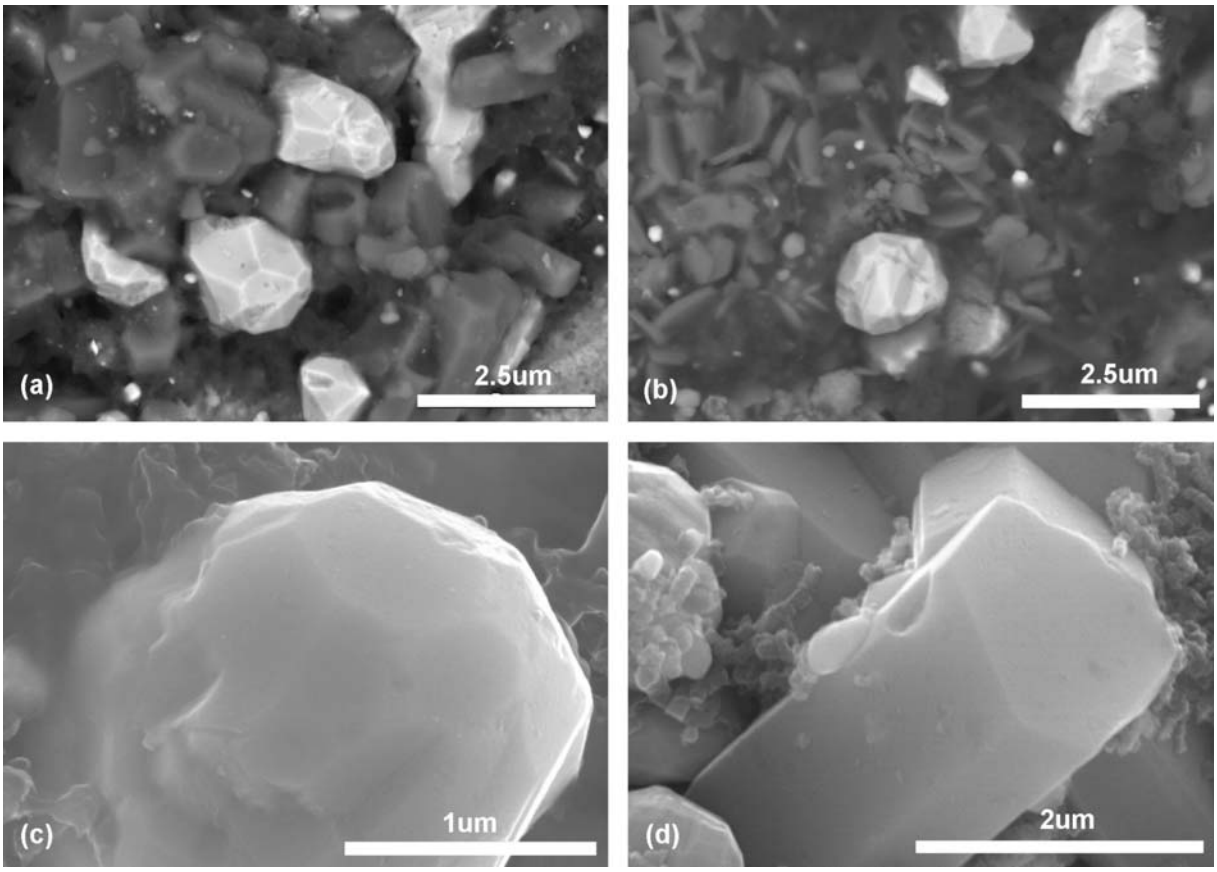

Figure 4.5 FEG SEM images of the surface (plan view) after 2 years of plant exposure; (a) BSE image of alloy 602, (b) BSE image of alloy 693, (c) Enlarged SE image of deposited nickel particle on surface of alloy 602, (d) Enlarged SE image of nepheline crystal on surface of alloy 602.

After 2 years of plant exposure, the Ni particles are typically in the 1μm size range and appear faceted, suggesting that they grow by successive attachment of atoms to the highly developed low-index crystallographic planes facing the process gas. This characteristic growth mode is fully consistent with the observation that the Ni crystallites stem from reactions with the process gas and are not ordinary corrosion products. The nepheline crystals are, in turn, embedded in-between these Ni-particles. They exhibit the characteristic hexagonal geometry and grow in directions facing outwards from the surface, toward the gas phase along their *c*-axis. In addition, large amounts of graphite can be observed on the top of the exposed surfaces, showing that the Boudouard reaction ($2CO = C + CO_2$) is operative under the prevailing circumstances. The situation is quite similar after 4 years of plant exposure, apart from the fact that the nickel deposition in this case is further accentuated.

Figure 4.6 shows a corresponding FEG SEM backscatter electron image of the cross section of alloy 602 after 2 years of plant exposure along with X-ray maps of the main constituent elements. The maximum depth being viewed is about 3µm, referring to the surface of the sample.

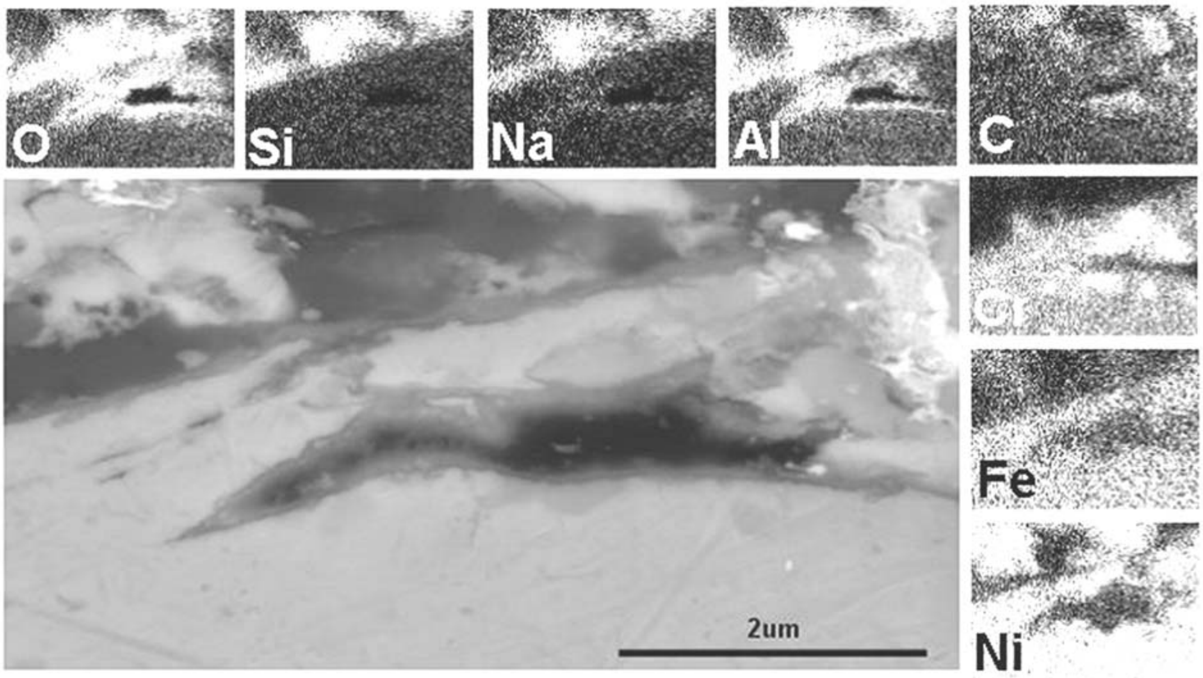

Figure 4.6 FEG SEM BSE image of cross section of alloy 602 following 2 years of plant exposure. The smaller images show the corresponding X-ray maps of main constituent elements from the same surface area.

A closer inspection of Fig. 4.6 reveals that a crack is present approximately 1.5µm beneath the exposed surface. It is apparent that the inner surface of the crack is completely covered by a thin layer of α-Al_2O_3. Moreover, sodium (Na) is observed in the vicinity of the oxide due to the nepheline formation. Moreover, the chromium rich spots, observed adjacent to the crack surface, could be the α-Cr or the $M_{23}C_6$ carbide phase being identified by synchrotron XRD.

Alternatively, the Cr-rich spots in Fig. 4.6 could be chromium oxide (Cr_2O_3), as indicated by the EDS data for oxygen. Unfortunately, the pertinent overlap between the $K\alpha$ radiation energy of oxygen (0.526keV) and the $L\alpha$ radiation energy of chromium (0.573keV) in the X-ray spectrum makes the oxygen identification in Fig. 4.6 rather uncertain. Nevertheless, the crack must be associated with oxide formation, and has probably developed as a result of this phase formation. Beneath the crack the solute depleted Aus_1 phase appears, containing Fe and some Cr in solid solution.

By utilising the FIB sample of alloy 693 in combination STEM/TEM analyses, further information about the local phase distribution at the surface following 2 years of plant exposure has been obtained. As shown by the annular dark field electron image in Fig. 4.7, a small crack exists about 0.2 to 0.4μm beneath the corroded surface. The corresponding X-ray element maps reveal that aluminium is concentrated to the inner surfaces of the crack, probably in the form of a dense nanolayer of α-Al_2O_3. Moreover, the nepheline phase, containing the constituent elements Na, Al, Si, and O, is observed in the upper part of the image, which in Figure 4.5 is seen to grow in different directions outwards from the surface towards the gas atmosphere.

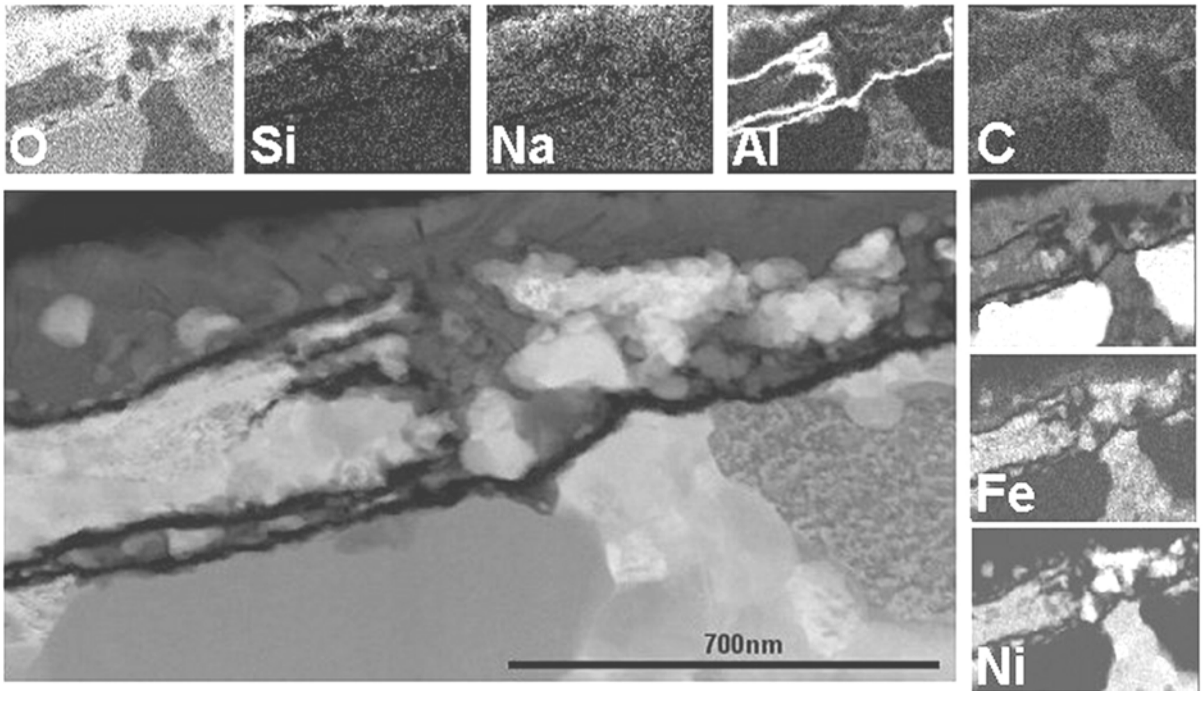

Figure 4.7 STEM annular dark field image of cross section of alloy 693 following 2 years of plant exposure. The smaller images show the corresponding X-ray maps of main constituent elements from the same surface area.

Beneath the crack in Figure 4.7 two distinct compositions are observed, one yielding Cr and one yielding the matrix elements Ni and Fe. The latter phase also contains significant amounts of carbon. These two regions are presumably α-Cr and the Aus_1 phase being previously detected by synchrotron XRD. It is evident from the X-ray element maps that full partitioning of elements Cr and Ni + Fe has occurred during exposure, probably as a result of the previously noted phase transformation. Element partitioning is also observed at other locations closer to the surface, suggesting that α-Cr and the Aus_1 phase are evenly distributed throughout the analysed volume.

The fact that the Cr-rich regions in Fig. 4.7 are pure α-Cr and not chromite or some metastable chromium carbide of the Cr_7C_3 or Cr_3C_2 type has also been verified by independent diffraction pattern analyses in the TEM, employing the same FIB sample as in the STEM examination. These results, which are summarised in Fig. 4.8, show that the reflections stem from a cubic phase with a lattice parameter close to 2.9Å, conforming to α-Cr, in agreement with the S-XRD results.

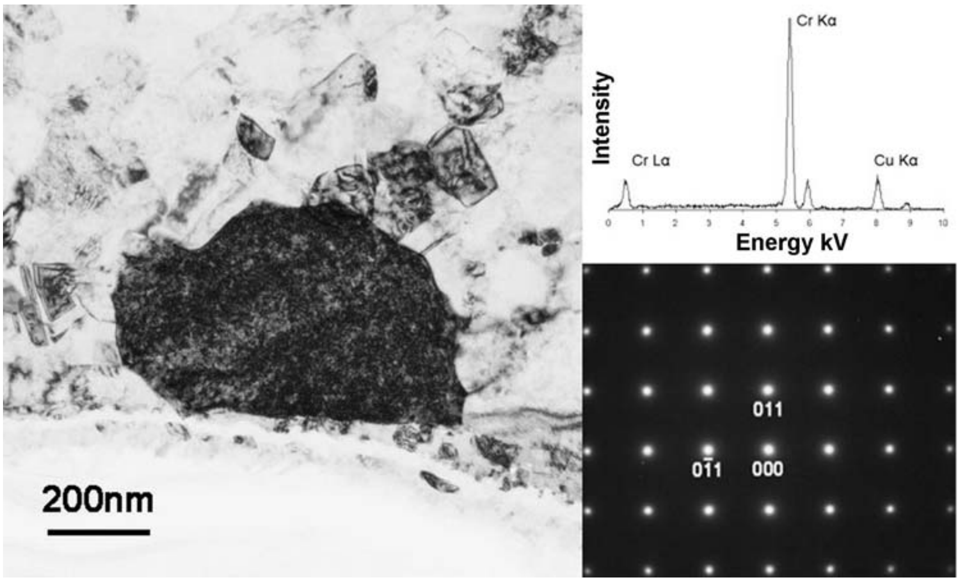

Figure 4.8 TEM bright field image of Cr-rich phase located at the surface of alloy 693 following 2 years of plant exposure. Included are also the results from the EDS and the diffraction pattern analyses identifying the phase as α-Cr.

4.4. Discussion

Based on a consideration of the above results, it is obvious that both alloys exhibit a high intrinsic resistance to metal dusting corrosion following 2 years of plant exposure to syngas at about 540^{o}C. However, the resistance to metal dusting corrosion gradually decreases as the surface disintegration proceeds, and after 4 years the attack is nearly uniform in the case of alloy 602. Although the performance of alloy 693 is better with respect to metal dusting, the resulting formation of corrosion pits at the surface of both alloys must be closely linked to the observed surface disintegration occurring earlier during exposure. This eventually leads to break-down of the surface oxide layer and subsequently to diffusion of carbon into the bulk of materials, as shown by the characteristic white zone of non-etching carbides which forms in front of the pits in Figs. 4.1 and 4.2.

Thus, in order to understand the subsequent development of the metal dusting corrosion pits in these nickel-based alloys after 4 years of plant exposure, the previous chemical and structural changes taking place within the surface-near regions of the exposed samples after 2 years must be clarified and explained. It will be shown below that this is possible by considering the reaction kinetics involved and the pertinent gradients in the carbon activity and oxygen partial pressures across the entire surface region. On the other hand, details of the pit formation and resulting carbon diffusion into the bulk of the materials are not considered here, as these matters will be duly discussed in Part V of the present thesis dealing with the mechanisms of metal dusting corrosion in the 4 years plant exposed samples.

4.4.1. Conditions for α-Cr formation in alloy 693

It is appropriate to start with a discussion of the observed phase transformation in alloy 693, which leads to formation of α-Cr both at the surface and in the bulk of the alloy after some few hundred hours of tempering at 540^{o}C. Notice that α-Cr has not previously been observed in nickel-based alloys, although it’s existence is predicted thermodynamically.[33] This may be because the precipitation involves growth of a *bcc* phase within a parent *fcc* lattice, which suggests that the associated kinetics are so slow that the reaction is not released under normal service temperatures and plant operating conditions.

But in alloy 693 the conditions for α-Cr precipitation are particularly favourable because of its high chromium, aluminium and iron contents. Whereas Fe decreases the solubility of Cr in nickel by partitioning to the γ-Ni phase, Al indirectly enhances the α-Cr precipitation by draining Ni from the matrix through the formation of the hardening γ'- Ni_3Al phase.[33] An idea of how large this latent supersaturation actually is can be obtained from a simple mass balance by considering for the amount of nickel being bound to aluminium. Taking the stoichiometric conversion factor between Ni and Al in Ni_3Al equal to 6.52, 3.3 wt% Al is able to tie-up about 21.5 wt% Ni. By subtracting this number from the nominal nickel content of 58.6 wt%, one arrives at an effective Cr to Ni ratio in alloy 693 of about 0.8. This ratio is considerably larger than that calculated from the nominal chemical composition, which yields a value of about 0.5. Although both values are within the two-phase region of the binary Ni-Cr phase diagram[34] (thereby suggesting α-Cr precipitation), the resulting supersaturation, as inferred from the former estimate, is so high that it fully explains the release of the phase transformation during tempering, in spite of the slow kinetics involved. On this basis it is not surprising to find that the original grain structure of both steam oxidised and plant exposed samples is completely masked by the α-Cr transformation product, as shown previously by the optical micrographs in Fig. 4.2. Considering the fact that the hardness of α-Cr is about 1350 Vickers, the hardness data reproduced in Figs. 4.3 (b) suggest that the volume fraction of α-Cr is of the order of 0.25 close to the surface of the 693 alloy. In these calculations it is assumed that the rule of mixtures applies, i.e. that the measured hardness of about 500VPN in the matrix at the surface position is a linear function of the hardness in α-Cr and the γ-Ni phase, respectively multiplied by their corresponding volume fractions. The value agrees reasonably well with the synchrotron XRD data for the 2 years plant exposed sample in Table 4.1 (b), yielding a volume fraction of about 0.17.

4.4.2. Conditions for α-Cr formation in alloy 602

It’s convenient to continue with a discussion of the α-Cr formation in alloy 602, where precipitation of α-Cr occurs locally following long time plant exposure. It follows from the synchrotron XRD data in Tables 4.1 (a) and (b) that the amount of α-Cr is approximately 50% lower compared to alloy 693 after 2 years of plant exposure. This can partly be explained by a lower chromium content, since alloy 602 contains less chromium than alloy 693. Thus, if corrections are made for the amount of nickel being tied-up as γ'- Ni_3Al precipitates, one arrives at an effective Cr to Ni ratio of 0.52 in alloy 602 compared to 0.40 if the nominal chemical composition is used. The latent supersaturation for the α-Cr precipitation in alloy 602 is therefore lower than in alloy 693. Still, the Cr to Ni ratio is within the two-phase region of the binary Ni-Cr phase diagram, suggesting that α-Cr is thermodynamically stable at 540°C. However, this latent supersaturation is evidently not large enough for the new *bcc* phase to nucleate and grow within the *fcc* lattice of the bulk material, meaning that the α-Cr formation in alloy 602 is probably released by local reactions occurring at the surface during exposure.

The most obvious explanation to this phase transformation is that α-Cr in alloy 602 forms as a result of reactions between corundum (e.g. $AlCrO_3$) and the trace elements Na and Si being brought to the surface by the process gas:[31]

$$AlCrO_3 + Na + SiO\,(g) = NaAlSiO_4 + \alpha\text{-}Cr \tag{4.1}$$

However, considering the fact that the surface oxide actually consists of an outer layer of Cr_2O_3 and an inner layer of α-Al_2O_3, it is more likely that the nepheline phase ($NaAlSiO_4$) forms by reactions with α-Al_2O_3, which implies no α-Cr precipitation. Therefore, another explanation to this phase formation is sought.

Based on transformation kinetic theory it can be argued that a deformed microstructure containing a high dislocation density will assist both the nucleation and growth of the new phase within the parent solid material.[35] Firstly, the driving force for the precipitation reaction will be enhanced by the release of the strain energy accompanying the reduction in the dislocation density when the new phase forms within the pre-deformed matrix. Secondly, the dislocations themselves provide high diffusivity paths for transport of the constituent elements in the matrix, thereby increasing the overall transformation rate.[35] In alloy 602 the deformation zone, being introduced during thermomechanical processing of the parent material, is seen to extend about 250μm below the surface, as shown previously by the hardness data in Fig. 4.3 (a). In addition, during exposure the volume changes taking place as a result of the local oxide formation can lead to further stress build-up and strain accumulation at the surface.[32, 36, 37] This expansion is sufficiently large to promote cracking of the oxide layer and release the α-Cr precipitation within the adjacent Aus_1 matrix down to depths of about 10μm, as indicated by the synchrotron XRD data in Table 4.1 (a).

4.4.3. Local phase equilibria at the surface

The different phases that have been detected by synchrotron XRD in the 2 years plant exposed 602 and 693 alloys are summarised in Fig. 4.9. This description is representative of the phase relations being established at the surface prior to the onset of the metal dusting corrosion attacks. In the schematic drawing a distinction is made between phases that are present below and above the protective nanolayer of α-Al_2O_3, separating the metal phase from the porous reaction layer in contact with the bulk gas phase. On the left-hand side of the α-Al_2O_3 demarcation line, the solute depleted Aus_1 phase, which essentially is a binary Ni-Fe alloy, coexists with α-Cr (and $M_{23}C_6$ in alloy 602). On the right-hand side the two oxide phases $NaAlSiO_4$ and Cr_2O_3 are observed, along with Ni-particles coming from the catalyst located upstream in the process and coke deposited on these particles via the Boudouard reaction ($2CO = C + CO_2$).

Parent material		**Gas phase**	
Metal phase		Porous reaction layer	Bulk gas
•Aus_1 (Ni+Fe) •α-Cr •$M_{23}C_6$ (in alloy 602)	Dense α-Al_2O_3 nanolayer	•$NaAlSiO_4$ •Cr_2O_3 •γ-Ni •Coke	•CO •H_2 •CO_2 •H_2O •CH_4

Figure 4.9 Summary of the different phases detected in alloys 602 and 693 after two years of plant exposure. These phases are either present within the porous reaction layer facing the process gas or located on the inside of the protective α-Al_2O_3 layer covering the metal surface.

It is well established that Ni (along with other metals such as Fe and Co and their oxide counterparts) are efficient catalysts for the CO decomposition reaction.[38-40] The exact carbon activity a_{C} needed for graphite precipitation at the Ni-crystallites shown in Fig. 4.5 (a) and (b) is not known, but obviously it must be significantly lower than the corresponding carbon activity in the bulk gas phase, which is close to 100. In fact, calculations done by Szakálos *et* al.,[13, 18, 41] using ThermoCalc, suggest that the carbon activity at the surface of Ni-based alloys during metal dusting corrosion is slightly higher than unity at temperatures around 500ºC (i.e. $a_{\mathrm{C}} \approx 1.7$). This agrees well with the classical MD models of Grabke[42] and others,[43-47] who use $a_{\mathrm{C}} = 1$ as the lower limit for the carbon activity at the metal surface to explain the cementite (Fe_3C) decomposition in iron-based alloys in the presence of graphite.

Provided that the Boudouard reaction also controls the carbon activity at the gas/metal interface during the graphite precipitation, simultaneous reaction equilibrium calculations can be used to estimate the local gas composition at this position. As a starting point, the commercial software package FactSage[48] is used in combination with dedicated thermodynamic databases.[49] In these calculations a closed system is assumed, taking the total number of moles of gaseous components equal to unity (i.e. $n_{tot} = 1$) and the initial number of moles of each gaseous component in the gas mixture equal to their respective mole fractions in the bulk phase. By solving the appropriate set of independent equations under the conditions of $a_C = 1$ and $p_{tot} = 35$ bar, the partial pressures of the same gaseous components within the porous reaction layer at the surface (in equilibrium with solid carbon) have been calculated and compared with those in the bulk. The results are summarised in Table 4.2, which also gives order of magnitude figures for the resulting partial pressures of oxygen along with the numbers for the carbon activity at both locations.

Table 4.2 Calculated partial pressures of different gaseous components at the surface and in the bulk gas phase at 540°C for a_C equal to 1 and ~100, respectively. Included are also estimates for the resulting oxygen partial pressure at both locations.

Gas phase	Partial pressures of gaseous components (bar)					Gas characteristics	
	p_{CO}	p_{H_2}	p_{H_2O}	p_{CO_2}	p_{CH_4}	p_{O_2} a)	a_C
Bulk	5.3	16.4	10.8	2.1	0.4	~10^{-27} (10^{-28})	100
Surface	0.3	3.0	15.5	6.2	10.0	~10^{-25}(10^{-25})	1

a) Calculated from the reaction $H_2 + ½ O_2 = H_2O$. Values in brackets refer to the reaction $2CO + ½ O_2 = CO_2$

It is evident from Table 4.2 that the conditions are more oxidising at the surface compared with the bulk gas phase, where the Boudouard reaction is blocked and the carbon activity is close to 100. These partial pressure gradients will, in turn, give rise to transport of the same gaseous species across a stagnant thin film (referred to as the boundary layer) within the porous reaction layer itself. Specifically, for diffusion of gases the molar flux J_X (in mol/m^{2}s) of a gaseous component X across the boundary layer of thickness δ (in m) can be expressed as:[50]

$$J_X = \frac{D_X}{\delta RT}\left(p_X - p_X^*\right) = k_X\left(p_X - p_X^*\right) \tag{4.2}$$

where D_X is the diffusivity (in m^2/s), R is the universal gas constant (in m^3 atm /K mol), T is the absolute temperature (in K), p_X and p_X^* are the partial pressures of component X in the bulk gas phase and at the surface, respectively (in atmospheres), and k_X is the overall mass transfer coefficient (in mol / m^2 s atm).

It follows that k_X depends both on the diffusivity D_X and the thickness δ of the boundary layer. The latter parameter is again a function of the gas velocity and the geometry and dimensions of the surface. Because of the pertinent partial pressure gradients being established within the porous reaction layer during the graphite deposition (see Table 4.2), a steady state situation implies that there must be a continuous supply of the reducing components CO and H_2 from the bulk gas phase to the reaction front by diffusion according to equation (4.2). At the same time back diffusion of the reaction products H_2O, CO_2 and CH_4 occurs into the bulk. Hence, it is reasonable to assume that the rate of coke deposition taking place on the surface of the Ni catalyst particles is controlled by a complex (coupled) transport mechanism involving counter-diffusion of these components within the porous reaction layer itself. This kind of film model is frequently used to describe rate phenomena in analogous metallurgical systems involving mass transfer between a metal surface and a bulk gas phase,[51] and is deemed to be applicable to syngas exposure as well after the Boudouard reaction has been triggered.

4.4.4. Thermodynamic stability of observed phases

The next step is to verify that the different phases observed within the porous reaction layer at the surface are thermodynamically stable under the prevailing conditions. The results from these additional FactSage calculations are summarised in Fig. 4.10, using the same thermodynamic databases as previously.[49] A closer inspection of the p_{O_2} data reveals that α-Al_2O_3 is the most stable oxide (also compared to other modifications of the same oxide), followed by $NaAlSiO_4$ and Cr_2O_3. This is in good agreement with the experimental observations. All these phases form at oxygen partial pressures that are orders of magnitude lower than those existing at the surface or in the bulk gas phase. In contrast, nickel will be present in a pure metallic form at the surface, as NiO is not stable at these partial pressures. Note that carbides are prevented from forming within the porous reaction layer, because they are always thermodynamically less stable than their oxide counterparts.[36, 52, 53] Therefore, all chromium carbides, which are in direct contact with the gas phase at the surface, will immediately be oxidised to Cr_2O_3, in agreement with the observations in Fig. 4.9.

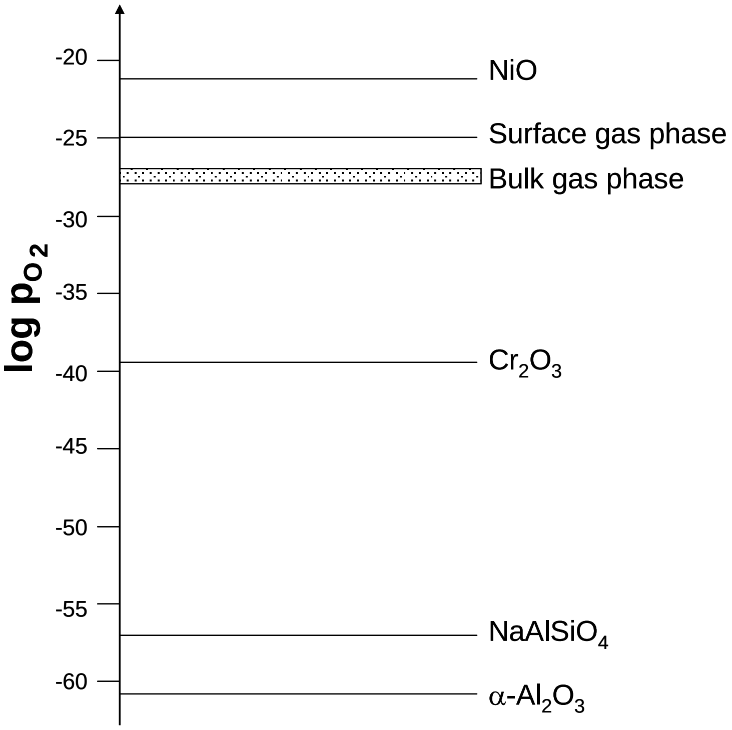

Figure 4.10 Calculated equilibrium oxygen partial pressures for formation of α-Al_2O_3, $NaAlSiO_4$, Cr_2O_3 and NiO at 540°C. The corresponding ranges in p_{O_2} at the surface and in the bulk gas phase are included for comparison.

Finally, based on the thermodynamic data summarised in Fig. 4.10 two semi-quantitative diagrams have been constructed, showing the pertinent carbon activity and oxygen partial pressure gradients across the entire surface region at 540°C and steady state in the presence of solid carbon. As indicated in Fig. 4.11 (a), the carbon activity is about 100 in the bulk gas phase and drops to a valued close to unity within the porous reaction layer in contact with the coke. At this stage of the surface degradation process the dense α-Al_2O_3 layer at the inner surface provides an effective getter for further carbon intrusion into the alloys, suggesting that a_C abruptly drops to a value of about 10^{-6} on the inside, where α-Cr is a stable phase. This carbon activity is large enough to stabilise the parent $M_{23}C_6$ phase within alloy 602 at 540°C (requires that $a_C > 2\text{x}10^{-7}$), without contributing to the formation of the higher order Cr_7C_3 carbide. The latter condition implies that $a_C < 5\text{x}10^{-6}$ in the present case.

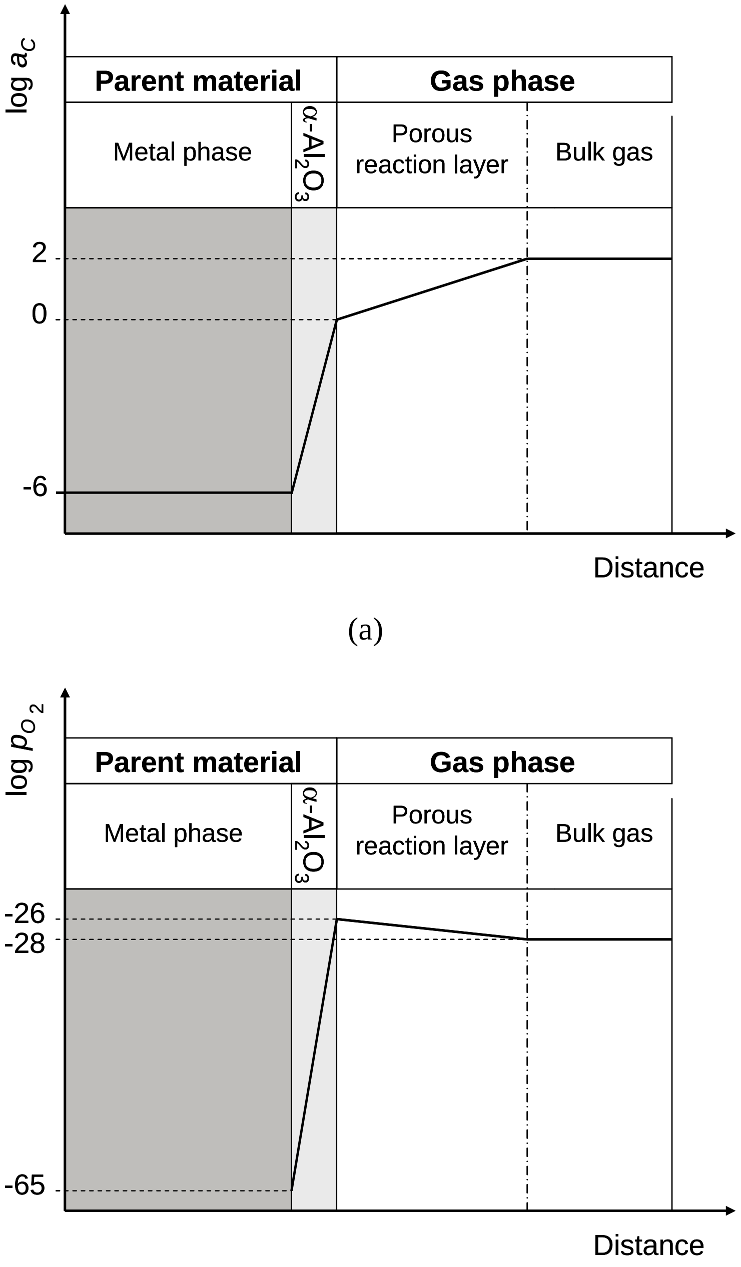
log a_C
Parent material
Gas phase
Metal phase
α-Al2O3
Porous reaction layer
Bulk gas
2
0
-6
Distance
log p_{O_2}
Parent material
Gas phase
Metal phase
α-Al2O3
Porous reaction layer
Bulk gas
-26
-28
-65
Distance

(a)

(b)

Figure 4.11 Semi-quantitative diagrams showing the carbon activity and oxygen partial pressure gradients across the entire surface region at 540°C and steady state; (a) The a_C gradient, (b) The p_{O_2} gradient.

The corresponding p_{O_2} profile is shown in Fig. 4.11 (b). In this case the oxygen partial pressure is highest at the surface, meaning that there will be a flux of oxygen diffusing through the porous reaction layer and into the bulk gas phase, in agreement with equation (4.2). Growth of the protective Al_2O_3 layer will then proceed, either by diffusion of oxygen ions through the alumina lattice towards the oxide/metal interface or by diffusion of aluminium ions from the inside and through the lattice where it reacts with oxygen in the gas phase on the outside. From what is already known in the literature about the growth kinetics of α-Al_2O_3, the former mechanism is perhaps the most probable one.

The kinetics of oxide formation will be further elaborated and discussed in Part V of the present thesis.

4.5. Conclusions

The basic conclusions that can be drawn from this investigation are as follows:

- In general, the chemical and structural changes taking place within the surface-near regions of the exposed nickel-based alloys 602 and 693 can only be understood by considering the reaction kinetics involved. In the present plant exposed trials involving processing of syngas, the local chemical composition is controlled by a complex transport mechanism. This includes bulk diffusion of Cr and Al in the metal phase and mass transfer of gaseous species across the porous reaction layer at the surface.

- The bulk process gas, containing the components CO, H_2, CO_2, H_2O and CH_4, is characterised by a high carbon activity ($a_c \approx 100$) and a low oxidising potential. However, when the Boudouard reaction ($2CO = C + CO_2$) is released and coke deposition occurs at the surface, the carbon activity immediately drops to a value close to unity, leading to a corresponding shift in the CO_2/CO ratio and an increase in the oxygen partial pressure. The latter condition favours oxide formation. This essentially means that the surface disintegration proceeds by gradual oxidation of the Al and Cr, which are the key elements in alloys 602 and 693.

- As long as the original surface oxide layer is not seriously damaged or degenerated by deposition reactions, both alloys exhibit a high intrinsic resistance to metal dusting corrosion. However, the resistance to metal dusting corrosion gradually decreases as the surface disintegration proceeds, and after 2 years of plant exposure a few corrosion pits can be observed at the surface of the alloys. After 4 years of exposure the attack is nearly uniform in the case of alloy 602, whereas alloy 693 is more reluctant to pit formation. This observed difference in the incubation time for metal dusting corrosion reflects the pertinent variations in the Al and Cr contents between the two alloys.

- A comparison between steam oxidised specimens and plant exposed alloys shows that both conditions favour the formation of an outer layer of Cr_2O_3 and an inner layer of α-Al_2O_3 at the surface. The oxidation is accompanied by Cr and Al depletion of the surface-near austenite, leaving behind nanometer-sized nickel- and iron-rich particles in-between the oxides. After 2 years of plant exposure, these are too small to be detected by synchrotron X-ray diffraction. The alumina layer is very dense and provides an effective getter against carbon intrusion into the bulk of the alloys. Therefore, the material below the protective α-Al_2O_3 layer is essentially unaffected by the process gas, even in cases where the outer oxide layer has cracked.

- In addition, the syngas contains impurity elements such as Ni, Si and Na at the ppb level, which are brought to the metal surface by the gas stream. The nickel particles tend to deposit on the alloy surfaces, where they contribute to coke formation by catalysing the Boudouard reaction. In contrast, the elements Si and Na react with α-Al_2O_3 or excess aluminium to form nepheline ($NaAlSiO_4$). The hexagonal nepheline crystals grow outwards from the alumina layer towards the process gas. At present, it cannot be stated with certainty whether the nepheline formation is harmful to corrosion properties by destroying the protective α-Al_2O_3 layer.

- Moreover, it has been verified that the materials themselves are not fully resistant to tempering at 540ºC because partitioning of the original austenitic lattice into α-Cr and γ-Ni (with Fe in solid solution) may occur. In alloy 602 the partitioning is restricted to a, say, 20μm thin layer adjacent to the surface. In contrast, the entire bulk region of the Cr-rich alloy 693 is seen to be covered by the characteristic lamella α-Cr transformation product after some hundred hours of tempering at 540ºC, thus making this experimental material unsuitable for high temperature applications.

- Finally, series of thermodynamic calculations have been carried out to rationalise the observed phase distribution across the entire surface region of the 2 years plant exposed alloys. In general, the constituent phases detected by synchrotron X-ray diffraction are consistent with those predicted by the thermodynamic model. This model allows for the existence of local equilibria at the surface in the presence of solid carbon and suggests that the carbon deposition occurring during exposure is controlled by a complex diffusion mechanism involving mass transfer of gaseous species across a stagnant boundary layer at the surface.

4.6. References

1. P. R. Roberge: *Handbook of Corrosion Engineering*, 1'st ed., McGraw-Hill, New York, 2000.
2. D. J. Tillack, J. E. Guthrie, "*Wrought and cast heat-resistant stainless steels and nickel alloys for the refining and petrochemical industries*", in NiDI Technical Series, Report No.10071, Nickel Development Institute, Birmingham, England, 1998.
3. P. Elliott: *Materials and Design*, 1991, No.6, vol. 12, pp. 299-307.
4. D. Woodford, "*Accelerated high temperature performance evaluation for alloy optimization, embrittlement, and life assessment*", paper presented at Corrosion/2005, Houston, Texas, USA, 3.-7.April 2005, NACE International, Houston, Texas, USA.
5. F. Tancret, H. K. D. H. Bhadeshia, D. J. C. MacKay: *Materials Science and Technology*, 2003, No.3, vol. 19, pp. 283-290.
6. D. C. Agarwal, U. Brill, "*Performance of alloy 602CA in high temperature environments up to 1200ºC (2200ºF)*", paper presented at Corrosion/2000, Orlando, Florida, USA, 26.-31.March 2000, NACE International, Houston, Texas, USA.
7. H. Stahl, S. Gyde Thomsen: *Ammonia plant safety (and related facilities)*, 1996, vol.36, pp. 180-191.
8. R. F. Hochman, J. H. Burson: *American Petroleum Institute Division of Refining Proceedings*, 1966, vol. 46, pp. 331-344.
9. H. J. Grabke, E. M. Müller-Lorenz, B. Eltester, M. Lucas: *Materials at high temperatures*, 2000, No.2, vol. 17, pp. 339-345.
10. B. Schmid: "*Microscale examination of metal dusting corrosion in steels and in-situ observations of high temperature oxidation of metals*", PhD Thesis, NTNU - Norwegian University of Science and Technology, Department of Materials Technology and Electrochemistry, Trondheim, 2000.
11. Z. Zeng, K. Natesan, V. A. Maroni: *Oxidation of metals*, 2002, No.1-2, vol. 58, pp. 147-170.
12. C. M. Chun, T. A. Ramanarayanan: *Oxidation of metals*, 2004, No.1-2, vol. 62, pp. 71-92.
13. P. Szakálos: "*Mechanisms of Metal Dusting*", PhD Thesis, KTH - Royal Institute of Technology, Department of Materials Science and Engineering, Stockholm, 2004.
14. H. J. Grabke, R. Krajak, J. C. Nava Paz: *Corrosion Science*, 1993, No.5-8, vol. 35, pp. 1141-1150.

15. F. Di Gabriele, F. H. Stott, Z. Liu: *Materials Science Forum*, 2004, No.1, vol. 461, pp. 545-552.
16. B. Schmid, Ø. Grong, R. Ødegård: *Materials and Corrosion*, 1999, No.11, vol. 50, pp. 647-653.
17. H. J. De Bruyn, E. H. Edwin, S. Brendryen, "*Apparent influence of steam on metal dusting*", paper presented at Corrosion/2001, Houston, Texas, USA, 11.-16.March 2001, NACE International, Houston, Texas, USA.
18. P. Szakálos, R. Pettersson, S. Hertzman: *Corrosion Science*, 2002, No.10, vol. 44, pp. 2253-2270.
19. F. Eberle, R. D. Wylie: *Corrosion*, 1959, No.12, vol. 15, pp. 622t-626t.
20. M. L. Holland, H. J. De Bruyn: *International Journal of Pressure Vessels and Piping*, 1996, No.1-3, vol. 66, pp. 125-133.
21. H. J. Grabke, M. Spiegel: *Materials and Corrosion*, 2003, No.10, vol. 54, pp. 799-804.
22. S. Strauss, H. J. Grabke: *Materials and Corrosion*, 1998, No.5, vol. 49, pp. 321-327.
23. D. C. Agarwal, L. Stewart, M. McAllister, "*Alloy 602CA (UNSNO6025) solves pig tail corrosion problems in refineries*", paper presented at Corrosion/2003, San Diego, California, USA, 16-20 March 2003, NACE International, Houston, Texas, USA.
24. R. Kirchheiner, D. J. Young, P. Becker, R. N. Durham, "*Improved Oxidation and Coking Resistance of a New Alumina Forming Alloy 60 HT for the Petrochemical Industry*", paper presented at Corrosion/2005, Houston, Texas, USA, 3.-7.April 2005, NACE International, Houston, Texas, USA.
25. H. J. Grabke, H. P. Martinz, E. M. Müller-Lorenz: *Materials and Corrosion,* 2003, No.11, vol. 54, pp. 860-863.
26. B. A. Baker, G. D. Smith, S. A. McCoy: *Ammonia plant safety (and related facilities),* 2002, vol.42, pp. 257-267.
27. A. T. W. Kempen, J. C. Wortel: *Materials and Corrosion*, 2004, No.4, vol. 55, pp. 249-258.
28. F. D. Gabriele, J. R. Bernstein, M. M. Al-Qhatani, Z. Liu, M. P. Jordan, J. A. Richardson, F. H. Stott: *Materials and Corrosion*, 2003, No.11, vol. 54, pp. 854-859.
29. A. S. Khanna: *Introduction to high temperature oxidation and corrosion*, 1'st ed., ASM International, Materials Park, Ohio, 2002.

30. H. J. De Bruyn, B. Schmid, Ø. Grong, J. Z. Albertsen, "*Adapting metal dusting research to trends in syngas technology*", paper presented at Corrosion/2005, Houston, Texas, USA, 3.-7.April 2005, NACE International, Houston, Texas, USA.
31. J. Z. Albertsen: Part III of the present thesis.
32. J. Z. Albertsen: Part V of the present thesis.
33. F. Tancret, H. K. D. H. Bhadeshia: *Materials Science and Technology*, 2003, No.3, vol. 19, pp. 291-295.
34. T. B. Massalski: *Binary alloy phase diagrams*, 1'st ed., American Society for Metals, Metals Park, Ohio, 1986.
35. D. A. Porter, K. E. Easterling: *Phase Transformations in Metals and Alloys*, 2'nd ed., Chapman & Hall, London, 1992.
36. M. Hänsel, C. A. Boddington, D. J. Young: *Corrosion Science*, 2003, vol.45, pp. 967-981.
37. O. V. D. Biest, J. M. Harrison, J. F. Norton: paper presented at The International Conference of the Behaviour of High Temperature Alloys in Aggressive Environments, Petten, The Netherlands, 15.-18. October, 1979, Ed.I. Kirman, The Metals Society, pp. 681-703
38. R. F. Hochman: in *Proceedings of the 3'rd International Congress on Metallic Corrosion (1966)*, University of Moscow Press, Moscow, Russia, 1969, pp. 119-133.
39. R. G. Olsson, E. T. Turkdogan: *Metallurgical Transactions*, 1974, No.1, vol. 5, pp. 21-26.
40. G. A. Jablonski, A. Geurts, J. Sacco, R. R. Biederman: *Carbon*, 1992, No.1, vol. 30, pp. 87-98.
41. P. Szakálos: *Materials and Corrosion*, 2003, No.10, vol. 54, pp. 756-762.
42. H. J. Grabke: *Corrosion*, 1995, No.9, vol. 51, pp. 711-720.
43. R. Yin: *Oxidation of metals*, 2003, No.1/2, vol. 60, pp. 103-116.
44. Q. Wei, E. Pippel, J. Woltersdorf, H. J. Grabke: *Materials and Corrosion*, 1999, No.11, vol. 50, pp. 628-633.
45. J. C. Nava Paz, H. J. Grabke: *Oxidation of metals*, 1993, No.5-6, vol. 39, pp. 437-456.
46. E. Pippel, J. Woltersdorf, R. Schneider: *Materials and Corrosion*, 1998, No.5, vol. 49, pp. 309-316.
47. C. M. Chun, T. A. Ramanarayanan, J. D. Mumford: *Materials and Corrosion*, 1999, vol. 50, pp. 634-639.
48. FactSage: www.factsage.com, 2005.

49. CRCT-ThermFact-Inc, GTT-Technologies: FACT 53. Compound Database, 2005.

50. T. Rosenqvist: *Principles of extractive metallurgy,* 2'nd ed., McGraw-Hill International Book Company, Singapore, 1983.

51. J. Szekely, N. J. Themelis: *Rate phenomena in process metallurgy,* 1'st ed., Wiley-Interscience, New York, 1971.

52. O. Kubaschewski, C. B. Alcock: *Metallurgical thermochemistry*, 5'th ed., Pergamon Press, Oxford, 1979.

53. R. Petkovic-Luton, T. A. Ramanarayanan: *Oxidation of metals*, 1990, No.5-6, vol. 34, pp. 381-400.

APPENDIX I S-XRD results and FEG SEM images of the iron-based alloy APMT

The main results from the Synchrotron XRD analyses are summarised in Table A1, which shows data from the unexposed, 2 years and 4 years plant exposed samples, respectively. Figure A1 shows FEG SEM backscattered images of alloy APMT after 4 years of plant exposure.

Table A1 Refined results of phases detected by S-XRD experiments in unexposed, 2 years and 4 years plant exposed samples of the APMT alloy. X-ray signals were extracted from a depth 6-13μm below the surface. Numbers in parantheses indicate standard deviation of the experiments.

Phase	Ferrite	γ-Ni	Nepheline	Corundum
Lattice	BCC	FCC	Hexagonal	Trigonal
Space group	Fm3m	Im3m	P63	R3C
Unexposed	*a*= 2.8939(1)Å 100 vol%			
2 years exposure	*a*= 2.8869(1)Å 67.2 vol%	*a*= 3.5385(1)Å 21.7 vol%	*a*= 9.9884(3)Å *c*= 8.3671(4)Å 5.5 vol%	*a*= 4.7652(2)Å *c*= 13.017(1)Å 5.6 vol%
4 years exposure	*a*= 2.8868(1)Å 59.7 vol%	*a*= 3.5346(1)Å 33.8 vol%	*a*= 9.9852(3)Å *c*= 8.3633(4)Å 2.4 vol%	*a*= 4.7651(2)Å *c*= 13.017(1)Å 4.1 vol%

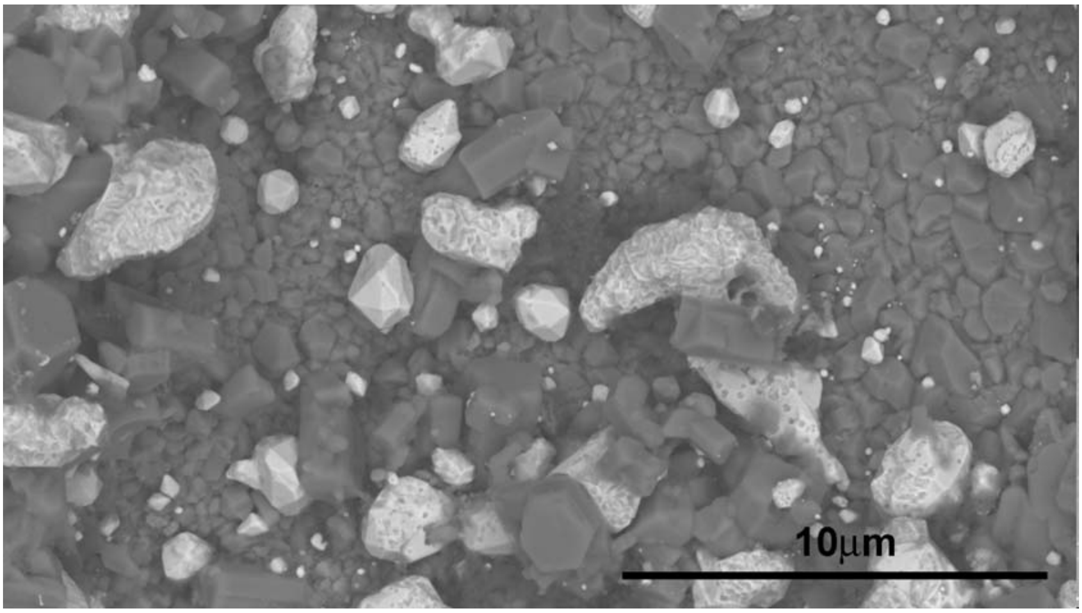

(a)

Figure A1 FEG SEM backscattered images of the iron-based alloy APMT exposed to a syngas environment for 4 years at 540ºC. (a) Ni-crystallites observed at the surface of the alloy, (b) Cross section image.

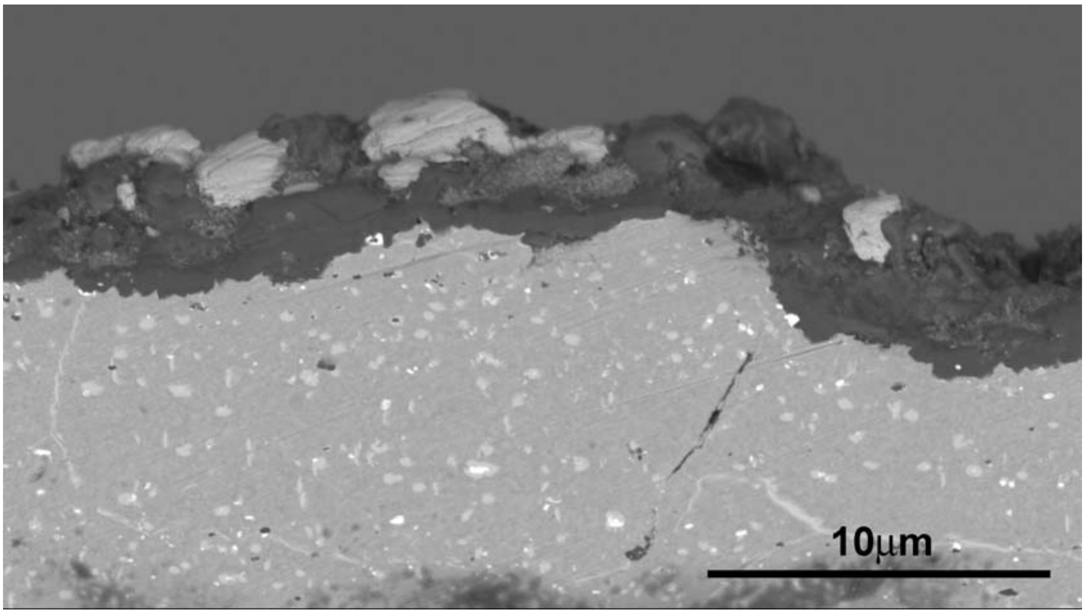

(b)

Figure A1 Continued.

Gas-metal interactions during plant exposure lead to the formation of γ-Ni, nepheline and corundum at the surface of the alloys. The nickel, appearing bright due to backscattered image contrast in Figure A1, stem from the nickel catalyst being used upstream in the process, whereas nepheline forms due to presence of the trace elements Na and SiO(g) at the ppb level in the syngas. No metal dusting pits were observed at the surface after 4 years of plant exposure. In general, the S-XRD results in Table A.1 show that minor changes occurred from 2 to 4 years of plant exposure. This indicates that the alloy is relatively stable under the prevailing circumstances.

PART V

A model for metal dusting corrosion in nickel-based alloys involving internal precipitation of carbides, oxides and graphite

5.1. Introduction

The term metal dusting is commonly used to describe metal deterioration at high temperatures (400-800ºC) which occurs during exposure to gas atmospheres containing H_2, CO, CO_2, H_2O and hydrocarbons.[1, 2] Both iron-, cobalt- and nickel-based alloys are prone to metal dusting and usually the corrosion attack results in pitting and general metal loss, where the individual pits often merge to cause uniform metal wastage.[3] The early stages of attack are characterised by the formation of hemispherical pits containing a powdery mixture of carbides, oxides, carbon soot and metal particles. At the same time heavily carburised metal is observed beneath the pitted areas.[4] The phenomenon of metal dusting was first documented by Pattinson[5] in 1876, and similar exploratory reports were later published in 1945[6], 1947[7] and 1959.[8-10] In 1966 Hochman and Burson[11] studied the corrosion mechanism in more detail and laid the foundation for the current understanding of the phenomenon. Over the years a number of researchers have contributed significantly to the development of the field,[12-35] but metal dusting corrosion is still a controversial research topic in the sense that the degradation mechanisms involved are not yet fully understood.

In a real plant exposure situation involving metal dusting, a number of variables come into play which cannot readily be accounted for in a mathematical simulation of the corrosion process, e.g. alloy and gas composition, temperature, ambient pressure, exposure time, gas flow rate and possible cyclic temperature variations.[33] In the past the gas phase has mainly been characterised by its carbon activity, a_c,[2, 13, 35-38] which is a measure of the carburising potential of the bulk gas. Provided that a_c is sufficiently high, carbon will start to deposit on the metal surface according to the Boudouard reaction $2CO = C + CO_2$. This carbon formation, which is released by a catalytic reaction, is normally considered to be a precondition for initiation of uniform metal dusting corrosion.[34] But as soon as carbon/graphite appears on the metal surface, the carbon activity drops towards unity by definition. Thus, after the Boudouard reaction has been triggered, the metal dusting corrosion process proceeds in the presence of both a carbon activity gradient and an opposite directed oxygen partial pressure gradient, as determined by local chemical equilibria at the gas/metal interface.[39] This suggests that a complex transport mechanism is operative during the steady state part of the degradation process, which also involves counter diffusion of molecular species across the boundary layer or the reaction zone established at the surface.[39] However, since the alloy often is protected by a stable surface oxide layer,[40, 41] the accompanying carbon penetration into the bulk of the material with consequent carbide formation must occur by diffusion through already existing pores or cracks in the oxide.[42] Therefore, in order to prevent subsequent carbide formation a certain amount of oxidation is needed to maintain or restore the protective oxide layer, which, in turn, requires diffusion of oxygen and oxide forming species towards the metal surface.[43, 44] But oxygen can also be responsible for the actual surface degradation leading to the metal dusting corrosion attacks.[20, 24, 39, 45] For example, it has been argued that high local stresses will build-up in the surface near regions of the exposed alloy when the metal carbides are converted into oxides in the root of the pits due to interactions with the process gas.[21, 39, 46] The stress build-up occurs because of the pertinent volume expansion accompanying the subsequent oxidation of the internal carbides.[47] This, together with possible cyclic temperature variations during exposure,[48] eventually leads to the break-up of the protective oxide layer and contributes to further carbon intrusion into the bulk of the material by diffusion. Therefore, some researchers have suggested that metal dusting corrosion in Ni-based alloys occurs by a process of simultaneous internal carburisation and oxidation.[20, 45, 49]

Although aspects of metal dusting corrosion have been extensively investigated and reported in the scientific literature, a verified quantitative understanding of the phenomenon under relevant exposure conditions has not been obtained yet. In particular, it is important to clarify how complex engineering alloys behave during long time exposure to real industrial process gases. Therefore, a multidisciplinary research programme on metal dusting corrosion in various nickel-based alloys during long time exposure to syngas in an industrial plant for methanol production was initiated about five years ago by Statoil. The aim of the project is to study surface degradation and metal dusting corrosion under such severe conditions, since previous investigations have shown that impurity elements like Ni, Si and Na contained in the syngas at the ppb level lead to the formation of various phases at the surface of both Ni-based and Fe-based alloys that are not observed in accelerated laboratory tests (i.e. $NaAlSiO_4$, pure γ-Ni crystallites and α-Cr).[50] In these studies different high resolution experimental techniques are employed, i.e. synchrotron X-ray diffraction in combination with scanning- and transmission electron microscopy, which are complimentary and well suited for the purpose.[33] In Part IV of the thesis previously referred to in the text,[39] the extent of surface degradation occurring prior to the pit formation in the two Ni-based alloys 602 and 693 following 2 years of exposure to syngas at 540ºC has been documented and reported. This part of the thesis, which is a follow-up on the same alloys after 4 years of syngas exposure, details of the pit formation and the resulting carbon intrusion into the bulk of the materials are further highlighted and explored in attempt to disclose the corrosion mechanisms involved under the prevailing circumstances.

5.2. *Experimental*

Part V of the thesis is mainly concerned with the 4 years plant exposed alloys 602 and 693 and the mechanisms of metal dusting corrosion in these materials. The experimental techniques being used include:

- Light microscopy
- Scanning electron microscopy (FEG SEM)
- Microprobe / WDS analyses
- Transmission electron microscopy (TEM/ STEM)
- Synchrotron X-ray diffraction (S-XRD) analyses

Further details are given in Part II of the thesis.

5.3. *Results*

The metal dusting corrosion pits formed after 4 years of plant exposure are shown by the optical micrographs in Fig. 5.1. Since these are close-ups of selected pits, the real difference in corrosion behaviour between the alloys is not highlighted. But previous investigations have disclosed that the metal dusting corrosion attack in alloy 602 is essentially uniform, whereas alloy 693 only reveals a small number of hemispherical pits at the surface.[39] Thus, in order to be able to trace back the location of the different phases detected and explain their chemical and physical origin, the areas being sampled and examined in the investigation are more closely defined in Fig. 5.1. It follows that the dashed horisontal lines indicate the maximum depth from which the X-ray signals in the synchrotron XRD analyses have been extracted. Similarly, the dotted arrows extending through the characteristic white zone of non-etching carbides below the pit and into the bulk of the alloys show the locations of the WDS line-scans performed using the microprobe analyser. Finally, the solid boxes encircling the white zone and the corrosion pit indicate the typical areas being examined in the FEG SEM and STEM/TEM analyses.

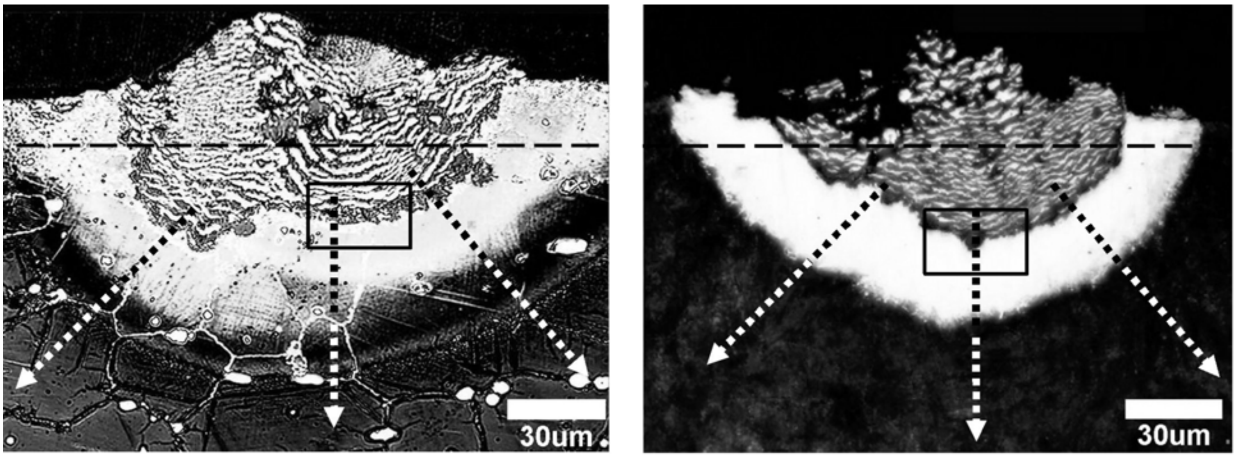

(a) (b)

Figure 5.1 Optical micrographs showing close-ups of the corrosion pits formed at the surface; a) Alloy 602, and b) Alloy 693. Notice that the dashed horizontal lines indicate the maximum depth from which the X-ray signals in the synchrotron XRD analyses have been extracted. Moreover, the dotted arrows show the locations of the WDS line-scans performed using the microprobe analyser, while the solid boxes indicate the typical areas being examined in the FEG SEM and STEM/TEM analyses.

5.3.1. Summary of phases detected by synchrotron XRD

The processed results from the synchrotron XRD analyses are summarised in Table 5.1. In alloy 602, which after 4 years displayed a nearly uniform corrosion attack, the phases detected are representative of those located within the pits and the upper part of the white zone facing the process gas. At the surface above the pits both nepheline ($NaAlSiO_4$) and γ-Ni are present. The nepheline phase forms as a result of reactions with the trace elements Na and Si contained in the process gas, while the deposited γ-Ni crystallites (which are not ordinary corrosion products) stem from the nickel catalyst located upstream in the process.[39] Also oxide phases as Cr_2O_3 and α-Al_2O_3 are detected, along with $M_{23}C_6$ carbide, α-Cr and a solute-depleted parent austenite phase, referred to as Aus_1 in Table 5.1. Whereas the $M_{23}C_6$ carbides probably are the same as those being observed along the grain boundaries of the bulk material in Fig. 5.1 (a), the latter phases are believed to form as a result of partitioning of the parent austenite lattice into α-Cr and Aus_1. This partitioning is probably released by a stress-induced phase transformation occurring at the surface during exposure.[39]

Table 5.1 Summary of phases detected by synchrotron XRD in the 4 years plant exposed alloys. The X-ray signals are extracted from a depth down to approximately 10μm below the surface. Data for the estimated volume fraction of each phase are also provided (in vol%).

Alloy	Metal phases			Carbides		Oxides		
	Aus_1	*Aus_2*	*γ-Ni*[1)] *(Ni-deposit)*	*α-Cr*	$M_{23}C_6$	$NaAlSiO_4$	Cr_2O_3	Al_2O_3
602	66.6%	-	27.9%	2.8%	0.2%	1.3%	0.8%	0.4%
693	16.5%	24.4%	53.4%	-	-	0.4%	4.5%	0.8%

1) Crystallites which stem from the nickel catalyst located upstream in the process.

The situation is even more complex in the case of alloy 693. In this alloy only a few corrosion pits are present at the surface, meaning that the synchrotron XRD signals are mainly extracted from the uncorroded parts of the surface facing the process gas. Referring again to Table 5.1, three metallic phases are observed at the surface, i.e. γ-Ni, Aus_1 and Aus_2 along with the three oxide phases $NaAlSiO_4$, Cr_2O_3 and α-Al_2O_3. Notice that the Aus_2 phase observed in alloy 693 has a lattice parameter that falls between that of the previously mentioned Aus_1 phase and pure γ-Ni.[39] This suggests that it has formed because of extensive depletion of the alloying elements Cr and Fe from the parent austenite lattice. Alternatively, the Aus_2 phase may have formed by absorption of the same alloying elements into the deposited nickel particles coming from the Ni-catalyst, which after 4 years cover most of the gas-exposed metal surface.[39] The latter explanation is perhaps the most probable one, since an increase in the exposure time from 2 to 4 years results in complete removal of the alpha chromium from the surface, as shown by the estimated volume fraction data in Table 5.1. Still, α-Cr is present in abundant amounts in the bulk because alloy 693 (due to its characteristic high Cr and Al contents) undergoes a full phase transformation already after some hundreds of hours of tempering at 540°C, as shown in Part IV of the thesis.

5.3.2. Microprobe analyses of corrosion pits and their surroundings

As shown by the dotted arrows in Fig. 5.1, several line-scans were run across each pit and into the white zone to obtain a representative overview of the element distribution. However, since these measurements did not disclose any evidence of compositional gradients along the periphery of the hemispherical pits, only composition data from the line-scans performed normal to the specimen surface are reported here. Notice that they represent the actual values obtained in the WDS analyses and are not normalised to 100% after the measurements have been made. The results are summarised in Figs. 5.2 and 5.3.

Along the abscissa the position “zero” denotes the boundary between the corrosion pit and the white zone, where negative and positive digits refer to the former and the latter region, respectively. The graphs in Figure 5.2 (a) and 5.3 (a) contain the concentration profiles of the major elements Ni, Cr, Fe and O, whereas the graphs in Figure 5.2 (b) and 5.3 (b) show the minor elements Al and C. The oxygen concentration profiles are also included in the latter plots for comparison with aluminium. In this case the measured oxygen levels can be read from the scale provided along the right ordinate.

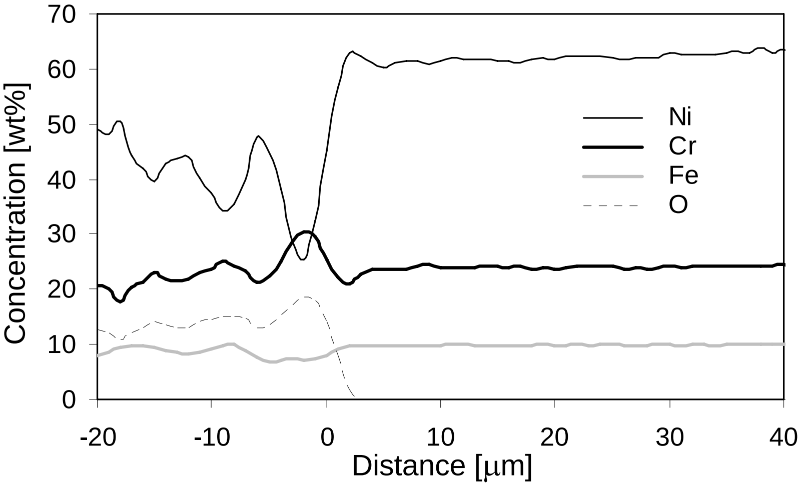

(a)

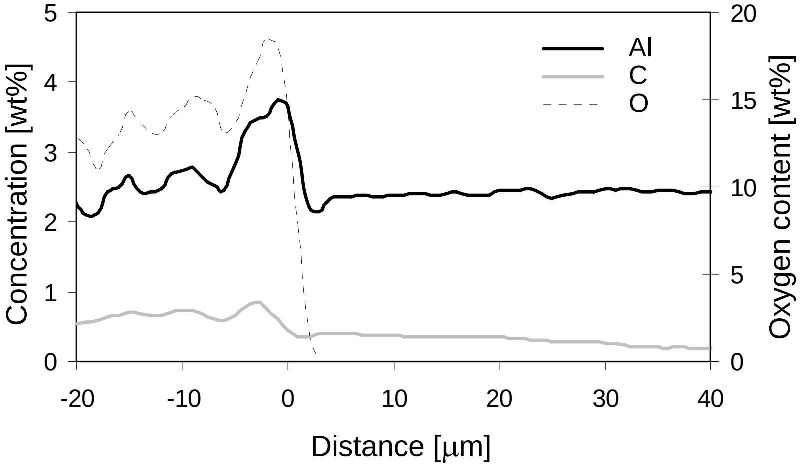

(b)

Figure 5.2 Plots showing measured WDS concentration profiles across a typical corroded area in alloy 602, sampling the bottom part of the corrosion pit, the adjacent white zone and part of the bulk material. The position 0μm denotes the boundary between the corrosion pit and the white zone; a) Measured Ni, Cr, Fe and O concentration profiles, b) Measured Al, C and O concentration profiles.

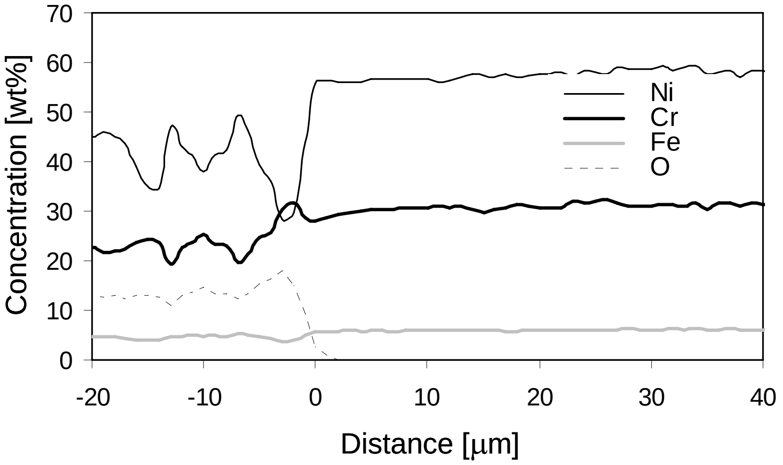

(a)

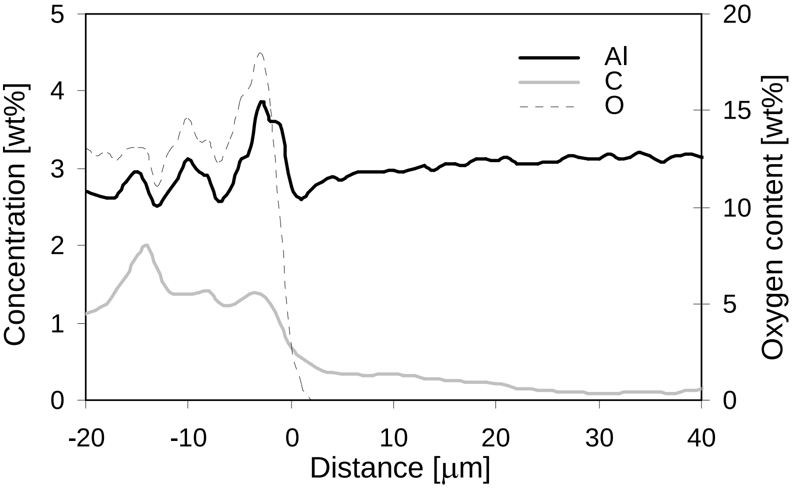

(b)

Figure 5.3 Plots showing measured WDS concentration profiles across a typical corroded area in alloy 693, sampling the bottom part of the corrosion pit, the adjacent white zone and part of the bulk material. The position 0µm denotes the boundary between the corrosion pit and the white zone; a) Measured Ni, Cr, Fe and O concentration profiles, b) Measured Al, C and O concentration profiles.

In general, both alloys reveal the same characteristic element concentration profiles across the entire corroded surface region. The major difference between Figs. 5.2 and 5.3 is the absolute levels of the elements, which is consistent with the compositions seen in Table 2.1 (Part II). Within the white zone, all alloying elements contained in the bulk materials are preserved. Still, there is clear evidence of carbon intrusion in both alloys. This can be seen from the monotonically decreasing carbon concentration profiles across the two white zones in Figs. 5.2 (b) and 5.3 (b). The situation is different within the corrosion pits, where the oxygen content increases rapidly at the expense of Ni as soon as the boundary is crossed. Here both

Cr and Al (and perhaps also some of the iron) are present as oxides, as evidenced by the close match between the measured concentration profiles of the alloying elements and the corresponding oxygen profiles. In contrast, the maxima in the two Ni concentration profiles in Figs. 5.2 and 5.3 appear to be inverted compared to those of the other elements, suggesting that nickel is separated from Cr, Al and O within the corrosion pits and is present in a metallic form together with most of the iron. This is consistent with the observation of a layered pit microstructure in Fig. 5.1. Within the layered microstructure carbon is also deposited, and in alloy 693 the measured carbon level is nearly twice as high as in alloy 602.

5.3.3. FEG SEM analyses of the pit/metal interface

The solid boxes encircling the white zone and the corrosion pits in Fig. 5.1 indicate the typical areas being examined in the FEG SEM analyses. Figures 5.4 and 5.5 show backscattered electron images of the cross section of alloy 602 and 693, along with X-ray maps of the main constituent elements within the same areas.

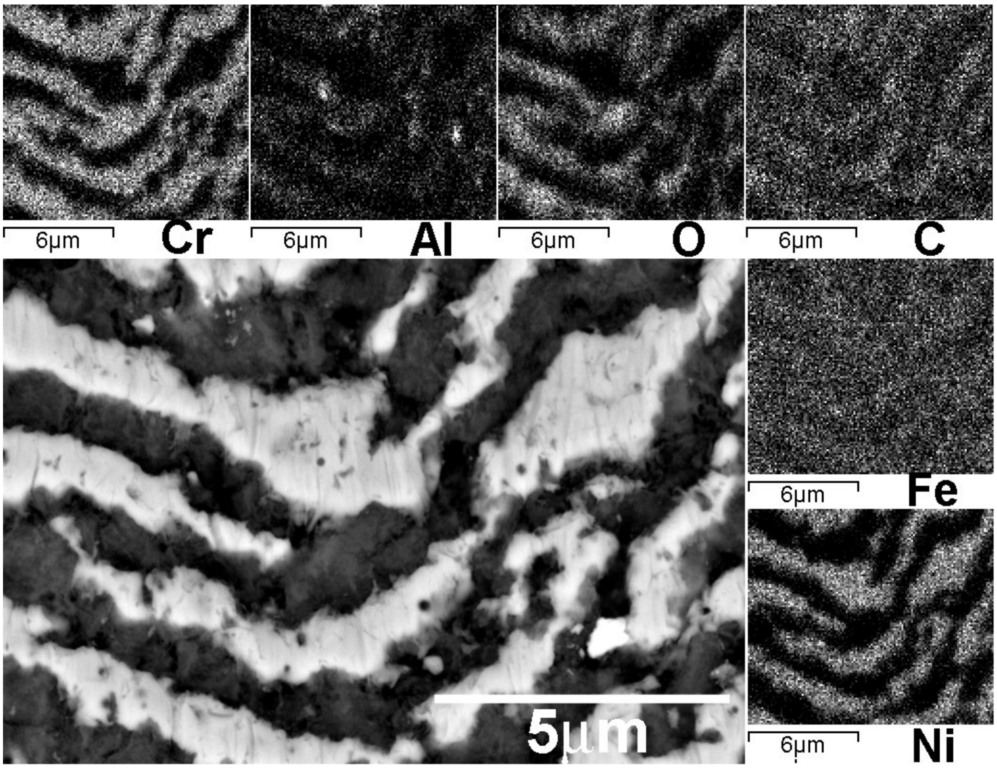

(a)

Figure 5.4 FEG SEM backscattered electron images of the cross section of alloy 602. The smaller images show the corresponding X-ray maps of the main constituent elements from the same surface area; a) The corrosion pit, b) The interface between the corrosion pit and the white zone.

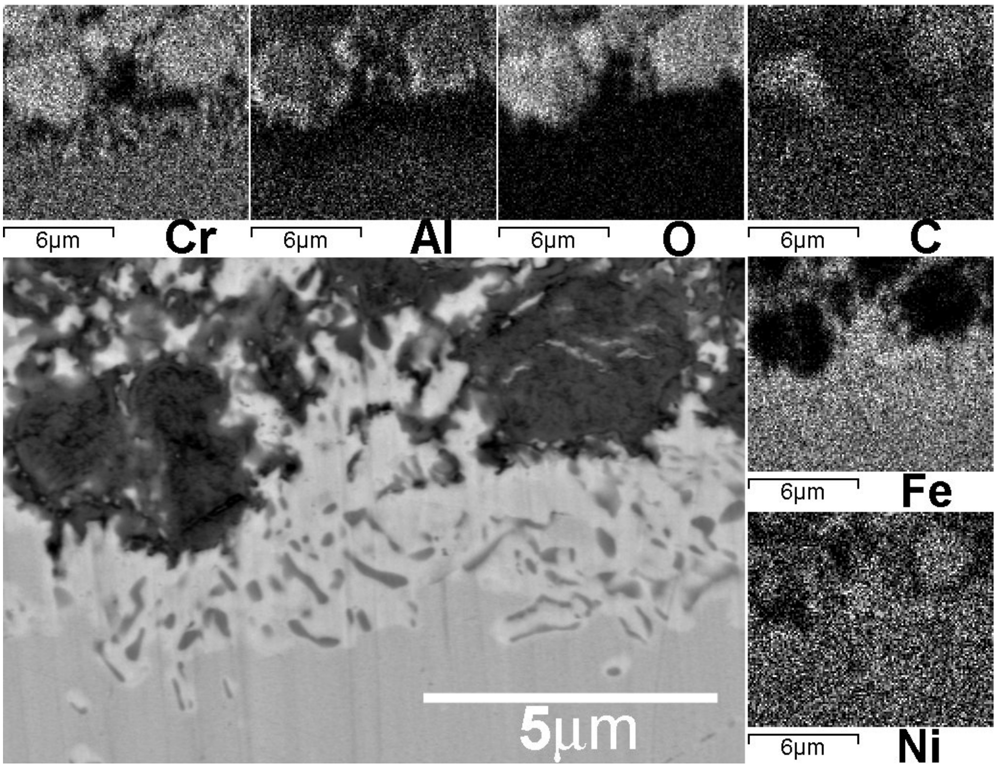
6μm
Cr
6μm
Al
6μm
O
6μm
C
5μm
6μm
Fe
6μm
Ni

(b)

Figure 5.4 Continued.

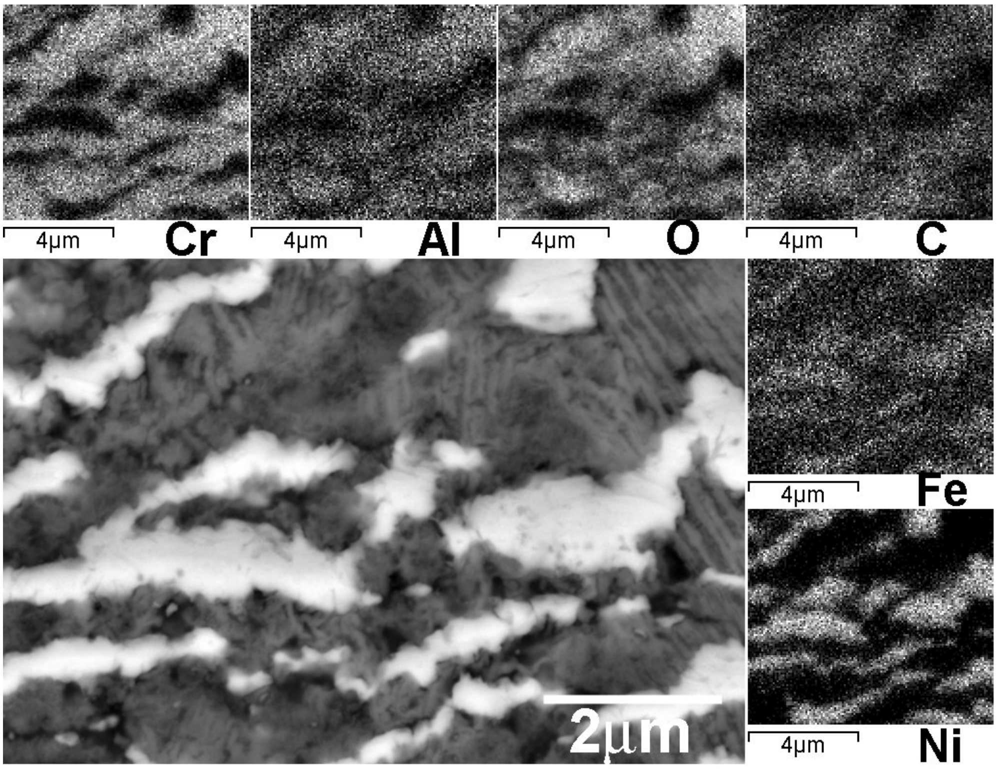
4μm
Cr
4μm
Al
4μm
O
4μm
C
2μm
4μm
Fe
4μm
Ni

(a)

Figure 5.5 FEG SEM backscattered electron images of the cross section of alloy 693. The smaller images show the corresponding X-ray maps of the main constituent elements from the same surface area; a) The corrosion pit, b) The interface between the corrosion pit and the white zone.

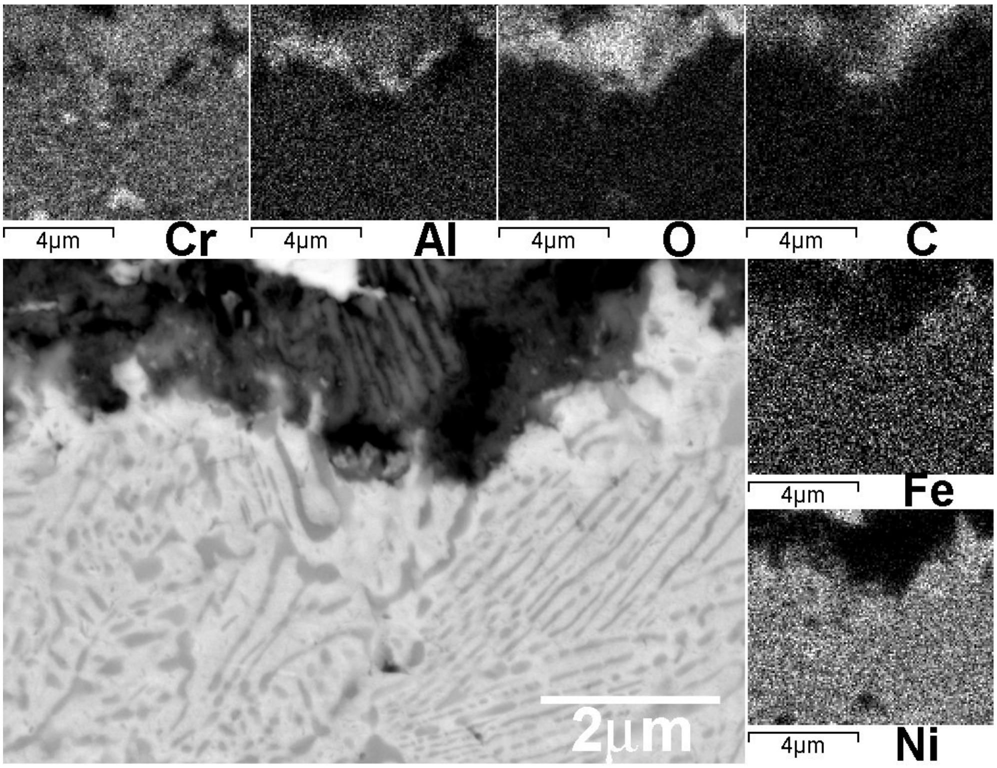

(b)

Figure 5.5 Continued.

A closer inspection of Figs. 5.4 (a) and 5.5 (a) reveals that the element distribution within the corrosion pits of alloys 602 and 693 is similar. In both cases nickel and most of the iron is separated from the other elements, which gives rise to the formation of the characteristic “zebra” pattern in the backscattered electron images. In-between the Ni-Fe rich phases, Cr, Al, O and C are located, forming the dark component of the layered pit microstructure. As judged from the sharpness of the phase contrasts in the backscattered electron images, the average atomic weight of the latter component must be significantly lower than that of Ni and Fe, suggesting that most of the chromium and aluminium are present as oxides. This conclusion is also consistent with the WDS results presented previously in Figs. 5.2 and 5.3, showing peaks in the oxygen level exceeding 15wt%.

Similarly, the backscattered electron images and the corresponding X-ray maps of the adjacent white zones in alloys 602 and 693 facing the bottom part of the corrosion pits are shown in Figs. 5.4 (b) and 5.5 (b), respectively. It follows that the oxygen front is sharp and marks the interface between these two regions. In contrast, chromium appears to be evenly distributed within both regions, whereas the other elements show distributions in accordance with the previous WDS analyses. The observation of a sharp oxygen front at the pit/metal interface is also consistent with the measured oxygen concentration profiles in Figs. 5.2 and 5.3. This means that the EDS oxygen detection is not significantly disturbed by the pertinent overlap in the X-ray spectrum between the $K\alpha$ radiation energy of oxygen (0.526 keV) and the $L\alpha$ radiation energy of chromium (0.573 keV) under the prevailing conditions. Moreover, there is clear evidence of element partitioning/phase formation within the white zone itself, as shown by the distinct phase contrast differences in the backscattered electron images. Although the visible precipitate zone in both alloys is seen to extend several micrometers into the white zone, the resolution of the corresponding X-ray maps is not good enough to capture the observed compositional variations. Therefore, more detailed analyses of the specially prepared FIB samples right at the pit/white zone interface are required to fully characterise the different corrosion microstructures, using transmission electron microscopy.

5.3.4. STEM/TEM analyses of precipitates and corrosion products

Figure 5.6 show a STEM annular dark field image of the FIB sample extracted from alloy 602. In this case the area close to the interface between the corrosion pit and the white zone is sampled. Because the electron transparent FIB sample provides a full 3D representation of the pit/metal interface, the STEM annular dark field image in Fig. 5.6 shows that the oxygen reaction front is rather diffuse and consists of channels penetrating the white zone. These channels are, in turn, filled with reaction products. On the left hand-side of the image, the Cr-Al oxide phases are visible, as indicated by the corresponding X-ray element maps. Within the adjacent white zone, coarse Cr-rich precipitates are observed. These correspond to the precipitates seen previously in the FEG SEM backscattered electron image in Fig. 5.4 (b).

Similarly, Fig. 5.7 shows STEM annular dark field images of the FIB sample extracted from alloy 693. Also in this case it is evident that the pit/metal interface is rather diffuse in the sense that the oxygen reaction front consists of channels penetrating the white zone. In between the oxide/graphite-filled channels, Ni-rich areas containing iron in solid solution are observed. A crack in the oxide layer is also detected, which is seen to be enriched with respect to aluminium. Approximately 4μm deeper into the white zone coarse Cr-rich phases are present. These correspond to the precipitates shown previously in the FEG SEM backscattered electron image in Fig. 5.5 (b).

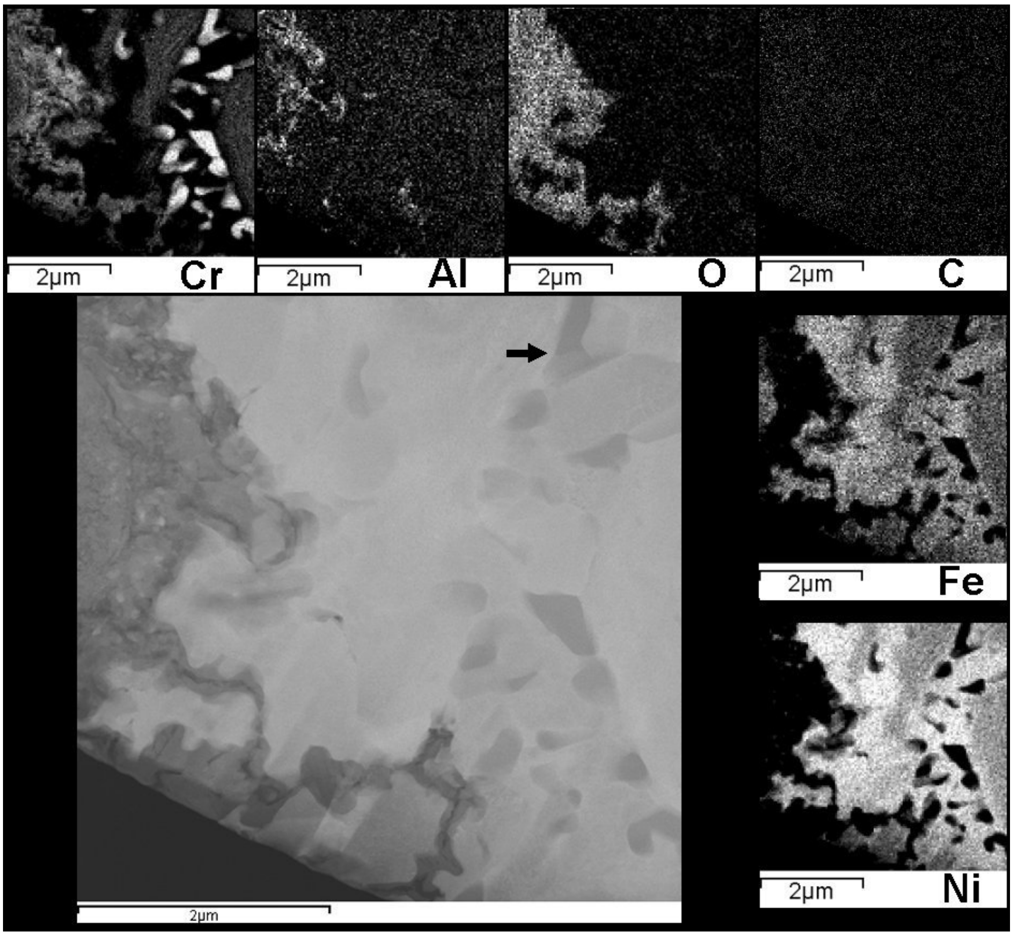

Figure 5.6 STEM annular dark field image of FIB sample extracted from alloy 602, showing the interface between the corrosion pit and the white zone. The smaller images show the corresponding X-ray maps of the main constituent elements from the same areas. The Cr-rich phase referred to in the text is indicated by the arrow in the micrograph.

Because the EDS signal is very insensitive to carbon, diffraction patterns were recorded to confirm that the coarse Cr-containing particles were carbides and to identify their structure. Several particles were examined from each material, and for some of these, diffraction patterns were obtained from more than one orientation. When comparing the patterns with the simulated structures for known carbide phases[51], it was found that they were consistent with the Cr_3C_2 Pnma structure. Also the measured lattice spacings were reasonably consistent with the tabulated unit cell, characterized by a = 5.5329Å, b = 2.8290Å and c = 11.4719Å.[52]

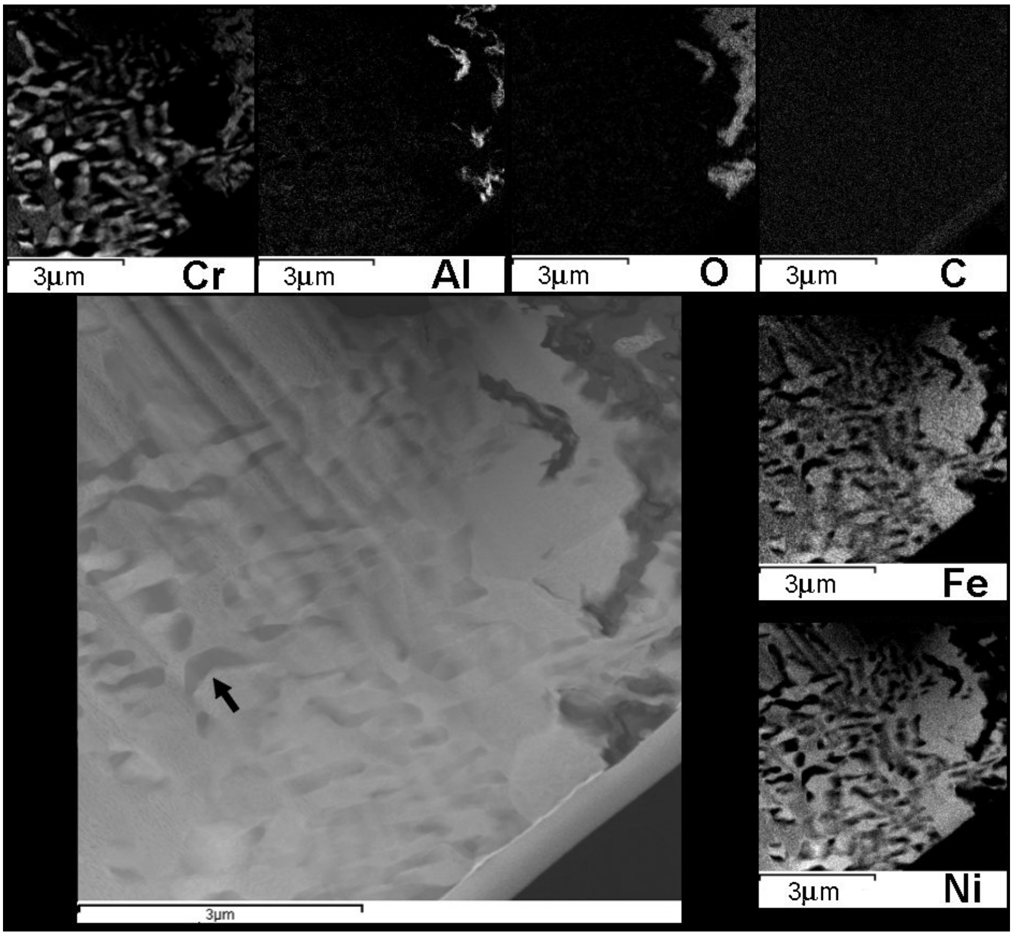

Figure 5.7 STEM annular dark field image of FIB sample extracted from alloy 693, showing the interface between the corrosion pit and the white zone. The smaller images show the corresponding X-ray maps of the main constituent elements from the same areas. The Cr-rich phase referred to in the text is indicated by the arrow in the micrograph.

Figure 5.8 (a) and (b) show examples of the carbides in alloy 602 and 693, respectively. The two carbides can also be located in Figures 5.6 and 5.7, where they are indicated by arrows. Both carbides shown in Figure 5.8 (a) and (b) are oriented along [031] zone axis directions. Figure 5.8 (c) shows selected area diffraction patterns from the [031] and [021] zone axis orientations of the carbide in Figure 5.8 (a). The {001} reflections are forbidden in the crystal structure but are present in both of the diffraction patterns due to double diffraction. Also the {012} reflections present in the [012] zone axis are forbidden but visible due to double diffraction.

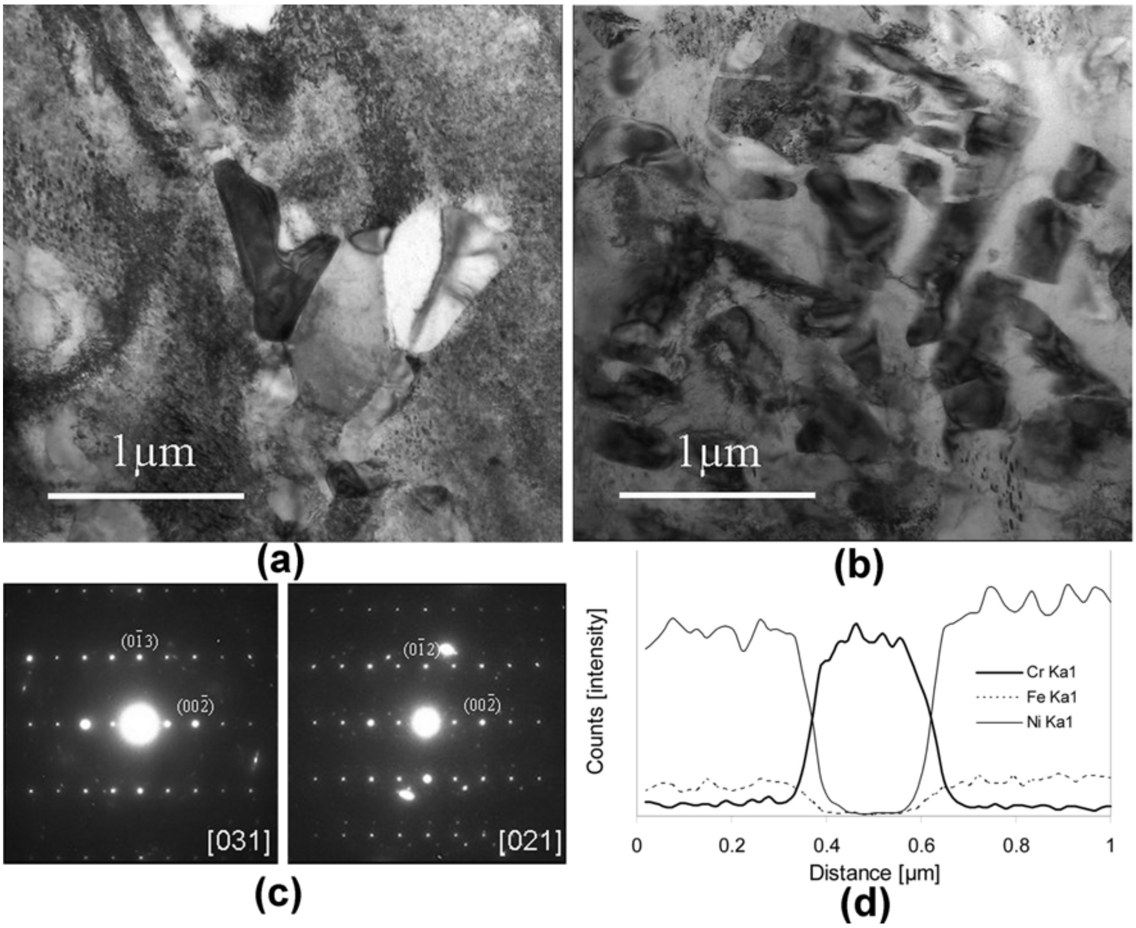

Figure 5.8 TEM investigations of the Cr_3C_2 carbide which form within the white zone a few micrometers away from the pit/white zone interface; (a) Bright field image of a Cr_3C_2 carbide in alloy 602, (b) Bright field image of the Cr_3C_2 carbides in alloy 693, (c) Selected area diffraction patterns of the carbide in (a) from the [031] and the [021] zone axis orientations, (d) Linescan data extracted from the mapping data across the carbide shown in (b).

While Cr is known to be a primary carbide former, some carbide phases may contain significant levels of other metals as well.[53] However, the EDS maps of Figs. 5.6 and 5.7 suggest that the carbides in alloys 602 and 693 contain only Cr as the metallic component. This is indicated more quantitatively in Figure 5.8 (d), which shows a linescan extracted from the mapping data running across the carbide in Figure 5.8 (b). The uncorrected number of counts are shown for the major elements Cr, Fe and Ni, which confirms that the particle is essentially a pure Cr carbide and that the level of Cr in the surrounding matrix is extremely low due to solute depletion.

5.4. Discussion

The main symbols, formulae and units used throughout the paper are defined in Appendix II.

In the following attempts will be made to rationalise the observed metal dusting corrosion behaviour by exploring the thermodynamics of the system and the pertinent rate phenomena involved.

5.4.1. Incubation time for metal dusting corrosion

It has previously been documented in Part IV of the thesis that both alloys are resistant against metal dusting corrosion as long as the inner aluminium oxide layer is intact and provides an effective barrier against carbon intrusion into the bulk of the materials. In alloy 602 the corrosion pits start to form at the surface after about 2 years of gas exposure, whereas the incubation time in alloy 693 is much longer and close to 4 years under the prevailing conditions. This difference in incubation time is not fortuitous, but reflects the pertinent variations in the Al and Cr contents between the two alloys and how a damaged Cr_2O_3 - Al_2O_3 surface oxide layer can be healed through diffusion by allowing new oxide to form from beneath.

As a starting point, simple diffusion calculations will be carried out to estimate the extent of oxide growth occurring after 2 and 4 years of gas exposure, respectively. Provided that the rate controlling step is diffusion of Al and Cr in the bulk austenite phase (thereby neglecting possible effects of high-diffusivity paths on the kinetics), the following analytical solution of Fick's 2nd law applies for the uniaxial case at constant temperature.[54]

$$\kappa_1 = \frac{C(x,t) - C_i}{C_0 - C_i} = erf\left(\frac{x}{\sqrt{4 D_X\, t}}\right) \tag{5.1}$$

where x is the depth beneath the slab surface, D_X is the diffusivity of the elements Cr and Al in the austenite lattice, and C_i and C_0 are the concentration of the same elements at the surface and in the bulk, respectively.

Figure 5.9 shows plots of the calculated concentration profiles of Cr and Al in a ternary Ni-20wt%Cr - 2wt%Al alloy at 540ºC following 2 and 4 years of gas exposure, using input data from Table 5.2. It can be seen from Fig. 5.9 that the maximum diffusion distance, x_m, for Al is of the order of 1μm under the prevailing conditions and about 0.5μm in the case of Cr. Moreover, it is evident that an increase in the exposure time from 2 to 4 years has only a marginal effect on x_m, which is a consequence of the underlying assumption of parabolic growth kinetics. Hence, there will eventually be restrictions in the supply of Cr and Al from the bulk phase to the metal surface. This, in turn, makes it difficult to restore the protective surface oxide layer as the degradation process at the surface proceeds and eventually its intrinsic resistance against carbon intrusion is destroyed because of cracking and spalling.[39, 47, 55]

Table 5.2 Summary of bulk diffusion coefficients for Cr, Al and C in a ternary Ni-20wt%Cr-2wt%Al alloy.[56, 57]

Parameters*	Chromium	Aluminium	Carbon
D_0 [m^2/sek]	1.84×10^{-4}	1.35×10^{-12}	1.56×10^{-4}
Q_d [kJ/mol]	278.644	142.130	160.680

* Assumed relationship $D = D_0 \exp\left(-Q_d / RT\right)$

If the calculated concentration profiles in Fig. 5.9 instead are linearised, the maximum diffusion distance, x_m, at which the bulk composition C_0 is reached is approximately given by the relationship;[58]

$$x_m \approx \sqrt{6\, D_X\, t} \tag{5.2}$$

which also is known as the random-walk model for diffusion in the scientific literature.

Based on a simple mass balance it is possible to convert x_m into an equivalent surface oxide layer thickness z_m of composition X_2O_3 (where X denotes either Cr or Al) by assuming a linear concentration profile across the solute-depleted region adjacent to the metal surface. Taking $\Omega_{X_2O_3}$ equal to the molar volume (in m^3/mol) and C_X equal to the molar concentration (in mol/m^3) of the reaction product X_2O_3 and element X in the alloy, we get:

$$z_m = \frac{1}{4}\, \Omega_{X_2O_3}\, C_X^0\, x_m \tag{5.3}$$

A combination of equations (5.2) and (5.3) then gives:

$$z_m = \frac{1}{4}\, \Omega_{X_2O_3}\, C_X^0 \sqrt{6\, D_X\, t} \tag{5.4}$$

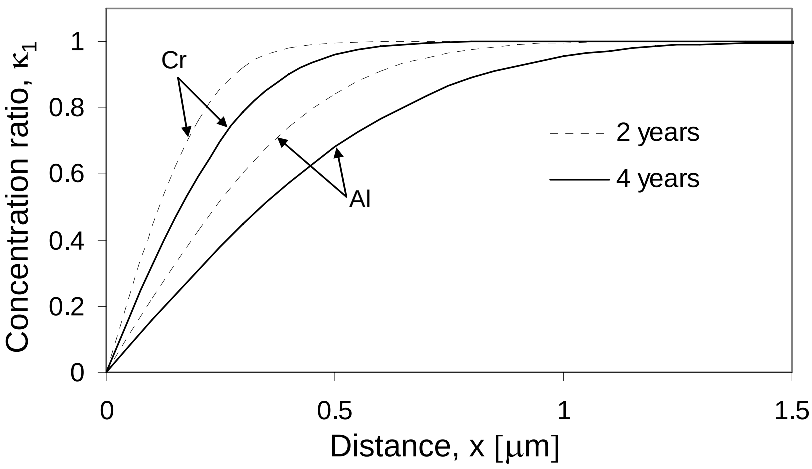

Figure 5.9. Predicted concentration profiles of Cr and Al in regions of a ternary Ni-20wt%Cr-2wt%Al alloy following 2 and 4 years of exposure at 540ºC. The calculations are done using equation (5.1) and input data from Table 5.2.

Figure 5.10 (a) shows a graphical representation of equation (5.4), yielding the evolution of z_m with time for Cr_2O_3 and Al_2O_3 during long time exposure of alloys 602 and 693 at 540ºC. The calculations are done using input data from Tables 2.1 (Part II), 5.2 and 5.3.

Table 5.3 Physical data for some relevant constituent phases. Corresponding data for the parent austenite phase are included for comparison.[47, 59, 60]

Phase	Cr_2O_3	Al_2O_3	$Cr_{23}C_6$	Cr_7C_3	Cr_3C_2	Graphite	Austenite
Molar weight [g/mol]	152	102	1268	400	180	12	57
Density [kg/m^3]	5200	4000	6970	6900	6680	2260	8500

As expected, the growth of the surface oxide layer is seen to be limited by diffusion, and particularly during long time exposure it is difficult to promote new oxide formation. This point is more clearly illustrated in Fig. 5.10 (b), which shows plots of the corresponding oxide growth rates dz_m / dt with time. It follows that the growth rates drop rapidly during the first one to two years because of the pertinent Cr and Al depletion. Hence, small cracks and flaws, which gradually develop in the oxide layer as the surface degradation process proceeds, will not readily be healed by new oxide growing from beneath through bulk diffusion of Cr and Al. Eventually, this results in the break-down of the oxide resistance against carbon intrusion, leading to carbide formation in the interior of the alloys. Still, the predicted growth rates of Cr_2O_3 and Al_2O_3 in alloy 693 are significantly higher than those in alloy 602 because of its resulting higher content of Cr and Al. This may explain why the incubation time for metal dusting corrosion in alloy 693 is nearly 4 years as compared to 2 years in alloy 602, as documented previously in Part IV of the present thesis.

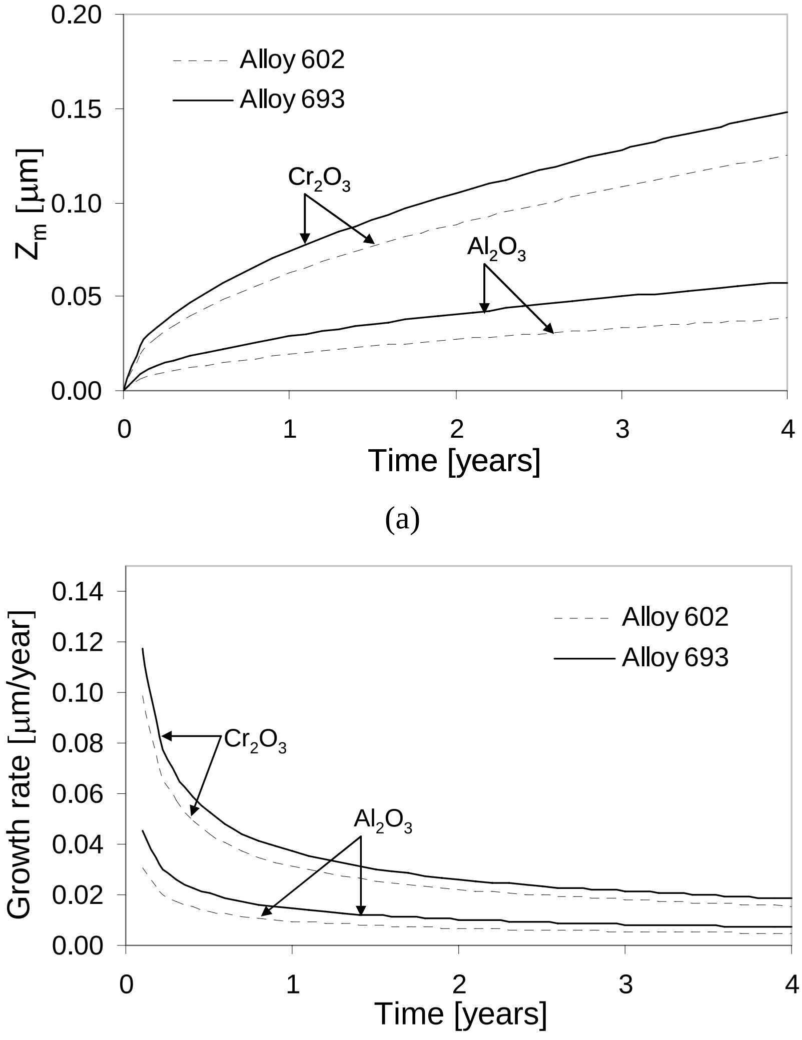

(a)

(b)

Figure 5.10 Predicted change in the surface oxide layer thickness z_m with time for Cr_2O_3 and Al_2O_3, respectively during long-time exposure of alloys 602 and 693 at 540ºC; (a)Plots of the layer thickness z_m versus exposure time (in years), (b) Plots of the growth rate dz_m/dt versus exposure time (in years). The calculations are done using equation (5.4) and input data from Tables 2.1 (Part II), 5.2 and 5.3.

5.4.2. Conditions for oxide formation within the corrosion pits

The WDS results in Figs. 5.2 and 5.3 show that different oxide phases are present within the corrosion pits. The main oxide components are Cr_2O_3 and Al_2O_3, both being stable phases at 540ºC under the prevailing exposure conditions.[39] Moreover, by comparing the peaks of the measured Cr, Al and O concentration profiles with those of Ni, it is obvious that the former elements are separated from Ni. This is readily seen from the characteristic zebra patterns in Figs. 5.4 (a) and 5.5 (a). Still, it is not possible to determine the extent of phase separation from these backscattered electron images and hence the exact chemical compositions of the layered pit microstructures.

In order to unravel further details of the phase compositions within the pits, it is necessary to perform a more in-depth analysis of the WDS data in Figs. 5.2 and 5.3. If all Cr and Al, in the limiting case, are assumed to be present as Cr_2O_3 and Al_2O_3, respectively, the corresponding amount of oxygen bound to these elements (in wt%) is given as:

$$[\%O] = \frac{3}{2}\left(\frac{M_O}{M_{Cr}}[\%Cr] + \frac{M_O}{M_{Al}}[\%Al]\right) \tag{5.5}$$

where M_O, M_{Cr} and M_{Al} are the molar weights of oxygen, chromium and aluminium, respectively.

Thus, by converting the measured concentration profiles for chromium and aluminium in Figs. 5.2 and 5.3 into an equivalent oxygen concentration, via equation (5.5), comparisons can be made between predicted and measured oxygen concentration profiles across the corrosion pits and into the white zone. The results are summarised in Fig. 5.11 (a) and (b) for alloy 602 and 693, respectively.

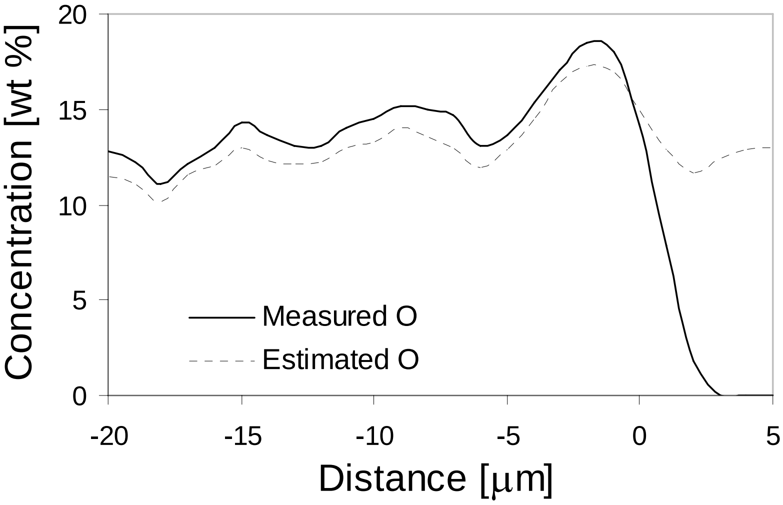

(a)

Figure 5.11 Comparison between measured and predicted oxygen concentration profiles within the corrosion pits, assuming that all Cr and Al are present as Cr_2O_3 and Al_2O_3, respectively. (a) Alloy 602, (b) Alloy 693. The calculations are based on equation (5.5) and data from Figs. 5.2 and 5.3.

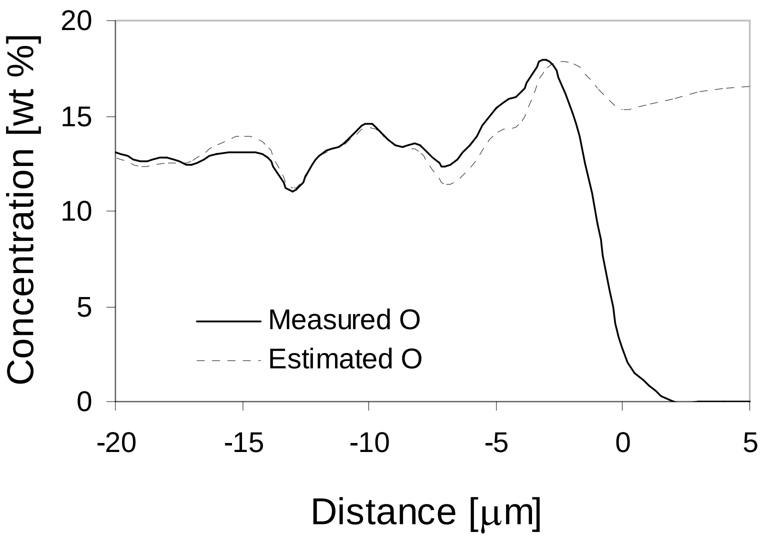

(b)

Figure 5.11 Continued.

It follows that the match between the predicted and measured concentration profiles is surprisingly good in both cases. This means that Cr and Al must be completely separated from Ni (and Fe) within the layered pit microstructure and are present as Cr_2O_3 and Al_2O_3, respectively, with graphite located in-between the oxide/metal lamellae.

5.4.3. Conditions for carbide formation within the white zone

In the following, the conditions for carbide formation within the white zone, as revealed by the optical micrographs in Fig. 5.1, will be examined more in detail. In alloys 602 and 693 the visible white zone is about 30µm thick and forms a continuous band around the pits. Since the white zone contains a high number density of carbides, carbon must have diffused from the outside through cracks in the surface oxide layer and then into the parent Aus_1 phase, where it has reacted with chromium and formed the observed Cr_3C_2 precipitates. In order to explain this carbide formation, some further clarification of the thermodynamics and kinetics involved will be given below.

5.4.3.1. Carbide stability

As a starting point, the commercial software package FactSage[61] is used in combination with dedicated thermodynamic databases[62] to predict the carbon activity (a_c) profile within the white zone at 540ºC and map the corresponding stability ranges of the different carbides, e.g. $Cr_{23}C_6$, Cr_7C_3 and Cr_3C_2. Within the pits themselves, the presence of solid carbon suggests that a_c is close to unity, whereas in alloy 602 the observation of $Cr_{23}C_6$ grain boundary carbides within the bulk phase implies that a_c in the base material is higher than about 2×10^{-7}.[61] The results are presented graphically in Fig. 5.12, which shows a plot of a_c versus position x within the white zone at 540°C, where the stability ranges of the different carbides are superimposed.

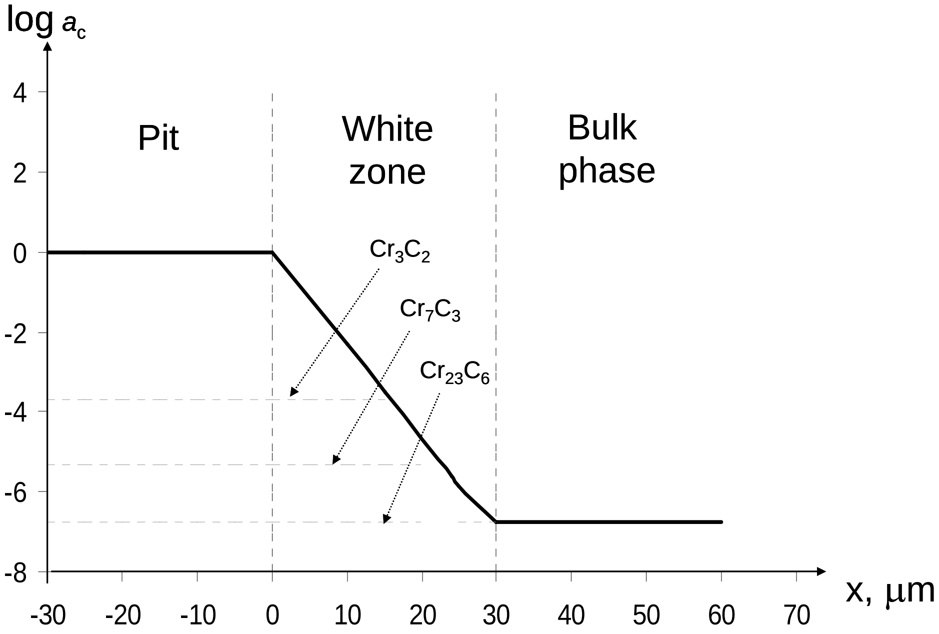

Figure 5.12 Semi-quantitative diagram showing the predicted carbon activity gradient within the white zone of alloy 602 at 540°C. The corresponding stability ranges of the three carbide phases Cr_3C_2, Cr_7C_3 and $Cr_{23}C_6$ are then superimposed on the diagram and indicated by the thin broken lines.

It follows that the chromium carbides, from a thermodynamic point of view, should form within distinct regions of the white zone in the sequence Cr_3C_2, Cr_7C_3 and $Cr_{23}C_6$, depending on the local carburising potential. This predicted reaction sequence is qualitatively consistent with the experimental observations in Figs. 5.6 through 5.8, showing the presence of Cr_3C_2 in alloys 602 and 693 already some few micrometers away from the pit/white zone interface. Also the $Cr_{23}C_6$ carbide is naturally present in alloy 602, both in the unexposed material as well as in the 4 years plant exposed sample, as shown previously by the synchrotron X-ray diffraction data in Table 5.1. In addition, other carbides with a different morphology have been identified within the white zone of alloys 602 and 693, but a more detailed description of these and their distribution will be provided elsewhere.

5.4.3.2. Extent of carbon intrusion

The predicted carbon activity gradient within the white zone creates, in turn, the necessary driving force for carbon diffusion into the bulk of the alloys. Since the process probably involves both lattice diffusion and element transport along high diffusivity paths such as grain boundaries and dislocation cores, it is not possible to fully unravel the mechanisms involved within the scope of the present thesis. Still, it is possible to perform a simplified analysis and provide a conservative estimate of the extent of carbon intrusion, based on the following analytical solution of Fick's 2'nd law.[54]

$$\kappa_2 = \frac{C_{(x,t)} - C_i}{C_o - C_i} = 1 - erf\left(\frac{x}{\sqrt{4 D_X t}}\right) \tag{5.6}$$

where the symbols have the same physical meaning as in equation (5.1).

Equation (5.6) applies to the situation where an element of high concentration at the surface (here carbon) diffuses into the bulk of the material during long time exposure at a constant temperature through the parent austenite lattice. The results from such predictions are presented graphically in Fig. 5.13, which shows plots of the calculated carbon concentration profiles after 1 month, 6 months, 1 year, 2 years and 4 years respectively, again using input data from Table 5.2.

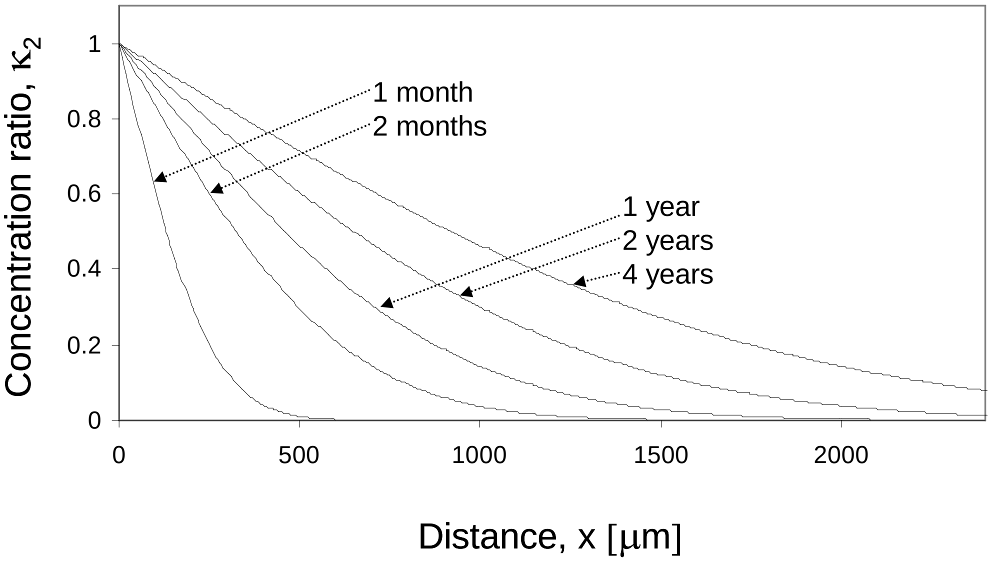

Figure 5.13 Predicted concentration profiles of carbon in the surface near regions of a ternary Ni-20wt%Cr-2wt%Al alloy at 540ºC under different exposure conditions. In these calculations it is assumed that the extent of penetration is controlled by bulk diffusion of carbon into the material. The concentration profiles are constructed using equation (5.6) and input data from Table 5.2.

It can be seen from Fig. 5.13 that carbon has the potential of penetrating several millimetres into the bulk of the alloys at 540ºC in the presence of solid graphite at the metal surface. This will be the case following the break-down of the protective surface oxide layer.[39] Even after one month of exposure, the penetration depth is significantly larger than the observed (visible) width of the white zone in Fig. 5.1, which is about 30µm. Moreover, this zone width tends to remain reasonably constant during the metal dusting corrosion process, which again is in conflict with the results in Fig. 5.13. Hence, it is reasonable to assume that a quasi-steady state situation soon is established within the white zone during exposure, where the corrosion front advances by a coupled diffusion process involving successive carbide formation and oxidation at the pit/white zone interface.

The idea of treating metal dusting corrosion in Ni-based alloys as a process of internal carburisation and oxidation occurring below the corrosion pit surface has previously been launched by several authors,[20, 45, 49] and a plausible model for this will be presented below, starting with the carbide formation.

5.4.4. Models for internal carburisation and oxidation

The electron microscope analyses of the constituent phases being detected within the white zone of alloys 602 and 693 revealed evidence of Cr_3C_2 carbide formation adjacent to the corrosion pits (see Figs. 5.4 through 5.8). This observation implies that there must be a steady supply of carbon from the surface, through the corrosion pit and into the white zone, which then reacts with chromium to form carbides.

Close to the corrosion pit/white zone interface the conditions are more oxidising. Here both the carbides and uncombined Cr (together with Al bound as hardening γ'- Ni_3Al precipitates) will be thermodynamically unstable in the presence of oxygen[39, 47, 61, 62], which is continuously supplied to the metal surface from the surrounding gas phase. This, in turn, leads to oxide formation and re-precipitation of graphite following the carbide decomposition and eventually to the development of the characteristic layered pit microstructures shown previously in Figs. 5.1 (a) and (b).

The main reactions involved during the diffusion process are summarised in Fig. 5.14 (a). This schematic drawing shows the $Cr_\alpha C_\beta$ formation within the carburised zone (CZ), the carbide decomposition and subsequent oxide formation within the oxidised zone (OZ) and the resulting development of the layered pit microstructure within the corrosion pit. Because the growth of the corrosion pits is a moving interface problem, the positions of the three interfaces 1, 2 and 3 in Fig. 5.14 (a) are in the general case related to a set of partial differential equations that account for the flux balance across the moving interfaces and a continuity equation for each phase that satisfies Fick's second law of diffusion. Although such coupled equations can be solved mathematically using numerical methods, the effort is not justified in the present case where a simple quasi-stationary solution for metal dusting corrosion in engineering alloys is sought. A more pragmatic approach would therefore be to treat internal carburisation and oxidation as separate processes and first derive the appropriate expressions for the interface velocities v_1 and v_2 on the basis of Fick's first law of diffusion by invoking the linear concentration approximation for the fast diffusing elements C and O. On the other hand, the slow diffusing elements Cr and Al are considered to be immobile and will thus be consumed at a rate which is controlled by diffusion of C or O through the austenite lattice. Based on an evaluation of the bulk diffusivities data provided in Table 5.2, this assumption seems reasonable.

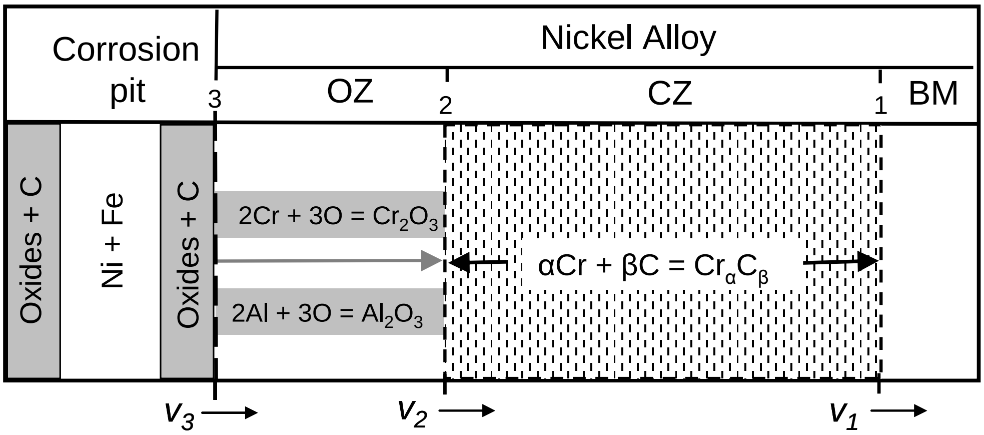

(a)

Figure 5.14 Proposed diffusion model for internal carburisation and oxidation of Ni-based alloys; (a) Schematic representation of the main reactions involved during internal precipitation of carbides, oxides and graphite, (b) Assumed carbon concentration profile within the carburised zone (CZ), as determined by the interface C_C^i and bulk concentration C_C^b of carbon, respectively, (c) Assumed oxygen concentration profile within the oxidised zone (OZ), as determined by the interface C_O^i and bulk concentration C_O^b of oxygen, respectively.

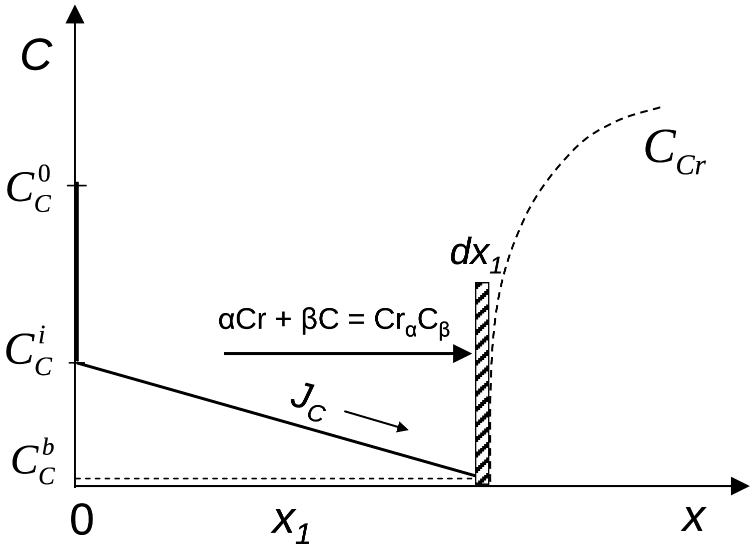

C
C_C^0
C_{Cr}
dx_1
$\alpha Cr + \beta C = Cr_\alpha C_\beta$
C_C^i
J_C
C_C^b
0
x_1
x

(b)

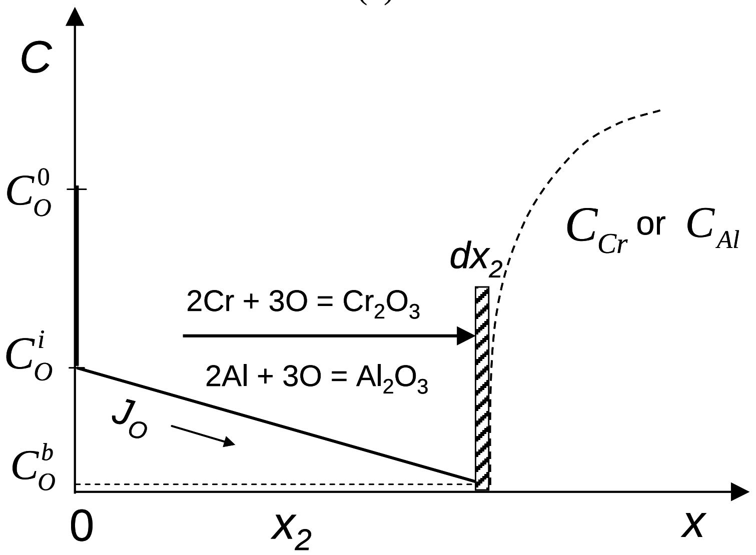

C
C_O^0
C_{Cr} or C_{Al}
dx_2
$2Cr + 3O = Cr_2O_3$
C_O^i
$2Al + 3O = Al_2O_3$
J_O
C_O^b
0
x_2
x

(c)

Figure 5.14 Continued.

5.4.4.1. Carbon diffusion

The situation existing during diffusion is described in Fig. 5.14 (b) and (c) for the internal carburisation and oxidation case, respectively. It follows from Fig. 5.14 (b) that the molar flux of carbon through the carburised zone (CZ) can be expressed as:

$$J_C \left(\frac{mol}{m^2 s}\right) = -D_C \frac{dC}{dx} \approx D_C \frac{C_C^i}{x_1} \tag{5.7}$$

which is a reasonable approximation when the interface concentration of carbon C_C^i is considerably larger than the corresponding bulk concentration of carbon C_C^b in the base material.

Similarly, the amount of $Cr_\alpha C_\beta$ which forms due to reactions between C and Cr at the interface position x_1 is given as:

$$J_{Cr_\alpha C_\beta}\left(\frac{mol}{m^2 s}\right)=\frac{dx_1}{dt}\,f_{Cr_\alpha C_\beta}\,\frac{1}{\Omega_{Cr_\alpha C_\beta}}=\frac{1}{\beta}D_C\,\frac{C_C^i}{x_1} \tag{5.8}$$

where $f_{Cr_\alpha C_\beta}$ and $\Omega_{Cr_\alpha C_\beta}$ are the volume fraction and molar volume of the $Cr_\alpha C_\beta$ phase, respectively. These parameters are defined previously in Appendix II.

After rearranging equation (5.8) and substituting for $f_{Cr_\alpha C_\beta}$ and $\Omega_{Cr_\alpha C_\beta}$, using the definitions in Appendix II, we get:

$$\frac{dx_1}{dt}=\frac{k_1}{x_1} \tag{5.9}$$

where

$$k_1=\frac{\alpha}{\beta}\,\frac{D_C\,C_C^i}{C_{Cr}^0\,Z_{Cr}} \tag{5.10}$$

which following integration reads:

$$x_1=\sqrt{2k_1 t} \tag{5.11}$$

Note that the expression for the parabolic growth constant correctly reduces to:

$$k_1=\frac{1}{\beta}\,\frac{D_C\,C_C^i}{C_{Cr}^0} \tag{5.12}$$

for the specific case where all Cr in the alloy is bound as CrC_β, corresponding to α and Z_{Cr} equal to unity in equation (5.10). This means that the classical Wagner model[55, 63] for internal oxidation/carburisation is a special solution of equations (5.10) and (5.11).

5.4.4.2. Oxygen diffusion

The next step is to derive similar kinetic equations for the oxidation of $Cr_\alpha C_\beta$, Cr and Al occurring within the oxidised zone (OZ) adjacent to the corrosion pit. Referring now to Fig. 5.14 (c), the molar flux of oxygen through this zone can be written as:

$$J_O\left(\frac{mol}{m^2 s}\right) = -D_O\frac{dC}{dx} \approx D_O\frac{C_O^i}{x_2} \tag{5.13}$$

which again is a reasonable approximation when $C_O^i >> C_O^b$.

This flux of oxygen is then consumed by reactions with $Cr_\alpha C_\beta$, dissolved Cr and Al at the interface position x_2, leading to the formation of Cr_2O_3 and Al_2O_3 in an amount which is determined by their volume fractions $f_{Cr_2O_3}$ and $f_{Al_2O_3}$ multiplied by the reciprocal values of their molar volumes $\Omega_{Cr_2O_3}$ and $\Omega_{Al_2O_3}$. Thus, by considering the stoichiometry of the total oxidation reaction, we may write:

$$J_{X_2O_3}\left(\frac{mol}{m^2 s}\right) = \frac{dx_2}{dt}\left[f_{Cr_2O_3}\frac{1}{\Omega_{Cr_2O_3}} + f_{Al_2O_3}\frac{1}{\Omega_{Al_2O_3}}\right] = \frac{1}{3}D_O\frac{C_O^i}{x_2} \tag{5.14}$$

After rearranging equation (5.14) and substituting for the parameters $f_{Cr_2O_3}$, $\Omega_{Cr_2O_3}$, $f_{Al_2O_3}$ and $\Omega_{Al_2O_3}$, using the definitions in Appendix II, we get:

$$\frac{dx_2}{dt} = \frac{k_2}{x_2} \tag{5.15}$$

where

$$k_2 = \frac{2}{3}\frac{D_O C_O^i}{C_{Cr}^0 Z_{Cr} + C_{Al}^0 Z_{Al}} \tag{5.16}$$

which following integration reads:

$$x_2 = \sqrt{2k_2 t} \tag{5.17}$$

Note that equations (5.16) and (5.17) also yield the classical Wagner solution[55, 63] for internal oxidation in the limiting case where the alloy contains no Al (i.e. $C_{Al}^0 Z_{Al} = 0$) and all chromium combines with oxygen to form CrO_β. Under such conditions, where the first term in equation (5.16) is equal to $1/\beta$, the expression for the parabolic growth constant becomes:

$$k_2 = \frac{1}{\beta}\frac{D_O C_O^i}{C_{Cr}^0} \tag{5.18}$$

But in the general case the present oxidation model is more comprehensive compared to the Wagner solution[63] in the sense that it allows for precipitation of other alloying elements and phases as well.

5.4.4.3. Quasi-steady state solutions

As already pointed out in Section 5.4.3.2, the width of the carburised zone, x_{CZ} (or more specifically the white zone) tends to remain approximately constant during the metal dusting corrosion process. This means that the three interfaces indicated in Fig. 5.14 (a) move at approximately the same velocity, i.e. $v_1 \approx v_2 \approx v_3$. Under such conditions the steady-state corrosion rate (SSCR) can be predicted from equation (5.9), taking $x_1 = x_{CZ}$:

$$SSCR = \frac{dx_1}{dt} = \frac{k_1}{x_{CZ}} = \frac{\alpha}{\beta} \frac{D_C C_C^i}{C_{Cr}^0 Z_{Cr}} \frac{1}{x_{CZ}} \tag{5.19}$$

The corresponding width of the oxidised zone $x_2 = x_{OZ}$ is then obtained by combining equations (5.15) and (5.19):

$$x_{OZ} = \frac{k_2}{dx_2 / dt} = \frac{k_2}{dx_1 / dt} = \frac{k_2}{k_1} x_{CZ} \tag{5.20}$$

After substituting for the parabolic growth constants k_1 and k_2, using the definitions in Appendix II, we get:

$$x_{OZ} = \frac{2\beta}{3\alpha} \frac{D_O C_O^i}{D_C C_C^i} \frac{C_{Cr}^0 Z_{Cr}}{C_{Cr}^0 Z_{Cr} + C_{Al}^0 Z_{Al}} x_{CZ} \tag{5.21}$$

At quasi-steady state equation (5.21) predicts that x_{OZ} is interrelated to x_{CZ} through a set of different stoichiometric, concentration and permeability parameters. These parameters have a direct physical meaning in the context of the model being developed and can be estimated from experiments and data available in the scientific literature.

5.4.4.4. Input data used in diffusion models

In general, data for the solubility and diffusivity of carbon and oxygen in Ni-based alloys are scarce and rather uncertain. However, the required input data for D_X og C_X^i can be obtained by taking advantage of the information avaliable on the permeability (i.e. the product $D_X C_X^i$) of the same elements.[47, 56, 64, 65] The permeability of carbon in alloy 602 at 650, 700 and

750ºC, as reported by Hänsel *et* al.,[47] has been used as a basis for evaluating the interface concentration C_C^i of carbon in the presence of solid graphite at the surface. First, the reported permeability data is extrapolated down to 540ºC and then combined with the ThermoCalc diffusivity data for carbon in Table 5.2 to yield the corresponding carbon solubility at that temperature. Similarly, the permeability data reported for oxygen by Meijering[64] has been used to evaluate the oxygen diffusivity in Ni-based alloys by extrapolating the curve for log($D_O C_O^i$) versus 1/T down to 540ºC. Then Sieverts' law[66] is employed to estimate the solid solubility of oxygen in Ni in equilibrium with O_2(g) at 540ºC and 35 bar total pressure by invoking the relationship:

$$C_O^i\,(35\,bar) = C_O^i\,(1\,bar)\sqrt{35} \tag{5.22}$$

taking C_O^i at 1 bar equal to 0.05 at%.[65] The results are summarised in Table 5.4, yielding the extrapolated values for D_C, D_O, C_C^i and C_O^i at 540ºC and 35 bar total pressure.

Table 5.4 Summary of extrapolated data for the solubility and diffusivity of carbon and oxygen in Ni-based alloys at 540ºC and 35 bar total pressure.[47, 56, 64, 65]

Parameter	Carbon		Oxygen	
	C_C^i [mol/m^3]	D_C [m^2/s]	C_O^i [mol/m^3]	D_O [m^2/s]
Value	774.0	7.5 10^{-15}	428.0	8.9 10^{-17}

5.4.4.5. Predictions of steady-state corrosion rates

The steady-state corrosion rates (SSCR) during plant exposure can now be predicted from equation (5.19), using input data from Tables 2.1 (Part II), 5.3 and 5.4. These calculations apply to Cr_3C_2 carbide formation and a constant width of the carburised zone of 30μm. The results are summarised in Fig. 5.15 (a), yielding the calculated corrosion rates in alloys 602 and 693 at 540ºC and 35 bar total pressure. The corresponding widths of the oxidised zone (x_{OZ}) are, in turn, given in Fig. 5.15 (b) for the special case where all Cr and Al are oxidised to Cr_2O_3 and Al_2O_3, respectively (i.e. $Z_{Cr} = Z_{Al} = 1$).

It can be seen from Fig. 5.15 (a) that the SSCR depends strongly on the fraction of Cr which is bound as carbide. But under otherwise identical conditions the nominal chromium content in the alloy is also of importance. In alloy 693 the nominal Cr content is 29.7wt% as compared to 25.1wt% in alloy 602, which explains why the predicted corrosion rate is slightly lower in the former case. Although the exact value of Z_{Cr} is difficult to measure under the prevailing circumstances, it is estimated to be within the range from 0.4 to 0.8, based on the observations made in the TEM of the carbide phases. Hence, both alloys should yield a steady-state corrosion rate between 0.5 to 0.3mm per year according to Fig. 5.15 (a) following the break-down of the protective surface oxide layer. As already pointed out in Section 5.4.1, this occurs towards the end of the incubation period, which is seen to last for approximately 2 years in alloy 602 and about 4 years in alloy 693 under the prevailing exposure conditions.

Moreover, it is evident from Fig. 5.15 (b) that both alloys should reveal a very narrow oxidized zone (*OZ*) adjacent to the corrosion pit, which at 540ºC and 35 bar total pressure is estimated to be about 0.65μm. This value is of the same order of magnitude as the observed spacing between the Cr_2O_3/Al_2O_3 lamellae within the corrosion pits (see Figs. 5.4 and 5.5), taking the lamella spacing as a cursor for the actual oxidized zone depth being established within the white zone at quasi-steady state.

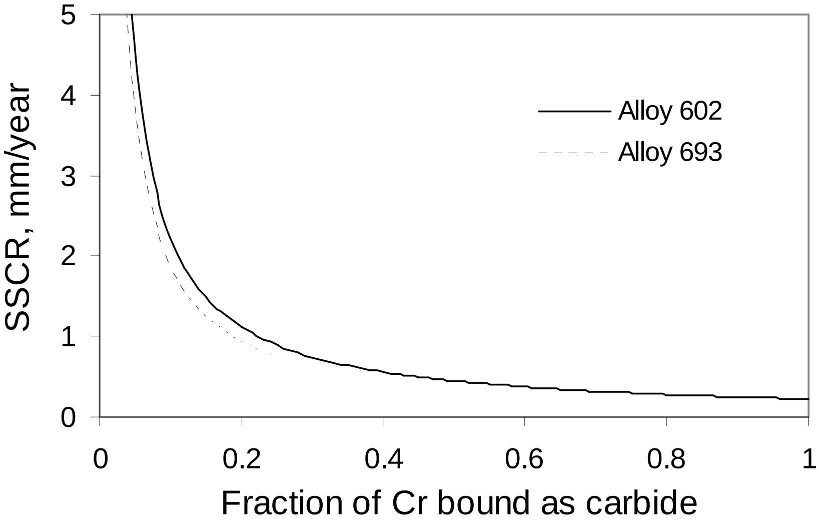

(a)

Figure 5.15 Predicted steady state corrosion rates (SSCR) and corresponding widths of the oxidized zone (OZ) in alloys 602 and 693 at 540ºC and 35 bar total pressure following the break-down of the protective surface oxide layer; (a) Plots of SSCR versus the fraction of Cr bound as Cr_3C_2 carbides, (b) Estimated widths of the oxidised zone for the specific case where all Cr and Al are bound as Cr_2O_3 and Al_2O_3, respectively. The calculations are done using equations (5.19) and (5.21) and a constant width of the carburised zone of 30μm. Input data as in Tables 2.1 (Part II), 5.3 and 5.4.

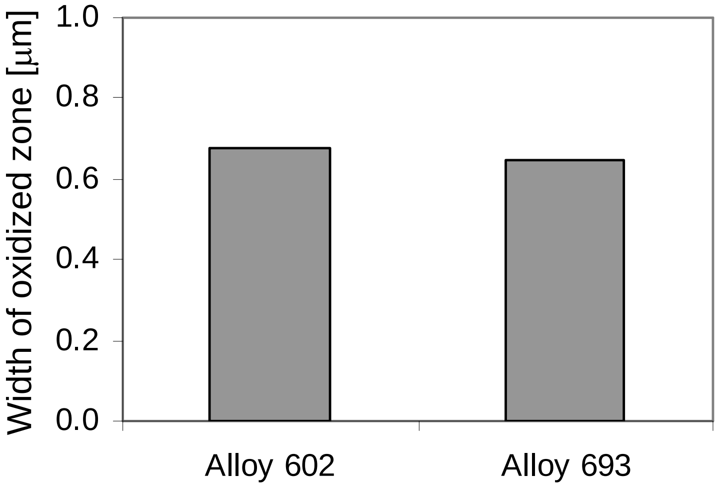

(b)

Figure 5.15 Continued.

5.4.5. Volume changes associated with internal precipitation

In the past, several authors have suggested that internal precipitation of carbides and oxides can be a source of surface disintegration during high-temperature exposure of heat-resistant alloys[20, 41, 49] and thus be part of the metal dusting corrosion mechanism in such alloys. In particular, in-situ oxidation of internal carbides is associated with large volume changes because phases like Cr_2O_3, Al_2O_3 and graphite have a low density compared to nickel.[47] This again leads to the development of high mechanical stresses in the adjacent matrix and eventually to the disintegration of the surface regions of the exposed alloys.

In the following, attempts will be made to quantify the volume changes associated with internal precipitation of carbides in alloys 602 and 693 and the subsequent oxidation of these along with Cr and Al to oxides and graphite, according to the reaction scheme outlined in Fig. 5.14 (a).

5.4.5.1. Constitutive equations

As a starting point, the white zone (*w*) is modelled as a composite material consisting of carbides ($Cr_\alpha C_\beta$), oxides (X_2O_3), graphite (C) and austenite (*a*). Taking V_w and V_a equal to the unit volume of the white zone and the parent austenite phase, respectively, the corresponding volume change ΔV due to internal precipitation can be expressed as:

$$\Delta V(\%) = \frac{V_w - V_a}{V_a} 100 \tag{5.23}$$

Provided that the increase in the total mass of the system due to the carbon and oxygen absorption from the surrounding gas atmosphere is neglected, it is possible to replace V_w and V_a in equation (5.23) with the corresponding densities ρ_w and ρ_a:

$$\Delta V(\%) = \frac{\frac{1}{\rho_w} - \frac{1}{\rho_a}}{\frac{1}{\rho_a}} 100 = \frac{\rho_a - \rho_w}{\rho_w} 100 \tag{5.24}$$

The density ρ_w of the white zone containing the internal precipitates can, in turn, be calculated from the "rule of mixtures" through the well-established relationship[67]:

$$\rho_w = \sum_i f_i \, \rho_i \tag{5.25}$$

where f_i and ρ_i are the volume fraction and density of component (i) in the white zone, respectively. Because the white zone contains varying levels of different internal precipitates, its density will change correspondingly across the carburised zone and into the adjacent oxidized zone facing the corrosion pit.

5.4.5.2. Volume changes within the carburised zone

Within the carburised zone, $Cr_\alpha C_\beta$ carbides along with austenite (a) are the main constituent phases, as shown previously in Fig. 5.14 (a). Hence, the appropriate expression for the density ρ_w becomes:

$$\rho_w = f_{Cr_\alpha C_\beta} \, \rho_{Cr_\alpha C_\beta} + (1 - f_{Cr_\alpha C_\beta})\rho_a \tag{5.26}$$

where the volume fraction of carbides, according to the definitions in Appendix II, is given by the relationship:

$$f_{Cr_\alpha C_\beta} = \frac{1}{\alpha} \, \Omega_{Cr_\alpha C_\beta} \, C_{Cr}^{o} \, Z_{Cr} \tag{5.27}$$

5.4.5.3. Volume changes within the oxidised zone

Within the oxidised zone, the $Cr_\alpha C_\beta$ carbides react with oxygen to form Cr_2O_3 and graphite, respectively, according to the following stoichiometric reaction:

$$Cr_\alpha C_\beta + \frac{3\alpha}{2} O = \frac{\alpha}{2} Cr_2O_3 + \beta C \tag{5.28}$$

In addition, dissolved chromium remaining in the austenite matrix along with aluminium are oxidised to Cr_2O_3 and Al_2O_3, respectively. Hence, the total number of constituent phases are four (i.e. Cr_2O_3, Al_2O_3, graphite and austenite), which gives:

$$\rho_w = f_{Cr_2O_3}\rho_{Cr_2O_3} + f_{Al_2O_3}\rho_{Al_2O_3} + f_C\,\rho_C + (1 - f_{Cr_2O_3} - f_{Al_2O_3} - f_C)\,\rho_a \tag{5.29}$$

where

$$f_{Cr_2O_3} = \frac{1}{2}\,\Omega_{Cr_2O_3}\,C^0_{Cr}\,Z_{Cr} \tag{5.30}$$

$$f_{Al_2O_3} = \frac{1}{2}\,\Omega_{Al_2O_3}\,C^0_{Al}\,Z_{Al} \tag{5.31}$$

$$f_C = \frac{\beta}{\alpha}\,\Omega_C\,C^0_{Cr}\,Z_{Cr} \tag{5.32}$$

These expressions for the pertinent volume fractions are in accordance with the definitions in Appendix II.

5.4.5.4. Calculated volume changes in alloys 602 and 693

By using input data from Tables 2.1 (Part II) and 5.3 it is possible to calculate the volume changes which occur within the white zone of alloys 602 and 693 during metal dusting corrosion due to internal precipitation. The results are summarised in Fig. 5.16 (a) and (b), respectively, which apply to a fixed carbide composition of Cr_3C_2.

A closer inspection of Figs. 5.16 (a) and (b) reveals some interesting trends and observations. Whereas the Cr_3C_2 carbide formation only leads to small volume changes, the corresponding volume changes occurring within the adjacent oxidised zone are dramatic in the sense that they may exceed 60 to 80%, depending on the alloy composition. As expected, the Cr_2O_3 formation contributes to approximately one half of the calculated volume expansion within the oxidised zone, whereas the other half can be attributed to the precipitation of Al_2O_3 and graphite.

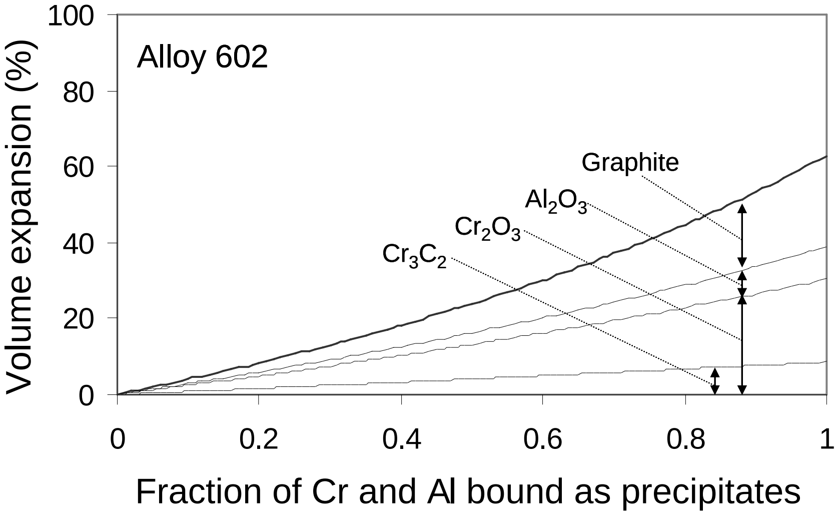

(a)

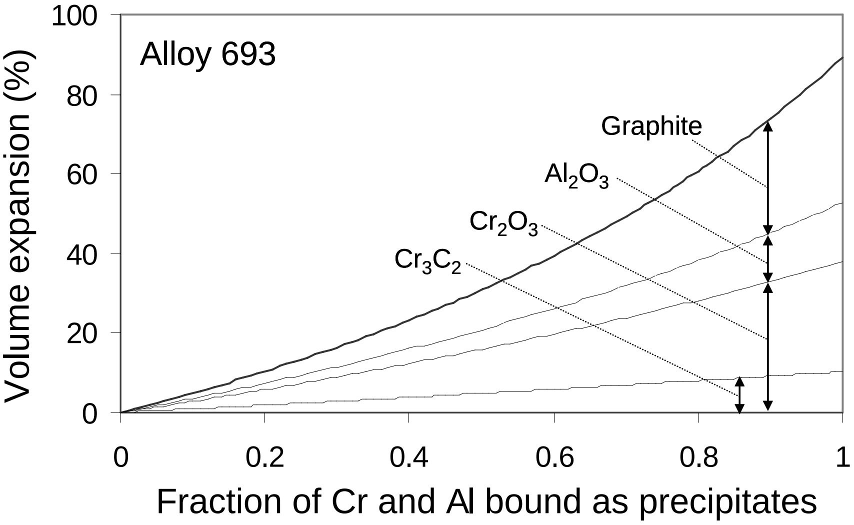

(b)

Figure 5.16 Calculated volume changes within the white zone of alloys 602 and 693 due to internal precipitation of carbides, oxides and graphite; (a) Alloy 602, (b) Alloy 693. The graphs apply to a fixed carbide composition of Cr_3C_2.

In particular, the graphite which forms as a result of the carbide oxidation is seen to have a strong effect on the volume expansion and will thus contribute significantly to the surface disintegration accompanying the metal dusting corrosion. In the past several investigators have noted that internal graphite formation may be responsible for the metal dusting corrosion attacks observed in Ni-based alloys,[29, 68, 69] but to the present author's knowledge its origin has not yet been associated with internal oxidation of carbides. Nevertheless, the calculated volume changes related to the Cr_2O_3, Al_2O_3 and graphite formation are so large that they must be the main factor contributing to the observed disintegration of the alloys 602 and 693 during metal dusting corrosion, leading to the development of the layered pit microstructures observed previously in Figs. 5.4 (a) and 5.5 (a).

5.4.6. Mechanisms of metal dusting corrosion in Ni-based alloys

The main results from the detailed modelling of the physical reactions involved during metal dusting corrosion are summarised in Fig. 5.17. Figure 5.17 (a) shows a schematic drawing of the damaged surface oxide layer from which a hemispherical pit starts to grow into the parent material.

Moreover, the characteristic layered pit microstructure is also displayed along with the white zone containing the internal carbides. Towards the left in the drawing an example of renewed oxide formation through Cr and Al bulk diffusion is indicated. This process occurs below the surface and contributes to healing of cracks and flaws in the surface oxide, thereby preventing carbon from penetrating into the bulk of the alloys during the incubation period.

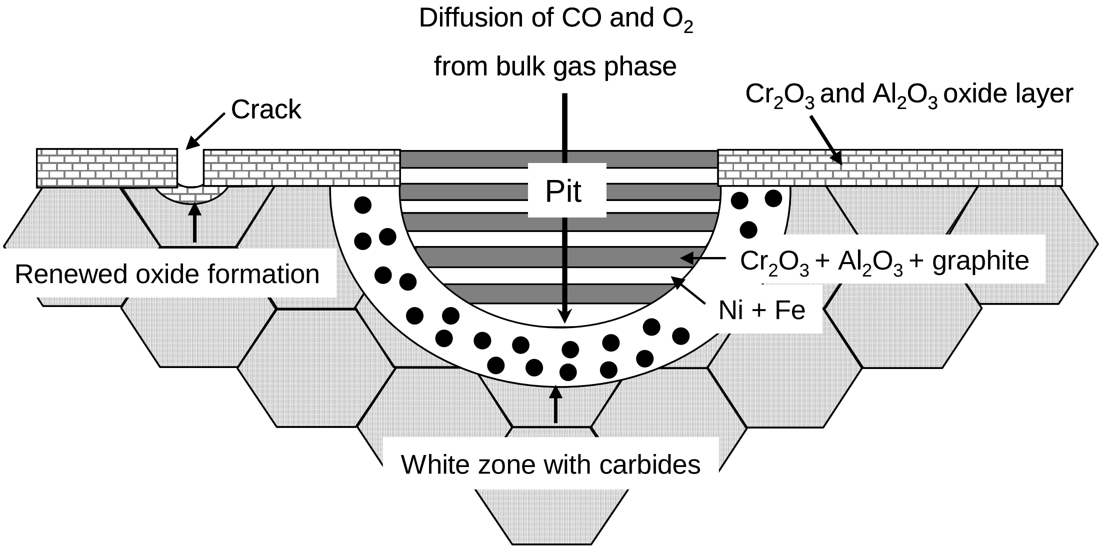
Diffusion of CO and O_2 from bulk gas phase
Cr_2O_3 and Al_2O_3 oxide layer
Crack
Pit
Renewed oxide formation
$Cr_2O_3 + Al_2O_3$ + graphite
Ni + Fe
White zone with carbides

(a)

Figure 5.17 Proposed model for metal dusting corrosion in Ni-based alloys involving internal precipitation of carbides, oxides and graphite; (a) Details of the pit formation and the associated carbide precipitation within the white zone following the break-down of the protective surface oxide layer, (b) Resulting corrosion behaviour, as observed both during and after the incubation period for metal dusting corrosion. Note that the incubation period ends when carbon starts to penetrate into the bulk of the materials through cracks in the surface oxide layer.

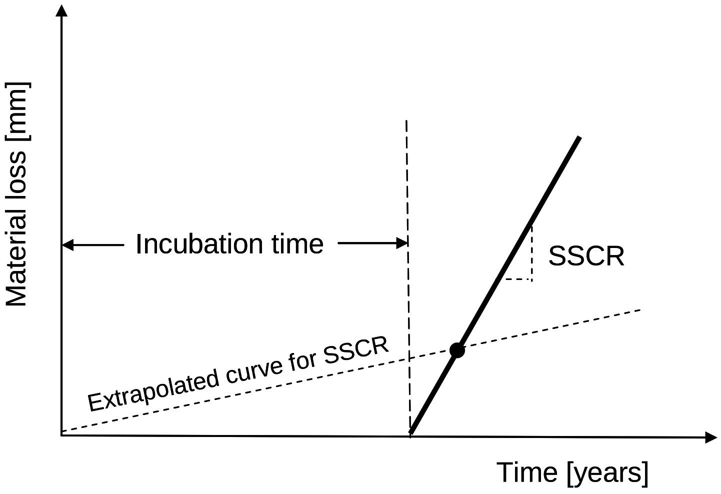

(b)

Figure 5.17 Continued.

The resulting corrosion behaviour is shown schematically in Fig. 5.17 (b), yielding a plot of the material loss (in millimetres) versus the exposure time (in years). It follows that the material loss is negligible during the incubation period as long as the surface oxide layer is intact and prevents carbon from diffusing into the bulk of the alloys. In the Ni-based alloys 602 and 693 aluminium is the key element determining the duration of the incubation period, which under the prevailing exposure conditions varies from about 2 to 4 years, depending on the alloy composition.[39] Then, following the break-down of the protective surface oxide layer, carbon starts to penetrate the material, leading to internal precipitation of chromium carbides within an approximately 30μm thick belt in front of the pits (referred to as the white zone). These carbides, along with Cr and Al, are subsequent oxidised to Cr_2O_3, Al_2O_3 and graphite. The oxidation occurs within a very narrow zone adjacent to the white zone/pit interface, where the oxygen being consumed in the reactions is supplied from the surrounding gas atmosphere through pore diffusion in the pit. Since the internal oxide/graphite formation is associated with large volume changes, high mechanical stresses start to build-up within the white zone. This eventually leads to the complete disintegration of the original alloy matrices into a layered microstructure consisting of Ni + Fe and Cr_2O_3 + Al_2O_3 + graphite, respectively.

Since the permeability of the porous pit microstructure is sufficiently high to provide rapid transport of the gaseous components CO and O_2 from the surface and to the reaction front, the rate controlling step for the internal carburisation and oxidation is diffusion of carbon atoms and oxygen ions through the austenite lattice. Under such conditions the diffusion model predicts that the steady-state corrosion rate should be independent of time, as shown in Fig. 5.17 (b). Therefore, the actual corrosion rate will differ from the one estimated by linear extrapolation of experimental data based on measurements of the material loss. The latter method, which is frequently used by industry, is rather uncertain because it does not include a consideration of the incubation time for metal dusting corrosion.

Finally, it is important to realise that the proposed metal dusting corrosion mechanism involving internal carburisation and oxidation is essentially the same as the one launched by Hänsel *et* al.[47] and Petkovic-Luton and Ramanarayanan[41] to explain the observed surface degradation of heat-resistant alloys in CO-CO_2 gas mixtures at temperatures of 650 to 1000ºC. This similarity between the two high-temperature corrosion phenomena makes the model more general and provides a basis for predicting the corrosion behaviour under conditions which have not yet been explored experimentally. For example at 540ºC and 35 bar total pressure Fig. 5.15 (a) predicts that the steady-state corrosion rate in alloys 602 and 693 should be about 0.3 to 0.5mm per year. By utilising the permeability data reported by Hänsel *et* al.[47], it is possible to use equation (5.19) and predict how an increase in the gas exposure temperature from, say, 540 to 600ºC influences the SSCR. Because this temperature change means that the carbon permeability increases by nearly a factor of four, the corrosion rate should also increase by approximately the same factor. Thus, the corresponding material loss due to metal dusting corrosion at 600ºC and 35 bar total pressure is estimated to be of the order of 1.2 to 2.0 mm/year.

5.5. Conclusions

The basic conclusions that can be drawn from this investigation are the following:

- Metal dusting corrosion, as observed in alloys 602 and 693 during long-time exposure to syngas at 540°C and 35 bar total pressure, occurs as a result of successive carburisation and oxidation of the alloy matrices. The corrosion attack starts by carbon diffusing into the bulk of the alloys following the break-down of the protective Cr_2O_3 - Al_2O_3 surface oxide layer. As long as this oxide layer is intact, it provides an effective barrier against carbon intrusion by virtue of its ability to continuously recover during exposure.

- The corrosion pits grow by a process of internal precipitation of Cr_3C_2 carbides, which form within an approximately 30µm thick belt in front of the corrosion pits (referred to as the white zone). These carbides, along with Cr and Al dissolved in the austenite matrix, are subsequently oxidised to Cr_2O_3, Al_2O_3 and graphite. The internal oxidation is seen to occur within a narrow zone adjacent to the white zone/pit interface, where the oxygen being consumed in the reactions is supplied from the surrounding gas atmosphere through diffusion.

- In particular, the oxidation of the internal Cr_3C_2 carbides to Cr_2O_3 and graphite is associated with large volume changes, which in alloys 602 and 693 add up to about 60 and 80%, respectively. This volume expansion results in the build-up of high mechanical stresses within the white zone and eventually to the complete disintegration of the original alloy matrices into a layered pit microstructure consisting of Ni + Fe and Cr_2O_3 + Al_2O_3 + graphite, respectively. The indications are that permeability of the porous pit microstructure is sufficiently high to provide rapid transport of the gaseous components CO and O_2 from the surface and to the reaction front. This essentially means that the rate controlling step for the internal carburisation and oxidation is diffusion of carbon atoms and oxygen ions through the austenite lattice.

- Based on this underlying assumption, a model for metal dusting corrosion in Ni-based alloys has been developed, which allows quantitative predictions of the quasi-steady state corrosion rate under different experimental conditions. The model has roots in thermodynamics and diffusion theory and yields the classical Wagner solution for the special case where the internal oxidation/carburisation occurs by formation of a single reaction product. But in the general case the present model is more comprehensive compared to the Wagner solution in the sense that it allows for precipitation of other alloying elements and phases as well.

5.6. References

1. R. T. Jones, K. L. Baumert, "*Metal dusting - an overview of current literature*", paper presented at Corrosion/2001, Houston, Texas, USA, 11.-16.March 2001, NACE International, Houston, Texas, USA.
2. H. J. Grabke, R. Krajak, J. C. Nava Paz: *Corrosion Science*, 1993, No.5-8, vol. 35, pp. 1141-1150.
3. R. C. Schueler: *Hydrocarbon processing*, 1972, vol. 51, pp. 73-75.
4. G. Y. Lai: *High-Temperature Corrosion of Engineering Alloys*, 1'st ed., ASM International, Materials Park, Ohio, 1990.
5. J. Pattinson: *Journal of Iron Institute*, 1876, vol. 1, pp. 85-100.
6. E. Q. Camp, C. Phillips, L. Gross: *Corrosion*, 1945, No.3, vol. 1, pp. 149-160.
7. H. K. Ihrig: *Transactions of the Electrochemical Society,* 1947, vol. 91, pp. 641-654.
8. F. A. Prange: *Corrosion*, 1959, No.12, vol. 15, pp. 619t-621t.
9. F. Eberle, R. D. Wylie: *Corrosion*, 1959, No.12, vol. 15, pp. 622t-626t.
10. W. B. Hoyt, R. H. Caughey: *Corrosion*, 1959, No.12, vol. 15, pp. 627t-630t.
11. R. F. Hochman, J. H. Burson: *American Petroleum Institute Division of Refining Proceedings*, 1966, vol. 46, pp. 331-344.
12. H. J. Grabke, R. Krajak, E. M. Müller-Lorenz: *Werkstoffe und Korrosion*, 1993, vol. 44, pp. 89-97.
13. E. Pippel, J. Woltersdorf, H. J. Grabke, S. Strauss: *Steel research*, 1995, No.5, vol. 66, pp. 217-221.
14. D. C. Agarwal, W. R. Herda, U. Brill: *Advanced materials & processes,* 1995, No.4, vol. 148, pp. 42-45.
15. M. L. Holland, H. J. De Bruyn: *International Journal of Pressure Vessels and Piping*, 1996, No.1-3, vol. 66, pp. 125-133.
16. C. M. Chun, T. A. Ramanarayanan, J. D. Mumford: *Materials and Corrosion*, 1999, vol. 50, pp. 634-639.
17. B. Schmid: "*Microscale examination of metal dusting corrosion in steels and in-situ observations of high temperature oxidation of metals*", PhD Thesis, NTNU - Norwegian University of Science and Technology, Department of Materials Technology and Electrochemistry, Trondheim, 2000.
18. B. Schmid, J. C. Walmsley, Ø. Grong, R. Ødegård: *Metallurgical and Materials Transactions A*, 2003, 34A, pp. 345-354.

19. B. A. Baker, G. D. Smith, "*Alloy selection for environments which promote metal dusting*", paper presented at Corrosion/2000, Orlando, FL, USA, 26.-31.March 2000, NACE International, Houston, Texas, USA.

20. H. J. De Bruyn, E. H. Edwin, S. Brendryen, "*Apparent influence of steam on metal dusting*", paper presented at Corrosion/2001, Houston, Texas, USA, 11.-16.March 2001, NACE International, Houston, Texas, USA.

21. Z. Zeng, K. Natesan, V. A. Maroni: *Oxidation of metals*, 2002, No.1-2, vol. 58, pp. 147-170.

22. C. H. Toh: "*Metal Dusting on Heat-Resistant Alloys under Thermal Cyclic Conditions*", PhD Thesis, University of New South Wales, School of Materials Science and Engineering, Sydney, 2002.

23. C. H. Toh, P. R. Munroe, D. J. Young: *Oxidation of metals*, 2002, No.1/2, vol. 58, pp. 1-21.

24. P. Szakálos, R. Pettersson, S. Hertzman: *Corrosion Science*, 2002, No.10, vol. 44, pp. 2253-2270.

25. P. Szakálos: *Materials and Corrosion*, 2003, No.10, vol. 54, pp. 756-762.

26. A. Schneider, H. J. Grabke: *Materials and Corrosion*, 2003, No.10, vol. 54, pp. 793-798.

27. F. D. Gabriele, J. R. Bernstein, M. M. Al-Qhatani, Z. Liu, M. P. Jordan, J. A. Richardson, F. H. Stott: *Materials and Corrosion*, 2003, No.11, vol. 54, pp. 854-859.

28. A. T. W. Kempen, J. C. Wortel: *Materials and Corrosion*, 2004, No.4, vol. 55, pp. 249-258.

29. Y. Nishiyama, T. Kudo, N. Otsuka: *Materials Transactions*, 2005, No.8, vol. 46, pp. 1890-1896.

30. R. Kirchheiner, D. J. Young, P. Becker, R. N. Durham, "*Improved Oxidation and Coking Resistance of a New Alumina Forming Alloy 60 HT for the Petrochemical Industry*", paper presented at Corrosion/2005, Houston, Texas, USA, 3.-7.April 2005, NACE International, Houston, Texas, USA.

31. H. Stahl, S. Gyde Thomsen: *Ammonia plant safety (and related facilities)*, 1996, vol.36, pp. 180-191.

32. S. B. Parks, C. M. Schillmoller: *STAINLESS STEEL WORLD*, 1997, No.3, vol. 9, pp. 44-49.

33. H. J. De Bruyn, B. Schmid, Ø. Grong, J. Z. Albertsen, "*Adapting metal dusting research to trends in syngas technology*", paper presented at Corrosion/2005, Houston, Texas, USA, 3.-7.April 2005, NACE International, Houston, Texas, USA.

34. K. Hirotani: in *Proceedings of The Fifteenth International Offshore and Polar Engineering Conference*, The International Society of Offshore and Polar Engineers, Seoul, Korea, 2005, pp. 54-61.

35. H. J. Grabke: *Materials and Corrosion*, 2003, No.10, vol. 54, pp. 736-746.

36. Y. Nishiyama, N. Otsuka, T. Kudo, O. Miyahara, "*Metal dusting of nickel-base alloys in simulated syngas mixtures*", paper presented at Corrosion/2003, San Diego, California, USA, 16.-20.March 2003, NACE International, Houston, Texas, USA.

37. I. Koszman: in *High temperature gas-metal reactions in mixed environments*, Ed.S. A. Jansson, Z. A. Foroulis, The Metallurgical Society of AIME, New York, 1973, pp. 155-167.

38. P. Elliott, "*Materials performance in high-temperature environments - making the choice*", paper presented at Corrosion/2000, Orlando, Florida, USA, 26.-31. March 2000, NACE International, Houston, Texas, USA.

39. J. Z. Albertsen: Part IV of the present thesis.

40. H. J. Grabke, A. Schnaas: in *Alloy 800*, Ed.W. Betteridge, Petten, The Netherlands, 1978, pp. 195-211.

41. R. Petkovic-Luton, T. A. Ramanarayanan: *Oxidation of metals*, 1990, No.5-6, vol. 34, pp. 381-400.

42. A. Perkins: in *Behaviour of High Temperature Alloys in Aggressive Environments*, Petten, The Netherlands, 1980, pp. 617-647.

43. X. G. Zheng, D. J. Young: *Oxidation of metals*, 1994, No.3/4, vol. 42, pp. 163-190.

44. H. J. Grabke, E. M. Müller-Lorenz, "*Occurrence and prevention of metal dusting on stainless steels*", paper presented at Corrosion/2001, Houston, Texas, USA, 11.-16.March 2001, NACE International, Houston, Texas, USA.

45. B. Schmid, Ø. Grong, R. Ødegård: *Materials and Corrosion*, 1999, No.11, vol. 50, pp. 647-653.

46. O. V. D. Biest, J. M. Harrison, J. F. Norton: paper presented at The International Conference of the Behaviour of High Temperature Alloys in Aggressive Environments, Petten, The Netherlands, 15.-18. October, 1979, Ed.I. Kirman, The Metals Society, pp. 681-703

47. M. Hänsel, C. A. Boddington, D. J. Young: *Corrosion Science*, 2003, vol.45, pp. 967-981.
48. Y. Nishiyama, N. Otsuka, T. Kudo: *Corrosion Science*, 2006, No.8, vol. 48, pp. 2064-2083.
49. R. A. Perkins, W. Coons, D. J. Radd: in *Properties of High Temperature Alloys, With Emphasis on Environmental Effects*, The Electrochemical Society, Princeton, N.J., 1976, pp. 733-749.
50. J. Z. Albertsen: Part III and IV of the present thesis.
51. R. Kilaas: MacTempas, A Program for Simulating High Resolution TEM images and Diffraction patterns, Version 2.1.1, Berkeley Total Resolution Ltd., Berkeley, CA, 1992.
52. P. Villars, L. D. Calvert, W. B. Pearson: *Pearson's handbook of crystallographic data for intermetallic phases* 1st ed., ASM International, Metals Park, Ohio , USA, 1985.
53. M. J. Donachie, S. J. Donachie: *Superalloys - A Technical Guide*, 2'nd ed., ASM International, Materials Park, Ohio, 2002.
54. J. Cranck: *The Mathematics of Diffusion*, 2'nd ed., Clarenden Press, Oxford, UK, 1975.
55. U. Krupp, H. J. Christ: *Journal of phase equilibria and diffusion*, 2005, No.5, vol. 26, pp. 487-493.
56. A. Engström: "*Long-range Diffusion and Microstructural Evolution in Multiphase Alloys - A Combined Thermodynamic and Kinetic Approach*", PhD Thesis, Royal Institute of Technology, Department of Materials Science and Engineering, Stockholm, 1996.
57. P. Szakálos, M. Lundberg, R. Pettersson: *Corrosion Science*, 2006, No.7, vol. 48, pp. 1679-1695.
58. P. G. Shewmon: *Diffusion in solids*, 1st ed., McGraw-Hill Book Company, New York, 1963.
59. G. Aylward, T. Findlay: *SI Chemical Data*, 3rd ed., John Wiley & Sons, Brisbane, 1994.
60. P. Szakálos: "*Mechanisms of Metal Dusting*", PhD Thesis, KTH - Royal Institute of Technology, Department of Materials Science and Engineering, Stockholm, 2004.
61. FactSage: www.factsage.com, 2005.
62. CRCT-ThermFact-Inc, GTT-Technologies: FACT 53. Compound Database, 2005.
63. C. Wagner: *Zeitschrift für Elektrochemie*, 1959, vol. 63, pp. 772-782.

64. J. L. Meijering: in *Advances in materials research*, Ed.H. Herman, Wiley-Interscience publishers, New York, 1971, pp. 1-81.
65. J. P. Neumann, T. Zhong, Y. A. Chang: *Bulletin of alloy phase diagrams*, 1984, No.2, vol. 5, pp. 141-143.
66. T. Rosenqvist: *Principles of extractive metallurgy*, 2'nd ed., McGraw-Hill International Book Company, Singapore, 1983.
67. D. R. Askeland: *The science and engineering of materials*, 3rd ed., Stanley Thornes Publishers Ltd, Cheltenham, 1998.
68. Z. Zeng, K. Natesan: *Chemistry of Materials*, 2005, No.14, vol. 17, pp. 3794-3801.
69. R. Schneider, E. Pippel, J. Woltersdorf, S. Strauss, H. J. Grabke: *Steel research*, 1997, No.7, vol. 68, pp. 326-332.

APPENDIX II. Symbols, formulae and units used in the diffusion models for metal dusting corrosion.

Symbol	Explanation	Formulae and units	
X	Metallic element Cr or Al		-
Y	Non-metallic element C or O		-
$[\%X]$	Weight concentration of X		[wt%]
$[\%X]^0$	Nominal value of X in alloy/pit		[wt%]
$[\%Y]^0$	Nominal value of Y in alloy/pit		[wt%]
M_X	Molar weight of X		[g/mol]
M_Y	Molar weight of Y		[g/mol]
$X_\alpha Y_\beta$	Carbide or oxide		-
$M_{X_\alpha Y_\beta}$	Molar weight of $X_\alpha Y_\beta$		[g/mol]
ρ_a	Density of alloy		[kg/m^3]
$\rho_{X_\alpha Y_\beta}$	Density of $X_\alpha Y_\beta$		[kg/m^3]
ρ_Y	Density of decomposed Y		[kg/m^3]
$\Omega_{X_\alpha Y_\beta}$	Molar volume of $X_\alpha Y_\beta$	$\frac{M_{X_\alpha Y_\beta}}{\rho_{X_\alpha Y_\beta}}$	[m^3/mol]
Ω_Y	Molar volume of decomposed Y	$\frac{M_Y}{\rho_Y}$	[m^3/mol]
Z_X	Fraction of X bound as $X_\alpha Y_\beta$	$\frac{\%X}{[\%X]^0}$	
C_X^0	Molar concentration of X in alloy	$\frac{1}{100}\frac{\rho_a}{M_X}[\%X]^0$	[mol/m^3]
C_X	Molar concentration of X bound as $X_\alpha Y_\beta$	$C_X^0 Z_X$	[mol/m^3]
$f_{X_\alpha Y_\beta}$	Volume fraction of $X_\alpha Y_\beta$	$\frac{1}{\alpha}\Omega_{X_\alpha Y_\beta} C_X^0 Z_X$	
f_Y	Volume fraction of decomposed Y	$\frac{\beta}{\alpha}\Omega_Y C_X^0 Z_X$	